Search of an ultra high energy neutrino diffuse flux with ANTARES telescope

L. Core

N° d'ordre CPPM-T-2013-04

AIX-MARSEILLE UNIVERSITÉ
FACULTÉ DES SCIENCES DE LUMINY
163 avenue de Luminy
13288 MARSEILLE Cedex 09

THÈSE DE DOCTORAT

Spécialité : *Physique et Sciences de la Matière*

Mention : *Physique des Particules et Astroparticules*

présentée par

Laura Core

en vue d'obtenir le grade de docteur d'Aix-Marseille Université

Search for an ultra high energy neutrino diffuse flux with the ANTARES telescope

Jury composé de

Dr.	E. Kajfasz	Examinateur
Dr.	A. Kouchner	Rapporteur
Dr.	A. Margiotta	Rapporteur
Prof.	J. P. Ernenwein	Directeur de thèse
Prof.	P. Jean	Examinateur

Thèse soutenue le 3 octobre 2013

I'll tell you more later - I must have a long rest now. I'll tell you something of the forbidden horrors he led me into - something of the age-old horrors that even now are festering in out-of-the-way corners with a few monstrous priests to keep them alive. Some people know things about the universe that nobody ought to know, and can do things that nobody ought to be able to do. I've been in it up to my neck, but that's the end.

H. P. Lovecraft, "The Thing on the Doorstep" (1933)

Introduction

Astroparticle physics is a relatively young field derived from the extension of conventional astronomy beyond the optical to the microwave and X spectrum. This new field can explore universe using a different kind of messengers, relying on high energy cosmic rays, gamma rays and neutrinos. The latters, interacting only via weak interaction and being very light, are the ideal messenger to observe astronomical sources, for they are not deflected by galactic magnetic fields and not suffer from absorption.

In 1960 Markov proposed a possible way of detecting high-energy neutrinos using huge volumes of material, such as sea water or ice. Muon neutrinos produced in astrophysical objects reach the Earth and interact via charged current with one of the nucleons of the medium surrounding the detector. The charged current interaction leads to the production of a muon that induces Cherenkov photons emission along its trajectory. These photons can be detected with photomultipliers. At energies above TeV, muons can travel kilometers and are almost collinear with the parent neutrino. Knowing that neutrinos have a low cross section and taking into account the astronomical fluxes, the typical size of the detector should of the order of km^3.

ANTARES is the first neutrino telescope installed in the Mediterranean Sea. It is composed by 12 lines of photomultipliers. Detector construction started in 2006 and was completed in 2008 with the deployment of the last line. The data taking has started in 2007. The main goal of the experiment is the search of high energy neutrinos from astrophysical sources. Its favored position allows to see the galactic center and ANTARES could be considered complementary to the IceCube Antarctic Telescope. It is also a first step before the construction of a km^3 neutrino telescope in the Northern hemisphere.

Neutrino telescopes are optimized to observe upgoing event from neutrinos coming from the other side of the Earth. It is the best way to reject muonic background originating from the interaction of cosmic rays with the nuclei of the atmosphere. However Earth becomes opaque to neutrinos with energy greater than 10 PeV and it is difficult to detect the upgoing signal

beyond this energy. In this case neutrinos have to cross a smaller amount of matter which is achieved if their direction is near the horizon. This thesis is mainly dedicated to the study of these particular neutrinos, called *Ultra High Energy (UHE) neutrinos*, but we will also study a more conventional energy range, called Very High Energy neutrinos.

Ultra high energy neutrinos may have very different origins: a part of them comes from the interaction between cosmic rays and CMB, another one may originate from particular phenomena like AGNs. There are also some fluxes predicted for theories beyond Standard Model, but they are not discussed in this work.

In this thesis the search of an astrophysical signal in ANTARES data is performed. The first chapter is dedicated to the high energy astronomy, analyzing the possible neutrino sources and the flux models associated. In the second chapter the detection mechanism is detailed, along with the particular signatures of different neutrino flavors. ANTARES experiment, with its layout and its possible background sources, is described in the third chapter. The fourth chapter deals with the Monte Carlo simulation system, taking into account the different software for event generation and track reconstruction used in the collaboration. The analysis chain is described in the fifth chapter, with a detailed description of sample selection and tests on the Monte Carlo. In the same chapter ANTARES sensitivity for Waxman-Bahcall and cosmogenic flux is estimated. The analysis chain is then applied on the full data sample in chapter six, in order to get a limit on the neutrino fluxes on which this work is focused.

Contents

List of Figures

Chapter 1

High Energy Astronomy

Astroparticle physics is a relatively young field derived from the extension of conventional astronomy beyond the optical to the microwave and X spectrum. This new field can explore universe using a different kind of messengers, relying on high energy cosmic rays, gamma rays and neutrinos.

This chapter deals with high energy cosmic rays, their spectrum and origin, to focus in particular on neutrino astronomy.

1.1 High Energy Cosmic Rays

The discovery of cosmic rays was made by Hess in 1912 [1] by three golden spectrometers placed in a free balloon at 5300 meters of altitude, finding that the level of radiation increased with height, contradicting the hypothesis of earth rock radioactivity. This opened the way to all the studies of the following decades with different kinds of detectors, from balloons to satellites. Detection of cosmic rays of higher energy becomes more difficult because of their low arrive frequency.

In 1938 Pierre Auger discovered the extensive air showers through a ground-based experiment, detecting the product of the cosmic ray interactions with atmosphere. The energy measured in these showers was some orders of magnitude greater than the one obtained in balloon experiments. New detectors on large scale were built to detect particles with these energies.

1.1.1 Cosmic Rays Composition and Spectrum

Cosmic Rays (CRs) spectrum is ranged between $\sim 10^9$ eV and $\sim 10^{21}$ eV. The largest part (almost 90%) of the incoming CR is made up by protons, while there is a 10% of alpha particles (helium nuclei) and a minor part

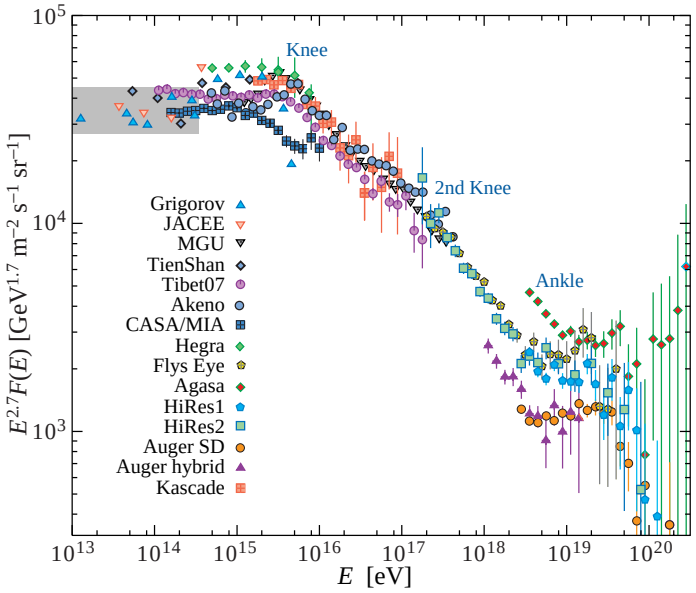

Figure 1.1: The all-particle spectrum from air shower measurements. The shaded area shows the range of the the direct cosmic ray spectrum measurements [2].

(almost 1%) of heavier elements, beta particles (electrons) and gamma ray photons. In CRs it is possible to find a composition similar to the one of the Solar System, even if there are some relevant differences. An abundance of nuclei with $Z > 1$ is visible in CRs and the contribution of two groups of elements, such as Li-Be-B and Sc-Ti-V-Cr-Mn, is more important than in the Solar System. The explication of this abundance lies in the collisions of heavier elements (C and O for the first group, Fe for the second one) with the interstellar medium, which produces lighter element through a process of spallation.

The energy spectrum spans over 13 orders of magnitude and follow approximately a power law, decreasing with the energy's increment. The differential flux can be expressed as following:

$$\frac{dN}{dE} \propto E^{-\gamma} \tag{1.1}$$

where N is the number of observed events, E is the energy of the primary particle and γ is called spectral index. The latter is about 2.7 until the energy reaches 3×10^{15} GeV, where the spectrum shows a *knee* and the spectral index steepens to about 3.1. The slope changes again at about 3×10^{19} GeV, when

γ steps back to 2.7. To summarize:

$$\gamma = \begin{cases} 2.67 & \log(E/eV) < 15.4 \\ 3.10 & 15.4 < \log(E/eV) < 18.5 \\ 2.75 & 18.5 < \log(E/eV) \end{cases} \tag{1.2}$$

Shielding by solar wind dominates for CRs below ∼10 GeV. Also, CRs with energy below ∼100 MeV are not able to reach the Earth.

Measurements above the atmosphere are required to detect CRs up to energy of $\sim 10^{14}$ eV. For this kind of CRs the acceleration is explained by the Fermi mechanism [3, 4]. These CRs seems to have a galactic origin, confirmed by experiments on satellites and stratospheric balloons, which had provided information also about the composition of CRS. Because of the randomization of original direction by the Galactic ($B \simeq 3\,\mu$G) and intergalactic (∼nG) magnetic fields, it is impossible connecting CRs with sources. The so-called gyro-radius for a nucleus with charge Z and energy E (eV) is:

$$R_{\rm gyro}(E) = \frac{E \times B_{\rm Galaxy}}{Z} \simeq 3 \times 10^{-16} \frac{E}{Z}\ [\rm pc] \tag{1.3}$$

For CRs with energy below the knee the value of $R_{\rm gyro}$ is comparable with the thickness of Galactic disc (≃200 pc) for a $Z = 1$ particle, such as a proton. This means that a source pointing is possible only for protons having $E > 10^{19}$ eV.

The knee in the spectrum is shown at about 3×10^{15} eV. There is still no unique explication for the spectrum's shape, even if several models had been proposed [7]. A possible phenomenological cause could be a cutoff energy to the CRs component, which should became iron-richer after the knee.

At energy above $\sim 10^{14}$ eV the CRs flux becomes even lower and the study of this spectral region are performed by big infrastructures located on the ground. These experiments can detect large showers of secondary particles produced by the CRs interaction with the atmosphere. KASCADE experiment has studied the region around the knee [8] and it seems to indicate that the average of CRs increases for energies above the knee.

At $\sim 10^{20}$ there is a second change in the spectrum, called the ankle. Above this energy the spectrum becomes flat and the CRs' origin is supposed to be extragalactic. There is no galactic source which can produce particles of such energy range and the gyro-radius of particles is large enough to make them escape from the galaxy [9]. In addition the particle diffusion is low if compared to the traveling path through the galaxy. It is possible to identify the source of this high energy particles. The isotropic distribution suggests that the traveling lenghts are longer than the galaxy's diameter.

The so-called GZK (Greisen-Zatsepin-Kuz'min) cutoff suppress the CRs flux above 6×10^{19} [10]. The cutoff is caused by the photo-interaction of proton with the 2.7 K Cosmic Microwave Background radiation. Observations by HIRES [11] and Auger [12] seem confirm the hypothesis. On the other hand the data from AGASA [13] experiment give no hints of this cutoff. The most recents analysis of Auger data cannot firmly establish the existence of GZK effect.

1.1.2 Acceleration mechanism

The high energy neutrino production is strictly bound to the CRs acceleration.

The Fermi mechanism explain the acceleration by iterative scattering process of charged particles in a shock-wave. The latter is originated by a very strong gravitational force, like in the proximity of a stellar collapse or a black hole. A particle goes through a stochastic acceleration, entering in the region with a certain E and exiting with a different one. The model proposes that the particle is accelerated by magnetic field inhomogeneities, increasing its energy in a proportional way ($\Delta E = \xi \times E$, where ξ is the gain).

There are two main configurations for the stochastic acceleration. The first configuration consider the acceleration zone as a moving gas cloud, where particles are scattered by the irregularities, with a random direction. The gain at the end of the acceleration is proportion to the squared cloud velocity, such as $\Delta E \propto \beta^2 E$. This is the second order Fermi acceleration mechanism.

In the first order acceleration mechanism the shock wave front is considered plane and infinite. The particles are accelerated going back and forth between the shock wave front. Being β the velocity of the shocked plasma flow, the energy is increased of $\Delta E \propto \beta E$. This is dependent on the velocity's direction, but is much more efficient than the second order mechanism, which has a $\beta \sim 10^{-2}$.

Supernova explosions are the main Fermi accelerators and can give birth to particles with a maximum energy of 100 TeV. These accelerated CRs can interact or decay, producing gamma ray, positrons, neutrinos and so on.

However the SNR (Supernova Remnant) model fails to explain the flux above the knee, even if at the present days there is no better model up to 10^{19} eV. There are some hypothesis involving an acceleration by rotating neutron stars. The particles, already accelerated by a SNR shock, suffer an additional acceleration into the strong variable magnetic field of the neutron star. The maxim energy which can be reached is 10^{19} eV [14].

1.2 High energy γ-ray

Neutrino telescope are able to study the energy spectrum up to the ankle, where the Fermi mechanism fails to explain CRs acceleration.

In this spectral region pointing CRs sources is not possible because of the galactic magnetic fields. On the other hand, neutral particles such as γ and neutrinos do not suffer the magnetic fields action, but are produced during interaction or decay of charged particles. There is no direct acceleration for them.

Two models have been developed to explain the γ-ray production, one leptonic [15] and another adronic [16]. In the first case, electrons are accelerated, while in the adronic model there is an acceleration for protons or nuclei. The lepton model wants high energy γ-rays produced in synchrotron radiation, bremsstrahlung and Inverse Compton (IC) scattering. The interaction between electrons and background photons is able to produce γ-ray via IC scattering with a high efficiency. The adronic model relies on γ production in neutral pions decay. In this particular scenario also charged pions are present, associated with the production of high energy neutrinos.

EGRET (Energetic Gamma-Ray Experiment Telescope) experiment has compiled a catalog from the 1990s with γ-ray sources in the MeV $\div$ GeV range [17]. The cataloger contains 271 sources with high significance, even if the largest part of them are not identified.

In June 2008 the Fermi Gamma-ray Space Telescope (Fermi) has been launched, with the goal of producing a new and more accurate skymap in the γ spectrum. At the GeV energies, Fermi has increased the number of known sources by nearly an order of magnitude in its first year of operation, confirming observationally some theorized γ-ray emitters [18]. In Figure 1.2 the new skymap is shown.

Satellites experiments are not sufficient for the low γ-ray fluxes above 100 GeV. High energy γ-rays interact with Earth's atmosphere and produce a cascade of high energy relativistic particles, which are able to emit Cherenkov radiation. The latter, formed by visible light and UV, can be detected at ground level by arrays of telescopes equipped with photomultipliers. By the Imaging Air-Cherenkov Technique (IACT) it is possible to reconstruct the shower and inquire the direction and energy of the primary photons.

The first experiments using the IACT method are Whipple [19], HEGRA [20], CANGAROO [21] and CAT [22]. In these days the modern experiments are HESS [23], VERITAS [24] (array telescopes) and MAGIC [25]. These telescopes have provided a large catalog of TeV γ-ray sources.

After the TeV spectrum, infrared, radio and microwave photons pose a limit to the mean free path. Above 10 TeV the horizon of photons is limited

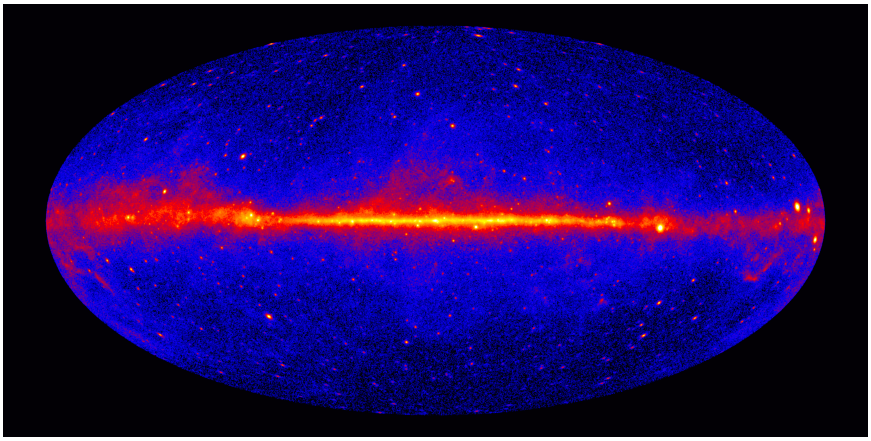

Figure 1.2: All-sky gamma-ray map from two years of Fermi LAT data, in Galactic coordinates and Aitoff projection. The color scale indicates the number of photons with energy greater than 1 GeV detected per pixel in the first twenty-four months of LAT operation. Diffuse Galactic emission is evident as a bright red band across the Galactic plane. This diffuse emission is produced by cosmic rays colliding with diffuse gas in the Milky Way, and by inverse Compton scattering of background starlight by energetic electrons. Bright point sources are visible both within the Galactic disk (predominantly pulsars, pulsar wind nebulae, and supernova remnants) and outside of it (predominantly AGNs, along with some millisecond pulsars). Many of the point sources are still unidentified [18]

to less than 10 Mpc.

1.3 Neutrino Astronomy

This part will deal with neutrino astronomy and its advantages and disadvantages, in order to explain why the neutrino is a good messenger and which are the mechanisms for neutrino production in the universe.

1.3.1 The choice of neutrinos

Neutrinos are stable particles and their neutral charge assures a straight trajectory from the source across the universe. On the other hand neutrinos can interact only through weak interaction. Their small cross section ($\sim 10^{-34}$ cm^2) allow them to cross big portions of space without interact, also through zones full of matter which can stop other messengers, such as photons or protons. This property implies also great volumes for neutrino detection.

Neutrinos can also bring new information about the most violent phenomena in the universe.

1.3.2 Production's mechanism

The main way to product neutrino is via hadronic interactions in matter. Hadronic interactions create pions whose decay implies neutrinos:

$$\begin{array}{rcl} \pi^+ & \longrightarrow & \mu^+ + \nu_\mu \\ & \longrightarrow & \overline{\nu}_\mu + e^+ \nu_e + \nu_\mu \\ \pi^- & \longrightarrow & \mu^- + \overline{\nu}_\mu \\ & \longrightarrow & \nu_\mu + e^- + \overline{\nu}_e + \overline{\nu}_\mu \end{array} \tag{1.4}$$

Neutrino generated in this process have a ratio $(\nu_e : \nu_\mu : \nu_\tau) = (1 : 2 : 0)$. Oscillations mechanism changes this proportion to $(1 : 1 : 1)$ when neutrinos reach Earth.

Having no electric charge, neutrinos cannot be accelerated after production. In this way hadrons must have a high energy, in order to justify the energy of neutrinos observed on Earth. Phenomena which can product such high energy hadrons are Fermi mechanism for supernovae of first and second order.

During first order acceleration, particles trajectories are bent by magnetic fields inside the wavefront. Particles travel in the same direction of the wavefront, having the rear wavefront a speed $\vec{u}_1$ greater than $\vec{u}_2$ for the front

one. Particles are magnetically reflected between the two wavefront, gaining an energy proportional to $|\vec{u}_1 - \vec{u}_2|$ before escaping the shock region.

Second order process is a stochastic particle acceleration. Particles gain and lose energy in random way inside magnetic matter's clouds, i.e. supernova remnants. These clouds moves through the space and their movement gives birth to a magnetic field that can give particles an energy contribution proportional to $|\vec{u}_1 - \vec{u}_2|^2$, being $\vec{u}_1$ and $\vec{u}_2$ the velocities for the two magnetic regions.

1.3.3 Neutrino sources

Neutrino astronomy is still a developing field. There are different sources which are good candidates for neutrino sources. These ones are investigated at Earth by Cherenkov telescopes.

1.3.3.1 Local sources

The nearest astrophysical neutrino source is the sun. It can product neutrinos by internal nuclear reactions. Neutrino energy is quite low ($\sim$MeV) and such flux can be investigated by smaller detector, as in the last forty years, from Homestake experiment until SuperKamiokande.

Atmospheric neutrinos are generated in the cosmic ray interactions with atmosphere. Even if cosmic rays are of extraterrestrial origin, neutrino production is considered local. The first and main contribution comes from the long lived particle disintegration, such as pions and muons ($10^{-8} - 10^{-6}$ s). The prompt contribution is from short lived particle disintegration (charmed hadrons, 10^{-12} s).

Energy spectrum for atmospheric neutrinos is very similar to the cosmic ray one ($E^{-2.7}$) until 100 GeV. Beyond this energy the spectral index becomes -3.7, decreasing quickly. Neutrinos form prompt contribution follow a slope $\propto E^{-2.7}$ until higher energies, 10-100 PeV, because of even higher hadron's energy.

1.3.3.2 Galactic sources

All the cosmic rays up to the ankle are supposed to be of galactic origin. These kind of sources are quite near the Earth (orders of 10 kpc). Some of them are very likely to be neutrino sources, since the complementary observations from γ-ray telescopes can not be explained by leptonic models alone.

Neutrinos form galactic disc: cosmic rays can interact with interstellar gas, whose main concentration is inside the galactic disc. These interactions create mesons which decay into neutrinos and other particles. These neutrinos are called diffuse because they have no information about their direction. Energy spectrum should follow the cosmic ray one, $E^{-2.7}$ until the most high energies.

Supernova remnants: supernova explosions are catastrophic events caused by gravitational collapse of a star at the end of her life, when all the element until iron had already been burnt. A supernova explosion can throw out an enormous quantity of energy in few time. The largest part of this energy is sent out as MeV neutrinos. After the explosion hadrons can be accelerated until PeV by Fermi mechanism. These high energy particles can interact with the medium and product other neutrinos. Final product of a supernova can be a neutron star, so the already accelerated particles can gain additional energy due to its strong magnetic fields.

In spite of the low expected explosion rate (2-4 per century), significant flux of high energy neutrinos can be produced during the short period after the explosion. In addition, these events will arrive in a short time window, which makes their detection easier.

Pulsar Wind Nebulae: it is a kind of stellar wind powered by magnetic fields from a pulsar, which blows put jets of very fast moving material into the nebula. These emissions are of synchrotron origin, according to radio, optical and X-ray observations, such as the case of the TeV γ-ray emission from the Vela PWN (Vela X) observed by HESS telescope.

Neutrino fluxes from these objects could be observed by a kilometer-scale neutrino telescope.

Microquasars: they are the best galactic candidates for neutrino astronomy. They are galactic X-ray binary systems composed of an accretion massive object such as a black hole or a neutron star and a companion star which provides mass to the firs one. They also display relativistic radio-emitting jets, probably caused by the accretion of matter from the companion star. Micro-quasar are quite like AGN, but at a much smaller scale.

Binary systems: a binary star is a neutron star or a black holes that increases by its companion's material and a fraction of this material is emitted as a couple of jets aligned with the stellar axis. These jets are naturally

region of acceleration for particles because of the collisions between particles. Moreover, in these regions there are strong magnetic fields.

To detect these neutrinos is mandatory to be in axis with one of the two jets. For this reason this kind of flux is considered as diffuse.

Neutrinos from Galactic Center (GC): Galactic Center is within the sky view with the latitude of the Mediterranean, so it is very interesting for the ANTARES experiment.

Inside the GC region a γ-ray spectrum described by a power law with spectral index of $\sim$2.3 has been measured. This fact indicates a local CR spectrum in the GC region which is much harder and denser than that measured on Earth. It could be due to an additional component to the CR population, above the standard concentration which fills the Galaxy.

Fermi Bubbles In the last years Fermi-LAT satellites has detected γ-rays with an hard and relatively uniform energy spectrum. This emission can be shaped as two bubbles in a region centered in the core of the Milky Way. They are perpendicular to the galactic plane and have an extension of 10 kpc. It is widely though that Fermi Bubbles can be neutrino sources [30] and these neutrinos should detectable by a km-scale telescope [31].

1.3.3.3 Extragalactic sources

Cosmic rays above the ankle are assumed to be of extragalactic origin. Therefore the existence of extragalactic high energy neutrino sources is directly implied by CR observations. Neutrinos can be produced in the same mechanism that accelerates hadronic particles, such as protons or nuclei.

While dealing with high energy cosmic rays, one must take into account the GZK cutoff, which imposes a theoretical upper limit on the energy of cosmic rays from distant sources. Auger experiment has rejected the hypothesis of a power low for CRs with $E > 6 \cdot 10^{19.6}$ eV, with a 6 sigma significance [26], as shown in Fig. 1.4. The main source for this kind of CR could be active galactic nuclei (AGN), even if sources distributed among the nearby galaxies are not excluded.

Neutrinos from the cosmic background radiation: all the CR interaction with the microwave background radiation of 2.7 K, which can be considered as a neutrino source both galactic and extragalactic. This kind of interaction produces pions via Δ^+ (1232) resonance. Pions decay gives birth to a neutrino flux with a energy higher than 10^8 GeV.

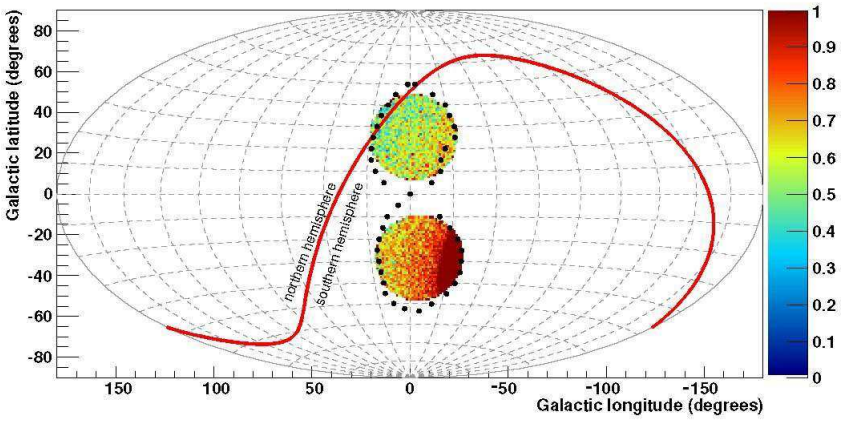

Figure 1.3: Galactic coordinates of simulated neutrino from the Fermi bubbles. The color code indicates the fraction of Monte Carlo neutrinos that are up-going in local detector coordinates. The measured bubble edges are also reported (black points). The red line represents the separation line between the northern and southern hemisphere [31].

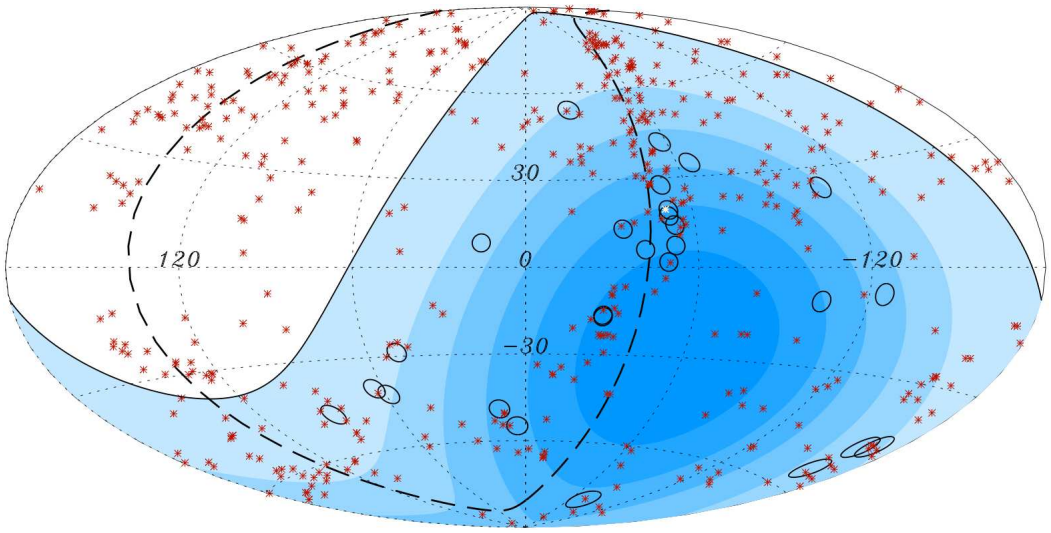

Figure 1.4: Aitoff projection of the celestial sphere in galactic coordinates with circles of radius 3.1° centered at the arrival directions of the 27 cosmic rays with highest energy detected by the Pierre Auger Observatory. The positions of the 472 AGN (318 in the field of view of the Observatory) with redshift $z \leq 0.018$ ($D < 75$ Mpc) from the 12^{th} edition of the catalog of quasars and active nuclei are indicated by red asterisks. The solid line represents the border of the field of view (zenith angles smaller than 60°). Darker color indicates larger relative exposure. Each colored band has equal integrated exposure. The dashed line is the supergalactic plane.

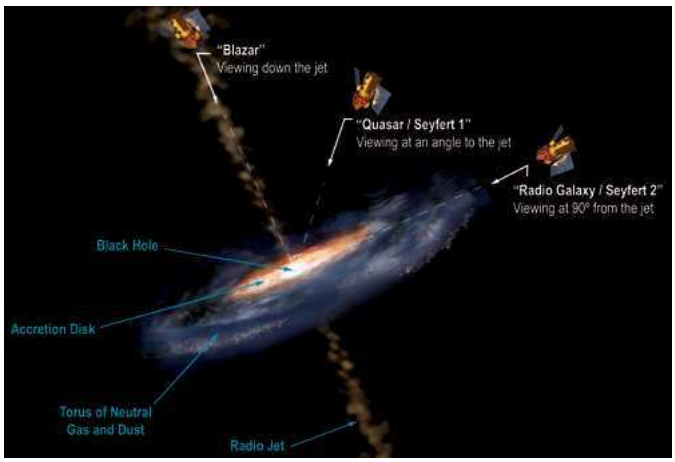

Figure 1.5: Scheme of an AGN. It is indicated which objects are believed to be seen from particular directions.

Neutrinos from AGN: galaxies with a very bright core of emission in their center are called Active Galactic Nuclei. They are 5% of the galaxies in the universe. There could be a supermassive black hole in the centre of these galaxies.

A schematic view of an AGN can be seen in Fig. 1.5.

The supermassive black hole, with a mass $10^6 \div 10^9$ times the Sun, would attract material in the center of the AGN and release a large amount of gravitational energy. Matter from dust torus feds the accretion disk. Is it possible to observe two jets, both perpendicular to the accretion disc.

These jets are particle accelerators. The outgoing beams can interact with the ambient matter and photons. ANG appear very bright when one of the jets is oriented along the line of sight: in this case it is called *blazar* and is one of the best chances to detect a neutrino point source.

The AGN mechanism can generate an energy rate greater than $L > 10^{47}$ erg s^{-1} and thus an AGN is the brightest steady source. AGN are believed to be high energy neutrino sources.

Neutrinos from Gamma Ray Bursts: this phenomenon has been discovered in the 1960s and is characterized by a brief flash of γ-rays, often followed by X-ray, optical and radio emission which carries out most of the energy as > 1 MeV photons. A GRB can last from few milliseconds to tens of seconds.

Among the models which can explain GRBs, the most accepted is the *fireball* model (Fig. 1.6). It is assumed that matter moving at relativistic

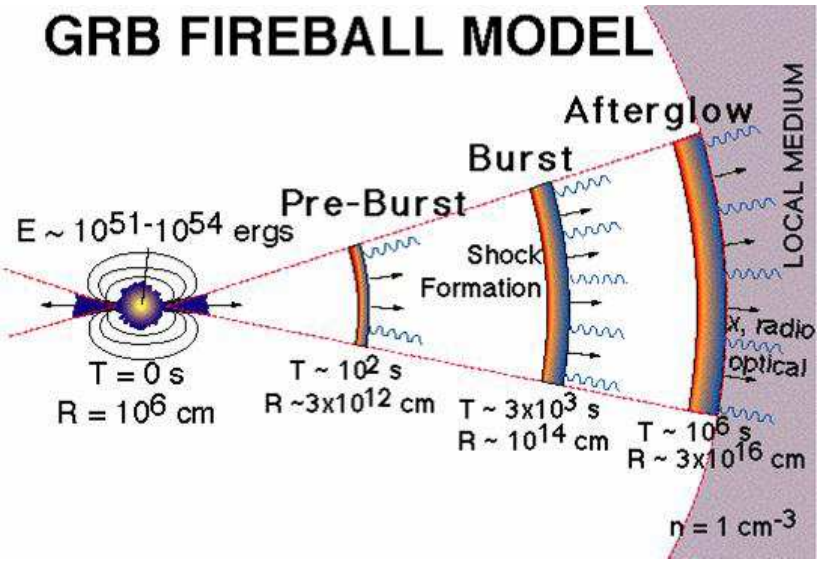

Figure 1.6: The GRB fireball model. Moving material at relativistic speeds ($\Gamma \sim$300) which interacts with the surrounding medium produces γ-rays and the afterglow.

speed, under the powering of radiation pressure, collides with other material in the proximity. The origin of the radiation pressure is still unknown, but it is thought to be a collapse of massive object to a black hole. Assuming that the fireball produced in the collapse has a high relativistic velocity (Lorentz factor $\Gamma \sim 300$), the protons accelerated within the shock wave lose energy through interactions with ambient photons. The high photonic density grants a high collision rate between photons and protons. This yields to a significative pion's production. The pions later decay in neutrinos carrying the 5% of the original proton energy, $E_\nu \sim 10^{14}$ eV [27]. Neutrino contribution can be different depending on the GRB evolution.

The advantage of this kind of transient sources is that they are almost background-free, being the emitted neutrinos correlated in time and direction with γ-rays. Being the average energy $\sim$ 100 TeV, a kilometer-scale neutrino telescope could be sufficient for their detection [28].

1.4 Diffuse ν fluxes

All the sources previously listed can be observed performing an individual pointing search. This procedure is quite difficult for detectors with a volume smaller than one kilometer cube.

However there is another way to have an evidence of high energy neutrino sources. In order to face the very low ration of events from individual sources, a cumulative neutrino flux from unresolved sources is searched. This is commonly known as neutrino diffuse flux.

There is no need for directional information when searching the diffuse flux. An excess of high energy events over the atmospheric spectrum is a signal of it.

A theoretical upper bound can be set relying on diffuse flux of γ-rays and UHECRs. Neutrinos and high energy γ-rays are produced in parallel from the decay of pions (charged in the first case, neutral in the second), but neutrinos have a larger probability to escape the source, due to their low cross section. The observation of the γ-ray flux can put a limit on the neutrino flux, taking into account the branching ratios and kinematics at the source.

The diffuse γ-ray flux measured by EGRET above 30 MeV has the spectrum shown in Eq. 1.5 [29]:

$$E^2 I_\gamma(E) = (1.37 \pm 0.06) \times 10^{-6} \left[\text{GeV cm}^{-2}\text{sr}^{-1}\text{s}^{-1}\right] \tag{1.5}$$

so the theoretical neutrino flux should have an upper bound of the same order of magnitude.

A similar upper bound can be deduced from extragalactic CRs, under the assumption that nucleons can escape from sources. In case of Fermi mechanism, protons are magnetically confined near the source. On the other hand, neutrons produced by protons' interaction are able to escape and decay again in protons outside the acceleration region.

There are still other factors to take account of in this relationship between neutrinos and CRs, such as the production kinematics, the opacity of the sources to neutrons and the effect of propagation. The last one is the greatest source of uncertainty because it is strongly dependent from the galactic evolution and the poorly known magnetic fields in the Universe.

1.4.1 The Waxman-Bahcall upper bound

The constrain on neutrino flux proposed by Waxman and Bahcall [32] [33] uses the observation on cosmic rays at $E_{\text{CR}} \sim 10^{19}$ eV as a constraint on the neutrino flux. There are some hypothesis to be made in order to obtain this upper limit:

- neutrinos are produced by interaction of proton with ambient radiation or matter;

- sources are transparent to high energy neutrinos ($E_\nu \sim 10^{19}$ eV), the so-called optically-thin proton accelerators;
- highest energy cosmic rays produced in neutron decay are not deflected by magnetic fields;
- the spectral shape of CRs up to the GZK cutoff is $dN/dE \propto E^{-2}$, typical of Fermi mechanism.

Considering that protons are accelerated by a Fermi mechanism in the energy range $10^{19} - 10^{21}$ eV, the energy injection rate of cosmic rays is given by:

$$E_{\rm CR}^2 \frac{d\dot{N}_{\rm CR}}{dE_{\rm CR}}\bigg|_{E_0} = \frac{\dot{\epsilon}_{\rm CR}}{\ln(10^{21}/10^{19})} \simeq 10^{44}\ {\rm erg\ Mpc^{-3}yr^{-1}} \tag{1.6}$$

assuming that the energy spectrum has a shape of E^{-2} and the starting at the sources energy is $E_0 = 10^{19}$ eV.

High energy protons produces by sources out of the galaxy lose a fraction $\epsilon < 1$ of their energy due to photomeson production of pions before escaping the source. In this way the produced energy density for muon neutrinos is:

$$E_\nu^2 \frac{dN_\nu}{dE_\nu} \approx \frac{3}{8}\epsilon_\pi t_H E_{\rm CR}^2 \frac{d\dot{N}_{\rm CR}}{dE_{\rm CR}} \tag{1.7}$$

where t_H is the Hubble time and ϵ_π is the fraction of energy injected in protons and lost during photo-pion interaction. The factor 3/8 that a half of the generated pions is neutral and they do not produce neutrinos in their decay. If it is considered $\epsilon = 1$, a muon neutrino intensity can be defined as the following:

$$I_{\rm max} \approx \frac{3}{8}\xi_Z t_H \frac{c}{4\pi} E_{\rm CR}^2 \frac{d\dot{N}_{\rm CR}}{dE_{\rm CR}} \approx 1.5 \times 10^{-8} {\rm GeV\ cm^{-2}s^{-1}sr^{-1}} \tag{1.8}$$

where the quantity ξ_Z describes the possible contribution of high redshift sources of cosmic rays and includes the effect of redshift in neutrino energy. At high redshift the generation rate of cosmic rays may have been higher, so it could be necessary to introduce a correction factor:

$$\xi_Z = \frac{\int_0^{z_{\rm max}} dz\, g(z)(1+z)^{-7/2} f(z)}{\int_0^\infty dz\, g(z)(1+z)^{-5/2}} \tag{1.9}$$

where z is the redshift, $g(z)$ is a weak function of redshift and cosmology (equal 1 for a flat universe with zero cosmological constant) and $f(z) =$

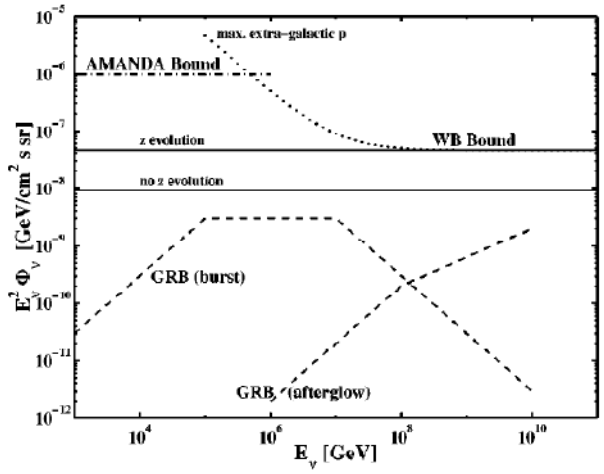

Figure 1.7: Comparison of muon neutrino intensities (ν_μ and $\overline{\nu}_\mu$ combined) predicted by different models with the upped bound implied by cosmic ray observation. The solid lines give an upped bound the case of evolution and no evolution, corrected for neutrino energy loss due to redshift and for possible redshift evolution of the cosmic ray generation rate. The component due to GRB is estimated in case of pure burst and afterglow. For comparison, the limit fixed for the AMANDA experiment is reported [32].

$(1+z)^3$ at low redshift. In this way, with weak dependent on cosmology, it could be approximated $\xi_Z = 3$.

Under the previous assumptions, the upper limit is:

$$E_\nu^2 \frac{d\Phi}{dE_\nu} < 4.5 \times 10^{-8} \text{ GeV cm}^{-2}\text{sr}^{-1}\text{s}^{-1} \tag{1.10}$$

Despite this limit may be out of date, due to hidden or optically thick sources for protons to interactions like $p\gamma$ or $pp(n)$, the Waxman-Bahcall limit is still took as a reference threshold for large volume neutrino detector.

1.4.2 The Mannheim-Protheroe-Rachen upper bound

The main problem of Waxman-Bahcall flux is the model dependency, because the largest part of the observations had been made under the choice of the spectral index $\alpha = 2$. This bound does not apply to models where the proton photo-meson optical depth is much greater than one. There is another upper limit, proposed by Mannheim and others [34], derived using also the γ-ray diffuse flux. Both opaque and transparent sources are taken into

account, while sources partially transparent to neutrons give an estimation of intermediate limits.

For sources opaque to neutrons, the limit is:

$$E_\nu^2 \frac{d\Phi}{dE_\nu} < 2 \times 10^{-6} \text{ GeV cm}^{-2}\text{sr}^{-1}\text{s}^{-1} \tag{1.11}$$

The limit is two order of magnitude smaller than the Waxman-Bahcall one. This is due to source opaque to neutrons produce a small amount of cosmic rays, because neutrons cannot escape and decay outside the source. On the other hand, the source is transparent to neutrinos and γ-rays.

1.4.3 Cosmogenic neutrinos

A very high energy neutrino flux can be derived by the propagation oh high energy nuclei on cosmological distances [35]. There are different hypothesis of neutrino flux, depending of the starting particle, being it a proton or an heavier nucleus. Present studies of cosmic ray composition indicate a dominance of heavier nuclei (from ^{4}He to ^{56}Fe) around the knee region ($\sim 10^{16} - 10^{17}$ eV) followed by a tendency toward lighter nuclei around $\sim 10^{18}$ eV and above. A way to confirm this hypothesis is the study of very high energy neutrinos produced after nuclei interactions. Cosmic rays at the highest energies produce pions off the cosmic microwave background (CMB) giving rise to the Greisen-Zatsepin-Kuzmin feature in the cosmic ray spectrum [10]. The decay of the charged pions produced by the interactions with the CMB generates neutrinos that are often called cosmogenic, GZK, or photopion neutrinos.

Even if most predictions of the cosmogenic neutrino flux assume that the UHECR primaries are protons, recently other cosmogenic neutrino fluxes were calculated for other primaries such as pure ^{56}Fe, ^{4}He, and ^{16}O.

1.4.3.1 Mixed composition and sources evolution

To predict neutrinos production, two UHECR injection compositions must be taken into account: pure proton and mixed composition. The source is assumed to emit a power law spectrum with spectral index α such that the number of nuclei i emitted in the energy range $[E, E + dE]$ is:

$$n_i(E) = x_i A_i^{\alpha-1} \kappa E^{-\alpha} dE \ , \tag{1.12}$$

where A is the mass number of a given nucleus, κ is a normalization constant, and x_i is the abundance of species i. The maximum energy at injection of each species is set to

$$E_{max,i} = Z_i E_{max}(^1H) \ , \tag{1.13}$$

i.e., the maximum energy is proportional to the charge number Z of a given nucleus. This assumption is reasonable if the maximum energy at the source is limited by the confinement of particles. For the neutrino flux calculation, the maximum proton energy is set to $E_{max}(^1H) = 10^{20.5}$ eV for the pure proton case and use the same input $E_{max}(^1H)$ in Eq. 1.13 to set the mixed composition case, which gives a maximum energy for iron of $\sim 10^{22}$ eV.

The predicted neutrino flux is strongly dependent on the choice of source redshift evolution. Difference source evolution models could be taken into account. The simple one previews no evolution with redshift, also called uniform distribution. A more evolved model considers a redshift dependence proportional to the old estimate of the star formation rate (SFR), which could be more on less severe, depending on the redshift z.

1.4.3.2 Interactions of protons and nuclei with photon backgrounds and neutrino emission

Protons and nuclei can interact with the CMB and the infra-red, optical and ultraviolet backgrounds (IR/Opt/UV for short). Even if the effect of IR/Opt/UV photons on the propagated UHECR spectrum of pure proton sources is negligible, these additional backgrounds have a significant effect on the neutrino flux associated with UHECRs.

In general, the IR/Opt/UV has a much milder cosmological evolution when compared to the CMB. The UV background gets fainter at lower redshifts due to the aging of the stellar population which results in the death of the stars with the shortest lifetimes which produce all of the UV emission. The basic reason is that most galaxies were forming stars at much higher rates at z=1 than they are today.

Protons and nuclei propagating in the extragalactic medium interact with CMB and IR/Opt/UV background photons. These interactions produce features in the propagated UHECR spectrum such as the GZK cutoff [10] and their decay products generate the cosmogenic neutrino flux. The evolution of the mean free path with redshift is strong in the case of the CMB, which implies that the dominant background strongly depends on the source evolution assumed. It is also important to note that the photo-pion production off IR/Opt/UV photons competes with the pair production process off CMB photons which is also evolving with redshift. At very high energies (above $\sim 5 \times 10^{19}(1+z)$ eV) the CMB contribution starts to dominate the mean free path evolution and the effect of the IR/Opt/UV photons becomes negligible.

The photopion production process off the IR/Opt/UV background has little effect on the predicted UHE proton spectra. Indeed, as soon as the pair production threshold with the CMB is reached, the photopion production

with IR/Opt/UV photons is completely subdominant and can be neglected in the calculation of UHECR with pure proton sources.

The interactions experienced by nuclei with photon backgrounds are different from the proton case. Pair production results in a decrease of the Lorentz factor of the UHE nucleus, whereas at higher energies, photodisintegration (also called photoerosion) processes lead to the ejection of one or several nucleons from the nucleus. Different photoerosion processes become dominant in the total interaction cross section at different energies. The lowest energy disintegration process is the Giant Dipole Resonance (GDR) which results in the emission of one or two nucleons and α particles. The GDR process is the most relevant as it has the highest cross section with thresholds between 10 and 20 MeV for all nuclei.

Around 30 MeV in the nucleus rest frame and up to the photopion production threshold, the quasi-deuteron (QD) process becomes comparable to the GDR and dominates the total cross section at higher energies. The photopion production (or baryonic resonances (BR)) of nuclei becomes relevant above 150 MeV in the nuclei rest frame (e.g., $\sim 5 \times 10^{21}$ eV in the lab frame for iron nuclei interacting with the CMB). It is important to note that photopion cross sections for nuclei are different from the free nucleon case. In particular, in nuclei the baryonic resonances heavier than the first Δ resonance are far less pronounced than for nucleons and the cross sections are not simply derived from the free nucleon case.

Pair production and photoerosion processes contribute to the total attenuation length of iron nuclei. Photoerosion processes dominate through most of the energy range and the effect of pair production is small at low redshifts. Although the competition between pair production off the CMB and photoerosion processes with IR/Opt/UV photons depends on the redshift (e.g., at high redshifts pair production increases due to the strong evolution of the CMB), the propagation of nuclei is mainly dominated by photoerosion processes. the attenuation length of low mass nuclei are smaller than that of protons and heavy nuclei and, as a consequence, light nuclei should not contribute as significantly at the high energy end of the spectrum. Furthermore, iron nuclei have larger or similar attenuation lengths to protons up to 3×10^{20} eV.

Neutrinos are also produced by the photopion production of protons and neutrons: $N + \gamma \rightarrow \Delta \rightarrow N' + \pi$ (where N is a nucleon). Photopion production through the delta resonance has a 1/3 probability of isospin flip of the incoming nucleon, and each isospin flip leads to the production of three neutrinos. For example, in the case of proton interactions producing π^+, $p + \gamma \rightarrow \pi^+ + n$, the π^+ decay generates one ν_μ, one ν_e+ and one $\overline{\nu}_\mu$.

In the case of nuclei propagation, neutrinos can also be produced via the

photopion production of nuclei. The treatment of this component is more uncertain complicated by pion interactions within the nucleus. To a good approximation, the pion production can be treated as the production of free nucleons, but the energy losses of the pion inside the nucleus have to be taken into account. The transfer of the initial kinetic energy of the pion to the spectator nucleons is partly responsible for the high multiplicity of ejected nucleons from this process. Furthermore, the produced pion can also be absorbed by a pair of nucleons before leaving the nucleus. If the pion is not absorbed, we remove 40 MeV of kinetic energy in the nucleus rest frame per participant nucleon before calculating the energy of the produced neutrinos.

1.4.3.3 Neutrino fluxes for cosmological distributions of sources

The proton spectra and the presence of a pair production dip are only mildly dependent on the source evolution hypothesis. The amplitude and the energy of the pair production dip minimum (around $10^{18.7}$ eV) only slightly depend on the evolution. However, the beginning of the dip is determined by the transition between the adiabatic and the pair production losses, which is more sensitive to the density of sources at high redshifts.

In the mixed composition case, the transition from galactic to extragalactic components ends at the ankle. The transition point and the spectrum above $10^{18.5}$ eV is quite insensitive to the source distribution. At energies below the ankle, the galactic fraction that completes the total observed spectrum depends on the source evolution, as in the case of pure proton models below 10^{18} eV.

1.4.3.4 Neutrino fluxes for pure proton sources

Neutrino fluxes for a pure proton composition and four different source evolutions are displayed on Fig.1.8 on the left where it is clear that the source evolution is a critical parameter. At high energies, $\sim 10^{18}$ eV, the neutrino flux for a uniform distribution of sources is almost one order of magnitude below the other hypotheses.

The contribution of the CMB and IR/Opt/UV backgrounds is detailed for the strong evolution case on the right of Fig.1.8. At low energies, the neutrino flux is dominated by the contribution of the IR/Opt/UV backgrounds and the flux is much higher than at higher energies. Although the interaction probability with the IR/Opt/UV backgrounds is much lower than with the CMB, the number of particles that are able to interact is much higher due to the steep injection spectra provided by acceleration mechanisms in

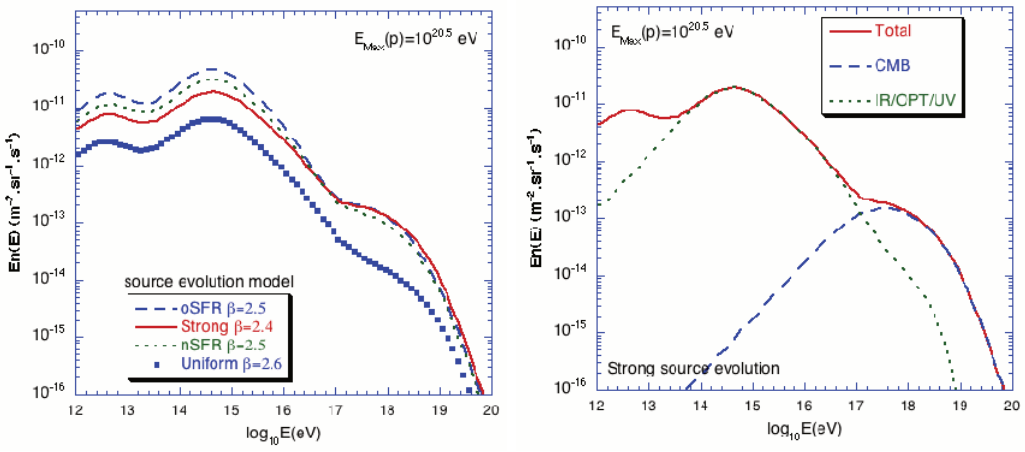

Figure 1.8: Left: Total neutrino flux from pure proton sources and four source evolution hypotheses. Right: Contribution of the different backgrounds to the neutrino flux for a strong source evolution hypothesis. The photopion interactions with CMB (dashed line) and IR/Opt/UV (dotted line) are shown and the difference between the sum of the two contributions and the total is the neutron decay component [35].

astrophysical sources. The CMB contribution generates a peak at $\sim 10^{17.6}$ eV, while the peak at $\sim 10^{14.5}$ eV is due to the IR/Opt/UV contribution. The position of the peaks depends on the combination of the evolution of the interaction probability and the injection spectrum.

1.4.3.5 Neutrino fluxes for a mixed composition

In the case of a mixed composition, the expected neutrino flux is shown in Fig.1.9a for the different source evolution hypotheses. At high energies, the flux is very similar to the pure proton case.

In the case of a strong evolution, the contribution of protons, He, and Fe nuclei to the total flux are displayed on the left of Fig.1.9. Above 10^{15} eV, the main contribution is due to protons ($\sim 65\%$), the second contribution comes from He, and Fe nuclei contribute only of a few percent over the whole energy range. Due to the harder spectral index, the intermediate energies peak for the proton component in Fig.1.9 (on the right) is slightly shifted towards higher energies (to $\sim 10^{15}$ eV), when compared to the corresponding peak in the pure proton case. The intermediate energy peak for the total flux from all the species is again around $\sim 10^{14.5}$ eV due to the contribution of the other species which become dominant for energies below the proton peak. The neutron decay peak of the proton component is invisible on the

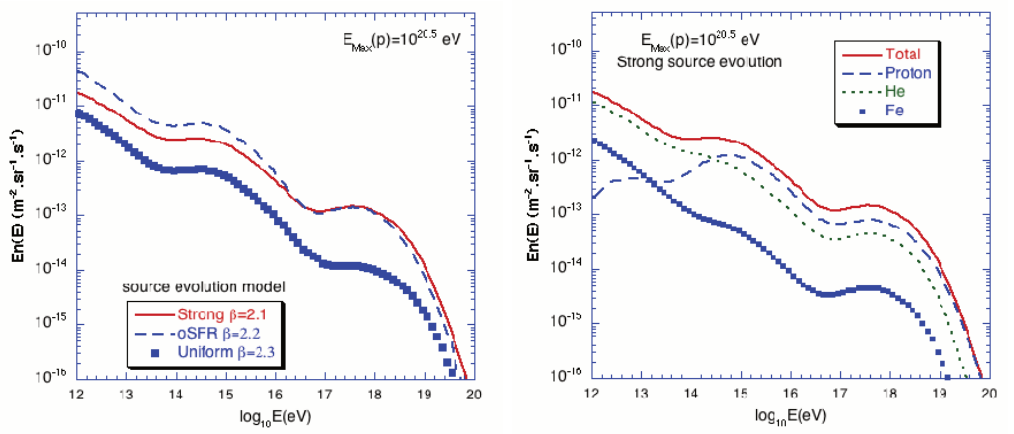

Figure 1.9: Left: Total neutrino fluxes corresponding a mixed composition and three source evolution hypotheses (the nSFR hypothesis is omitted). Right: Contribution of the different species to the neutrino flux for a strong source evolution hypothesis [35].

total flux as it is completely dominated by the nuclei contribution in this energy range. It is important to note however that the contribution of the different species is strongly dependent on the relative abundances assumed at the source. In our model, protons contribute $\sim 50\%$, helium $\sim 30\%$, and Fe $\sim 5\%$ at the source for a spectral index $\beta = 2.1$.

In the intermediate peak region around $10^{14.5}$ eV, the neutrino flux from nuclei originate mainly from direct pion production and neutron decay from secondary nuclei. Direct photopion production is the dominant process in the peak region, which may appear surprising since the GDR interaction probability (which is responsible of the nucleon emission) is higher than the photopion probability. However, for the photopion production of secondary nucleons, the neutrino emission requires first the emission of a nucleon and a subsequent photopion interaction of the emitted nucleon. At low energies, the realization of both of these requirements becomes less probable than a direct photopion interaction (despite the pion absorption probability), therefore, direct photopion dominates.

At the lower energies, below 10^{14} eV, the neutrino flux from nuclei is dominated by the contribution of secondary neutron β-decays. This component is far more important than in the case of primary protons as the interaction probability of nuclei (via the GDR process) is much higher. Unlike the secondary nucleon photopion component, the flux keeps increasing at lower energies as a subsequent interaction of the ejected nucleon is not necessary. The CMB contribution peaks around 10^{14} eV but is overwhelmed

by the IR/Opt/UV background contribution in the case of He nuclei. Neutrons with energies below 10^{16} eV can be ejected in contrast with the pure proton case where neutrons are produced following a photopion interaction of a proton, which does not occurs below 10^{16} eV even at high redshifts.

1.4.3.6 Comparison between the two composition hypotheses

The comparison between the pure proton and the mixed composition is displayed on Fig.1.10 for a strong source evolution hypothesis. For the other choices of source evolution, the comparison is qualitatively similar. At high energies, where detection is feasible, the fluxes are comparable. Changes in the detailed composition at the source or in the maximum energy reachable for the nuclei can slightly increase or decrease the predictions, but for a proton dominated mixed composition the flux at the highest energies is very close to the pure proton model. The similarity between the fluxes arises from the fact that the lower contribution of nuclei to the neutrino flux is compensated by the harder spectral index required to fit the UHECR data. Conversely, at lower energies, the higher fluxes expected for the pure proton scenario are mainly due to the softer spectral index that give a higher luminosity at low energies. In the intermediate energy range, detectability is limited by the atmosphere neutrino background for energies below 10^{15} eV. For energies between 10^{15} eV and 10^{17} eV, the pure proton case increases the chances of future detectability.

For the aim of this thesis, the pure proton flux will be used as a model for cosmogenic neutrinos.

1.5 ANTARES physics results

ANTARES telescope has already achieved some physical results for different phenomena. Here the most significant results are presented.

1.5.1 Diffuse flux

The search of signal coming from Waxman-Bahcall flux has been already performed with ANTARES telescope. The analysis has exploited 334 days of data taking, analyzed with a particular energy estimator to discriminate signal and background. The sensitivity for ANTARES has been estimated as:

$$E^2\Phi_{90\%} = 5.3 \times 10^{-8} \text{ GeV cm}^{-2}\text{s}^{-1}\text{sr}^{-1} \tag{1.14}$$

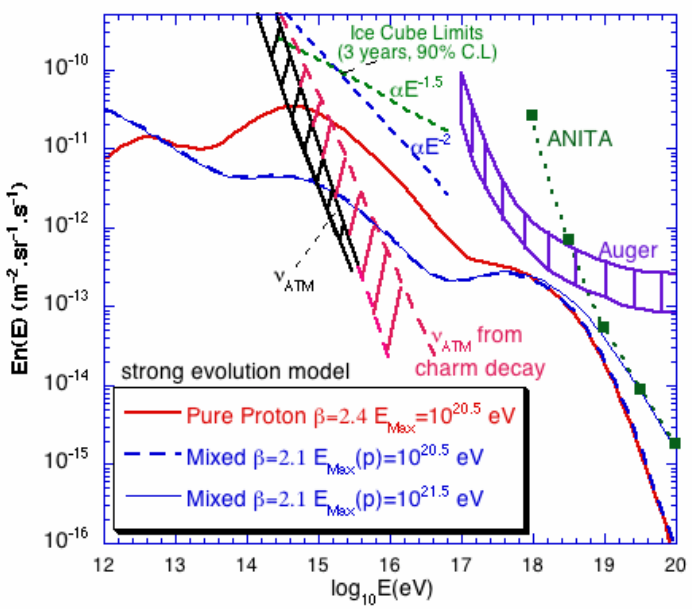

Figure 1.10: Predicted cosmogenic neutrino flux for pure proton and mixed composition in the case of the strong source evolution compared with the sensitivities of Auger (ν_τ) and ANITA at high energy and the limit of Ice Cube (for the ν_μ detection channel only) after three years of observation with 90 C.L. (assuming neutrino spectra $\propto E^{-2}$ and $E^{-1.5}$) at low energy, estimates of the atmospheric neutrino flux and atmospheric neutrinos due to charmed interactions are also displayed.

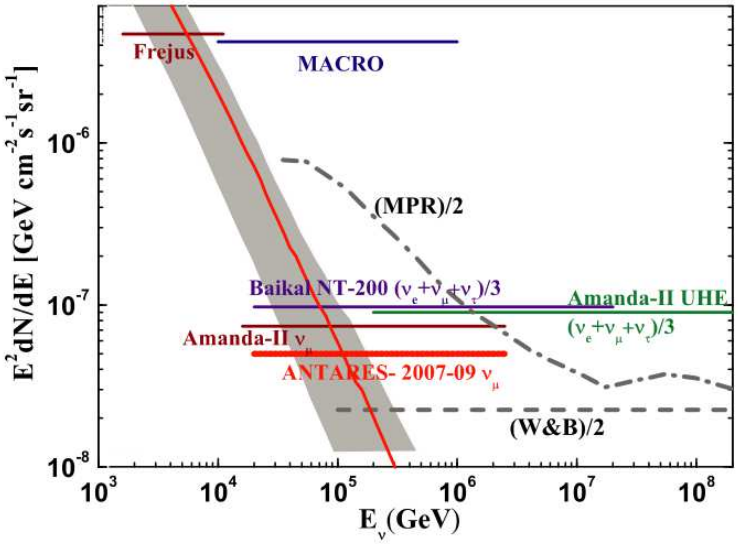

Figure 1.11: The ANTARES 90% c.l. upper limit for a E^{-2} diffuse high energy neutrinos and antineutrinos flux obtained in this work, compared with the limits from other experiments. The Frejus, MACRO, Amanda-II 2000-03 limits refer to muonic neutrinos and antineutrinos. The Baikal and Amanda-II UHE 2000-02 refer to neutrinos and antineutrinos of all flavours, and are divided by 3. For reference, the W-B and the MPR upper bounds for transparent sources are also shown. They are divided by two, to take into account neutrino oscillations. The grey band represents the expected variation of the atmospheric muonic neutrino flux: the minimum is the Bartol flux from the vertical direction; the maximum the Bartol + RQPM flux from the horizontal direction. The central line is averaged over all directions [37].

in the energy range 20 TeV-2.5 PeV, as can be seen in Fig. 1.11. Other models predicting cosmic neutrino fluxes with a spectral shape different from E^{-2} are tested and some of them excluded at a 90% C.L. [37].

1.5.2 Point source search

ANTARES has performed the search of an astronomical signal coming from a precise direction, exploiting the information on the position of the events inside the detector, the so-called point source analysis. A search on the period 2007-2010 (813 days) has been made, with two different analysis methods: within a list of candidate sources and in the whole sky. No statistically significant excess has been found in either cases, so 90% C.L. upper

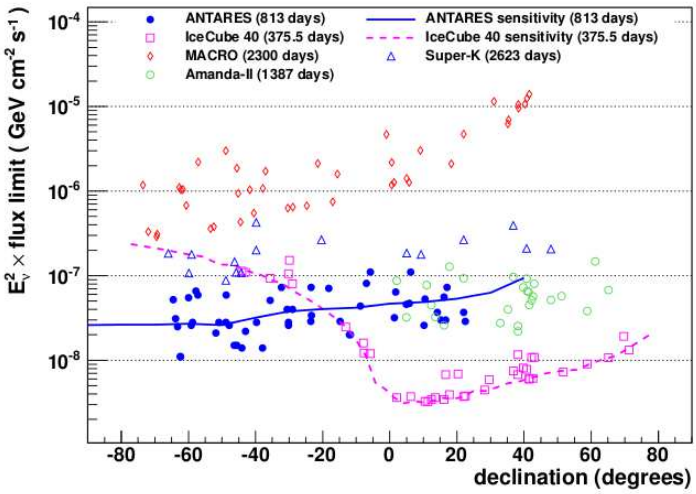

Figure 1.12: Limits set on the E_ν^{-2} flux for the sources in the candidate list. Upper limits, previously reported by other neutrino experiments, on sources from both Northern and Southern sky are also included. The ANTARES sensitivity of this analysis is shown as a solid line and the IceCube 40 sensitivity as a dashed line [**?**].

limits on the neutrino flux normalisation have been set at $1 - 10 \times 10^{-8}$ GeV cm^{-2} s^{-2} in the range from 4 to 700 TeV (80% of the signal, see Fig. 1.12), assuming an energy spectrum of E_ν^{-2}, and are the most restrictive ones for a large part of the Southern sky.

1.5.3 Magnetic monopoles

Magnetic monopoles are hypothetical particles first proposed by Pierre Curie and theoretically confirmed by Dirac. In certain spontaneously broken gauge theories, magnetic monopoles are not a possibility, but a requirement, leading to the quantization of electric charge.

Measurements and estimates of cosmic magnetic fields suggest that magnetic monopoles lighter than 10^{14} GeV could have been accelerated to relativistic velocities, acquiring typical kinetic energies of 10^{15} GeV. Magnetic monopoles are expected to lose energy significantly when crossing Earth due to their large equivalent electric charge ($g_D \simeq 68.5\, e$). Magnetic monopoles with mass below $\sim 10^{14}$ GeV would be detectable in a neutrino telescope after crossing Earth. For the refractive index of sea water ($n \sim 1.35$) fast monopoles are expected to emit about 8550 times more Cherenkov photons than muons of the same velocity.

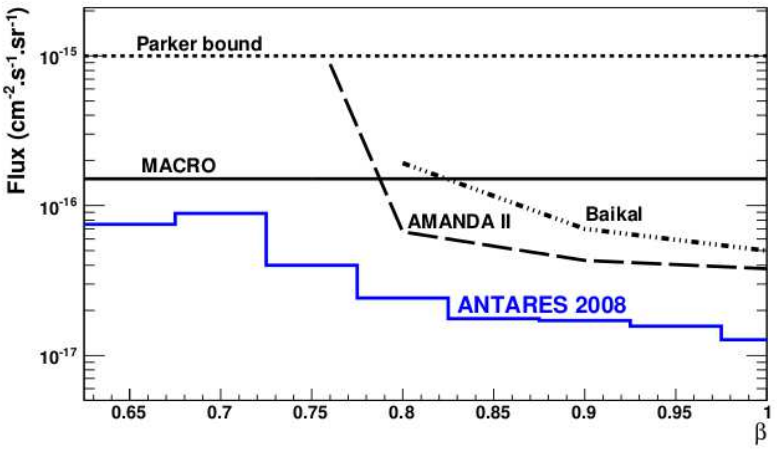

Figure 1.13: The ANTARES 90% C.L. upper limit on ustimapgoing magnetic monopoles, compared to the theoretical Parker bound, the published upper limit obtained by MACRO for an isotropic flux of monopoles as well as the upper limits from Baikal and AMANDA for upgoing monopoles [36].

A search for relativistic magnetic monopoles has been performed with 116 days of data taking for ANTARES detector, yielding a limits on the upgoing magnetic monopole flux above Cherenkov threshold which are more stringent than the ones obtained by previous experiments, as can be seen in Fig. 1.13 [36].

Chapter 2

Neutrino Detection Principle

2.1 Neutrino interactions

The main problem in neutrino detection is the very small cross section: the majority of neutrinos that reaches the Earth is able to traverse it without leaving any detectable trace. This makes a massive detector (∼GTon) mandatory. Since underground detectors cannot reach such mass, in the '60s Markov proposed to use a great amount of natural medium, such as the sea or lake water or the ice of Antarctica [51].

A neutrino telescope is usually made up by a matrix of light detector inside a transparent medium, such as water or ice. This approach has some advantages:

- a great target for neutrino interactions;
- a shield against background sources such as secondary particles in CRs;
- the Cherenkov photons produced after neutrino interactions are transmitted and not absorbed by the medium.

Also an acoustic or radio detection is possible for neutrinos in a huge volume of water [52].

2.1.1 Interaction types

There are two main interaction types depending on the boson exchanged. The interaction will be a charged current resulting in a final charged lepton if the exchanged boson in a $W^{\pm}$:

$$\nu_l + N \rightarrow l + X \tag{2.1}$$

When the exchanged boson is a Z^0, the interaction is a neutral current and the outgoing lepton is a neutrino:

$$\nu_l + N \rightarrow \nu_l + X \tag{2.2}$$

The cross section for CC interactions for neutrino at astronomic energies is given by:

$$\frac{d^2\sigma_{\nu N}}{dxdy} = \frac{2G_F^2 m_N E_\nu}{\pi} \frac{M_W^4}{(Q^2 + M_W^2)^2} [xq(x, Q^2) + x(1-y)^2 \bar{q}(x, Q^2)] \tag{2.3}$$

where Q^2 is the squared momentum transferred between the neutrino and the lepton, m_N is the nucleon mass, M_W is the mass of the mediator, G_F is the Fermi coupling constant and $q(x, Q^2)$ and $\bar{q}(x, Q^2)$ are the parton function distributions for quarks and antiquarks. x and y are the Feynman-Bjorken variables:

$$x = \frac{Q^2}{2m_N(E_\nu - E_l)} \tag{2.4}$$

$$y = \frac{(E_\nu - E_l)}{E_\nu} \tag{2.5}$$

In Fig. 2.1 neutrino cross section as a function of the energy is shown. Cross section grows linearly with energy in the range $10^{10} - 10^{15}$ eV, so it can be expressed as [2]:

$$\sigma_{\nu N} = (0.677 \pm 0.014) \times 10^{-38} \left(\frac{E_\nu}{1 \text{ GeV}} \right) \text{ cm}^2 \tag{2.6}$$

$$\sigma_{\bar{\nu} N} = (0.334 \pm 0.008) \times 10^{-38} \left(\frac{E_\nu}{1 \text{ GeV}} \right) \text{ cm}^2 \tag{2.7}$$

The increment to the cross section is reduced at higher energies because the invariant mass $Q^2 = 2m_N E_\nu xy$ could be larger than the W-boson rest mass. These values are extrapolated from the data of HERA collider, with a 10% uncertainty on the total cross section at $E_\nu \sim 100$ PeV [38]. In the range $10^{16} - 10^{21}$ eV cross section can be approximated as following:

$$\sigma_{\nu N} = 5.53 \times 10^{-36} \left(\frac{E_\nu}{1 \text{ GeV}} \right)^{0.363} \text{ cm}^2 \tag{2.8}$$

$$\sigma_{\bar{\nu} N} = 5.52 \times 10^{-36} \left(\frac{E_\nu}{1 \text{ GeV}} \right)^{0.363} \text{ cm}^2 \tag{2.9}$$

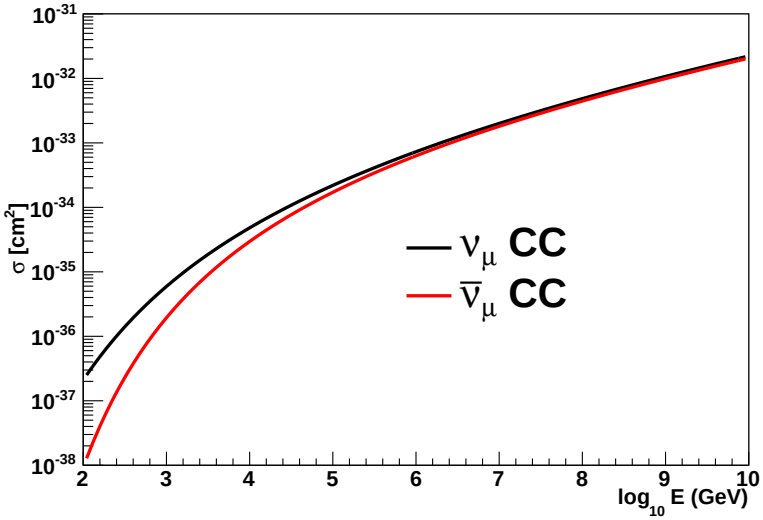

Figure 2.1: Cross-section for ν_μ and $\overline{\nu}_\mu$ as a function of the energy according to the parametrization in Eq. 2.10 [44]. At low energies the cross section for $\overline{\nu}_\mu$ is near one third of the ν_μ one. When the energy increases, the two cross sections converge.

One of the effects of the increasing cross section with energy is the enlargement of the effective volume of the detector. Also the muon range is increased with energy ($\sim$ 1 km at 300 GeV and $\sim$ 25 km at 1 PeV). A side effect is the Earth opacity for high energy neutrinos.

Simulations of neutrino interactions are implemented in the CERNlib package [41]. The kinematic of Deep Inelastic Scattering (DIS) is provided by LEPTO [45], with the following facilities:

- integration of the differential cross-section over a specified kinematic range to give the total cross-section (up to 10^8 GeV);
- sampling of the kinematic properties of the outgoing muon from the differential cross-section;
- hadronisation of the quark-gluon system in the target nucleus using the Lund string model, calling the PYTHIA 5.7/JETSET 7.4 package [46] to give the initial particles in the hadronic shower.

To perform these calculations, a particular PDF is used, either taken form the ones built in LEPTO or calling the Parton Distribution Function Library PDFlib 8.04 [42]. These functions come from the most up-to-date calculations of the PDFs based upon recent accelerator data.

	C_0	C_1	C_2	C_3	C_4
ν	-1.826	-17.31	-6.406	1.431	-17.91
$\overline{\nu}$	-1.033	-15.95	-7.247	1.569	-17.72

Table 2.1: Coefficients for parametrizing the cross section according to Eq. 2.10 [44].

LEPTO takes into account only the DIS contribution when computes the total cross section. This interaction involves a neutrino on a target nucleus, which participates with only one of its partons to produce a muon. Interactions between partons are important only in the hadronisation of the colored interaction products after the charged current exchange. LEPTO uses to integrate the differential cross-section over a range of kinematic variables. LEPTO is able to reproduce the cross-sections and kinematics computed by Gandhi et al. [43] to better than 5% in the main region of interest.

The LEPTO code is accurate up to lepton energies of 10 TeV. Above this energy a dedicated ANTARES software [66] performs an extrapolation of the model, for neutrino energy up to 10^8 GeV. For even higher energies a parametrization of the cross-section has been used [44], with an expression of the following form:

$$\log_{10}[\sigma(\varepsilon)/\mathrm{cm}^2] = C_1 + C_2 \cdot \ln(\varepsilon - C_0) + C_3 \cdot \ln^2(\varepsilon - C_0) + C_4 / \ln(\varepsilon - C_0) \quad (2.10)$$

where $\varepsilon = \log_{10}(E_\nu/\mathrm{GeV})$ and $4 < \varepsilon < 12$. Values of the constants for each νN and $\overline{\nu} N$ are shown in Tab. 2.1.1.

The choice of PDF enters into both the cross-section and kinematics calculations via the quark distribution functions $q(x, Q^2)$. These PDF are extracted from electron-proton collisions at HERA and other fixed target experiments. ANTARES software relies on the CTEQ6-D [47]. For high energy neutrino interactions, most neutrino interactions correspond to the low-x and high-Q^2 region of kinematic phase space, the one of greatest uncertainty in the calculations and fitting of the PDFs.

2.2 Neutrino Detection

Being a neutral particle, a neutrino can be detected by its interaction products. In the case of ANTARES experiment, the signal searched is the

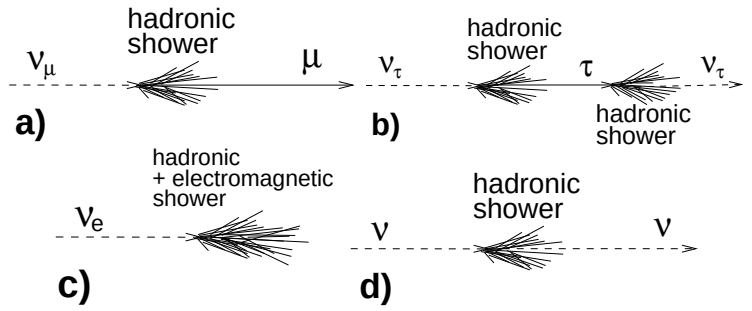

Figure 2.2: Some event signature topologies for different neutrino flavors and interactions: a) CC interaction of a ν_μ producing a μ and a hadronic shower; b) ν_τ CC interaction producing a τ and tracing the double bang event signature; c) ν_e CC interaction with an electromagnetic and an hadronic shower; d) NC interaction producing an hadronic shower.

Cherenkov radiations. To detect this radiation, a detector made up by transparent medium is mandatory. Schematic view of neutrino interactions are shown in Fig. 2.2

2.2.1 Cherenkov Radiation

When a neutrino interact via CC interaction, a charged relativistic lepton is produced and travels across the detector. When the speed of this charged particle exceeds the velocity of light in the medium through which it is traveling, the particle will emit the so called Cherenkov radiation [48]. In a medium the speed of light is defined as:

$$\beta c = v_l = \frac{c}{n} \tag{2.11}$$

where n is the refraction index of the medium and c the speed of light in the vacuum. When this condition is respected, the particle generates a shock wave (Fig. 2.3). The light emission creates a wave front where the light emitted is coherent. As the particle propagates across the medium, the wave front forms a cone with its axis along the particle trajectory. The opening half-angle of the cone can be written:

$$\cos\theta_c = \frac{1}{\beta n} \tag{2.12}$$

As measured in [50], refraction index at the ANTARES site is 1.35, generating a Cherenkov angle of 42.2^o. For a muon or an electron, the number of emitted

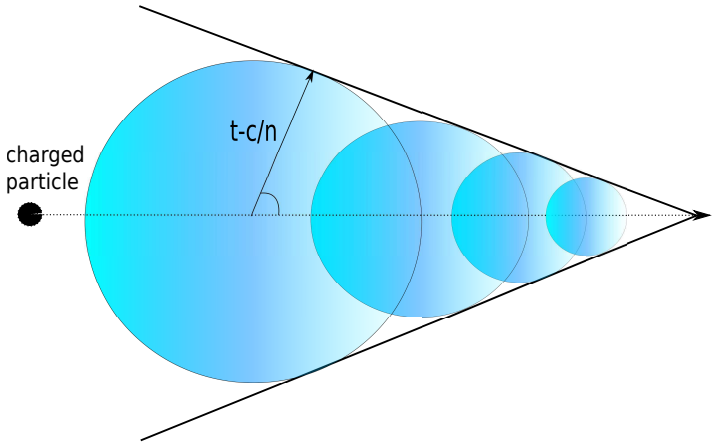

Figure 2.3: Cherenkov cone generated by a charged particle traveling through a medium with a speed superior than light in the same medium. The opening half angle depends on the particle velocity.

Cherenkov photons is given by:

$$\frac{d^2pN}{dxd\lambda} = 2\pi\alpha\frac{1}{\lambda}\left(1 - \frac{1}{\beta^2 n^2}\right) \tag{2.13}$$

where λ is the emission wavelength of the photon and α is a fine structure constant. Typically, in the wavelength range between 300-600 nm, 3.5×10^4 Cherenkov photons per meter are emitted.

2.2.2 Neutral currents interactions

If a NC interaction occurs, it is the same for all neutrinos flavors. The outgoing neutrino carries away a part of the energy and this increases the error on the true energy estimation. In reality, there is no topological difference between a neutral current interaction and an electron neutrino one, mostly because of the poorly instrumentation of the current detectors.

Hadronic and EM showers can be produced. The first ones present a more important fluctuation event-to-event due to the secondary particles produced during the interaction. These particles usually leave the shower producing long tracks.

Monte Carlo simulations show that a energy of TeV the largest amount of Cherenkov light is produced by EM sub-showers. Even if an hadronic shower can be parametrized in the same way of an EM one, the measurement of the incoming neutrino show an angular difference with the shower lesser than 2° for $E_\nu \geq 1$ TeV.

2.2.3 Electron neutrinos

A high energy electron is the product of a ν_e interaction for charged current. This electron can create a shower through bremsstrahlung and the following process of pair creation, generating a shower until the energy of constituents falls below the threshold value of critical energy E_c. At this point the remaining energy is dissipated via excitation and ionization.

An EM shower emits Cherenkov light isotropically in azimuth with respect to the shower axis. The lateral extension, of the order of 10 cm, is negligible if compared to the longitudinal one. The longitudinal profiles are used to parametrize the total shower length L as a function of the initial energy. The 95% of the shower energy is deposed covering this distance. For example, a 10 TeV electron can cover a length of 7.4 m.

The most difficult task in electron neutrino detection is the shower reconstruction. The pointing accuracy is lesser than the one for a single track. Also, there are two effects which have consequences on EM showers:

- the so-called Glashow resonance [39], which creates a resonance process affecting the $\overline{\nu}_e$:
$$\overline{\nu}_e + e^- \rightarrow W^- \rightarrow q + \overline{q} \tag{2.14}$$
The resonance peak is for a $\overline{\nu}_e$ with an energy of 6.3 PeV;

- the Landau-Pomeranchuk-Migdal (LPM) [40], which suppresses the radiative energy loss of the particles in the shower, enhancing the longitudinal development. This effect is dominant at ultra high energy ($E > 10^{16}$ eV).

2.2.4 Muon neutrinos

Muonic neutrinos are the most used probe in the field of high energy point sources search, for energies greater than 1 TeV. In this case, even if neutrino interaction occurs outside the detector, the muon produced is energetic enough to reach the sensible volume and even traverse the detector. The muon's direction is closely correlated with the neutrino's one, which allows a an accurate reconstruction of the primary direction after the measure of the muon track.

Neutrino telescopes rely on the relation between muon and neutrino direction. Being neutrinos neutral particles, they are not affected by galactic magnetic fields, so the direct pointing of the source is possible. While in traditional astronomy this is done tracing photons back to the sources, in a neutrinos telescope the muon direction (and thus the neutrino one) is tracked.

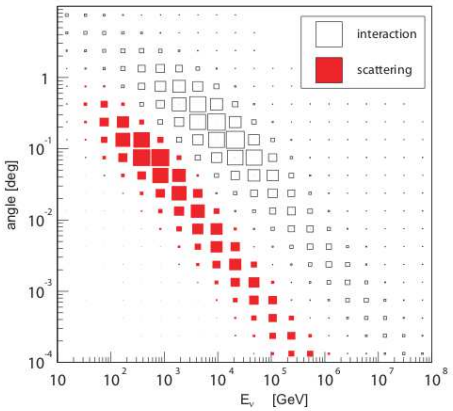

Figure 2.4: Angle between the neutrino direction and the produced muon (labeled as interaction), and the variation in direction of the muon due to multiple scattering.

There is however an angle between the incident neutrino and the outgoing muon, defined as [84]:

$$\theta_{\nu\mu} \leq \frac{0.6^\circ}{\sqrt{E_\nu[\mathrm{TeV}]}} \tag{2.15}$$

where E_ν is the energy in TeV. Although the muon is subjected to multiple scattering through matter, it will maintain the same direction to a large extent. Fig. 2.4 shows the difference in the direction of the muon with respect to the neutrino and the variation of the muon direction from the interaction vertex point to the moment in which it enters the detector.

As they propagate through matter, muons can lose energy by different processes (Fig. 2.5), which can be classified as following:

- ionization: muons traversing matter excite and ionize atoms all around. When the energy loss is at low energy (less than 1 TeV) ionization is the dominant process. In the rare case an electron is able to catch a non-negligible fraction of the muon energy, there is the emission of the so-called δ-rays.

- bremsstrahlung: charged particles emit radiation in the presence of an electromagnetic field, giving rise to a deceleration. If the muon propagate itself in a dense medium, the deceleration is produced by the electromagnetic interaction with nuclei and electrons of surrounding atoms.

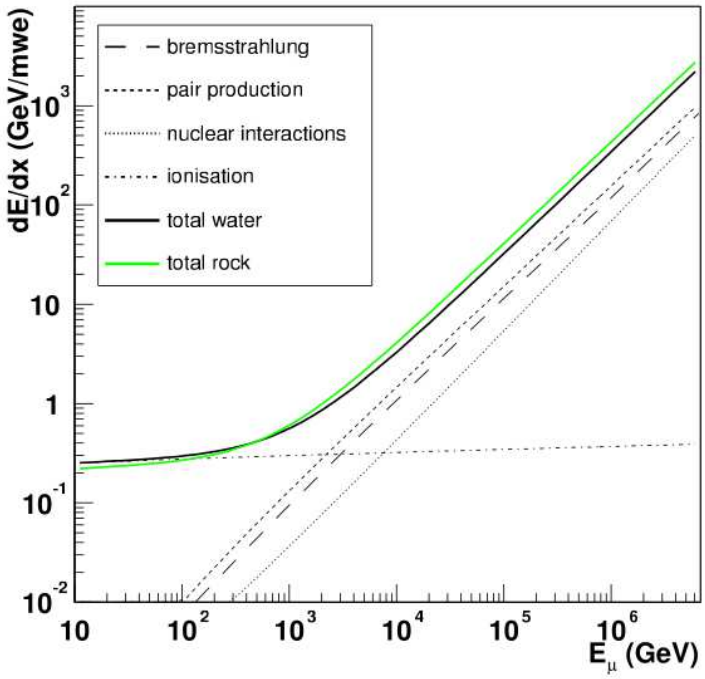

Figure 2.5: Average energy lost per meter of water equivalent (m.w.e.) for muons in sea water as a function of the muon energy. The contribution of the different processes are shown separately. The data for this figure were taken from the MUSIC code [81].

- pair production: this is the dominant process for muons with energy above 1 TeV, when an e^+e^- pair is produced.
- photo-nuclear interactions: there could be an exchange of a virtual photon between the muon and an atomic nucleus.

All the process listed above can be parametrized in a single formula for the muon's energy loss:

$$-\langle\frac{dE}{dx}\rangle = \alpha(E) + \beta(E) \cdot E \tag{2.16}$$

The first constant term takes into account ionization, while the second one, with a slope linear with energy, accounts for radiative losses. For water and a muon energy between 30 GeV and 35 TeV, the constant are $\alpha \simeq 2.67 \cdot 10^{-3}$ GeV/g and $\beta \simeq 3.40 \cdot 10^{-6}$ g^{-1} cm^{-2}. Ionization is considered as a continuous process, while the other process have a stochastic behavior, which makes more difficult the energy reconstruction.

2.2.5 Tau neutrino

When a ν_τ interacts via CC, the produced tau lepton can travel a distance dependent on its energy before decaying in a secondary shower. It is possible to detect the Cherenkov light emitted by the shower in the case both the ν_τ interaction and the tau decay occur in the sensible volume of the detector. Except for the case where the tau has a muonic decay, below 1 PeV for the largest part of ν_τ CC interactions it is impossible to resolve the tau track, so the event are classified as trackless ones.

Having a short lifetime, the tau lepton is able to travel from few meters up to few kilometers before decay, in the energy range of interest. If the leptonic track is long enough, it is possible to distinguish the primary interaction of the ν_τ and the tau decay. In this case a particular signature, called *double bang event*, is observed: a shower, plus a track, plus another shower.

If the tau track starts or ends outside the detector, only a shower plus a track can be detected. This signature is called *lollipop event*. This kind of event has a rate below than 1 event per year for small detectors like ANTARES. For larger detector, the optimal ν_τ energy to observe a double bang event is around $\sim 10^{16}$ eV, because the tau path length rapidly exceeds the dimensions of the detectors at higher energies. When the tau decays into a muon, the distinction form a true ν_μ event is not possible.

Chapter 3

The ANTARES Telescope

3.1 The ANTARES Detector

ANTARES (**A**stronomy with a **N**eutrino **T**elescope and **A**byss environmental **RES**earch) is actually the largest Cherenkov telescope in the Northern hemisphere. Its collaboration is made up by 200 physicists, engineers and sea science researchers from 7 different European countries. ANTARES' goal is the exploration of Southern sky hemisphere, an very interesting zone due to the presence of the Galactic Center.

The first project for ANTARES telescope was presented in 1996 [53], while the first line connection took place in March 2006 [54]. The whole detector deployment ended in May 2008, with the current 12 lines configuration.

The largest part of ANTARES technologies were already tested during the DUMAND experiment [55] and also the more successful Baikal detector in Siberia [56]. ANTARES has also some similarities with AMANDA/IceCube detector at the South Pole.

ANTARES is located at a depth of 2475 m in the Mediterranean Sea, 42 km away the coast of La Seyne-Sur-Mer, near Toulon in Southern France, at 42°48'N, 6°10'E. Fig. 3.1 show a schematic view of ANTARES detector. The current configuration is composed of 12 lines holding the detector for Cherenkov light emitted in water by the charged leptons coming from neutrinos' vertexes.

ANTARES could be seen as a complement of the South Pole detector because it explores a region which is not accessible to AMANDA or IceCube. Furthermore, being located on the seabed, ANTARES gives an opportunity to study the deep sea environment. Its permanent connection with the shore for high-bandwidth data acquisition allows the installation of sensor to study the sea parameters on very long periods. All the instrumentation for marine

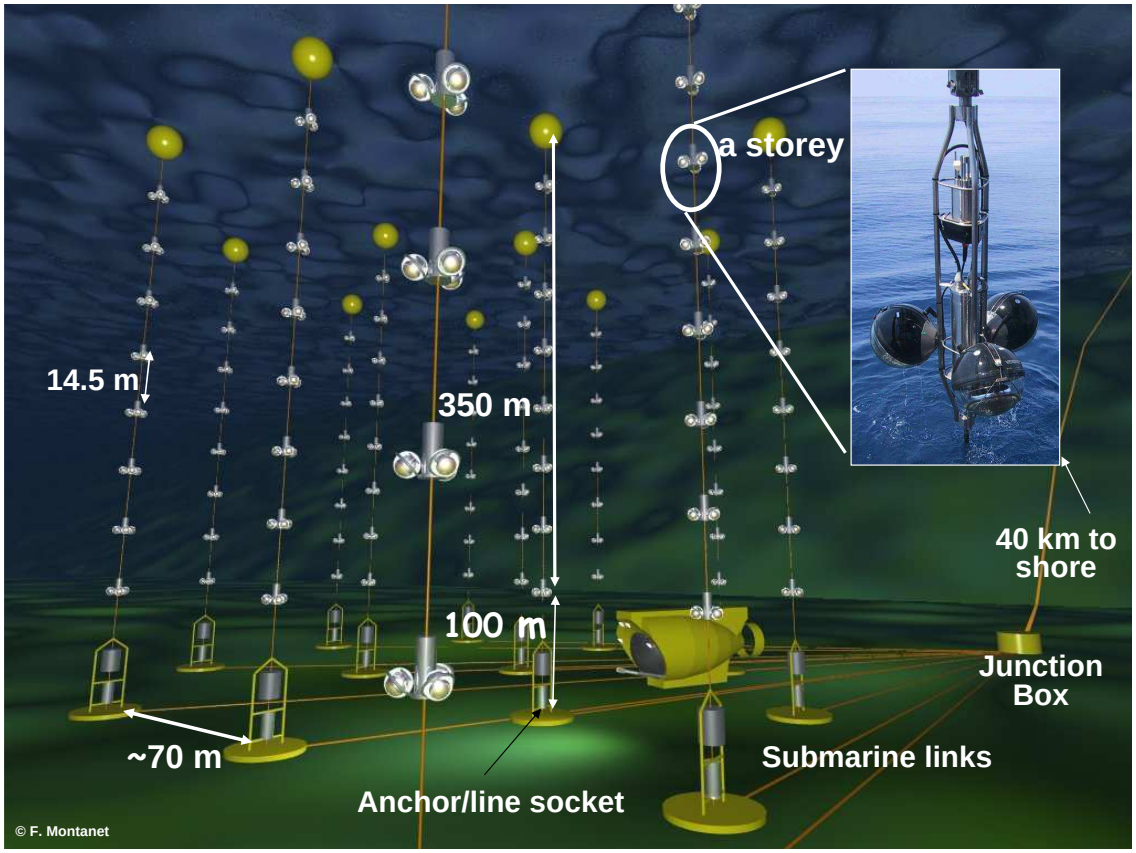

Figure 3.1: Schematic view of the ANTARES detector.

and Earth science is distributed on the 12 detector lines, plus a 13th one dedicated to the monitoring of sea environment.

3.1.1 Detector Layout

ANTARES was designed to have an area of 0.1 km^2. Its fundamental unit is called Optical Module (OM) and its scheme is shown in Fig. 3.2 [57]. It consists of a borosilicate glass sphere (with 41.7 cm of inner diameter and 15 mm thickness, in order to support high pressures) housing a photomultiplier tube (PMT, 10" Hamamatsu R7081-20). This model has the following properties:

- a hemispherical 10 inch diameter, which assures the best angular acceptance. It is a good compromise between a large angular coverage and a still small contribution in the transit time spread due to optical entrance;
- a gain greater than $5{\cdot}10^7$ when working at a voltage up to 2000 V;
- a peak-to-valley ratio greater than 2, in order to have a good separation of the peak of 1 photo-electron;
- a transit time spread (TTS) smaller than 3 ns. This impacts track resolution and the angular resolution for the detector;
- a dark noise rate smaller than 10 kHz for the 0.25 photo-electron threshold.

The influence of Earth's magnetic field can spread the trajectories of the low energy photoelectrons in the optical entrance, and thus degrade the TTS. To avoid this effect, a μ-metal cage with high magnetic permeability is included in the OM as magnetic shield. The PMT, along with the magnetic shield, is fixed to the glass sphere by a silicon gel able to perform a good optical coupling, reducing photon internal reflection. The opposite of the glass hemisphere is painted black to minimize the reflection and insuring a little efficacy for downgoing atmospheric muons.

The PMTs are gathered in triplets, forming a three dimensional telescope matrix element called storey. The three OMs are mounted in a mechanical structure, the Optical Module Frame (OMF), equipped also with a titanium container, the Local Control Module (LCM), containing the offshore electronic, two Analogue Ring Samplers (ARS) per OM. The dialog between the OMs and the offshore data control is assured by this Application-Specific

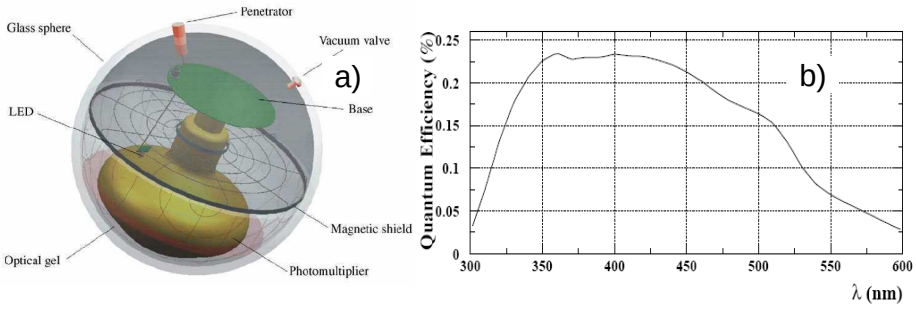

Figure 3.2: Schematic view of the OM of ANTARES on the left, the plot of its quantum efficiency on the right.

Integrated Circuit (ASIC). The ARS receives all the electronic commands: the clock signal, the slow control, the HV supply and the readout.

The storeys are grouped in five as a sector, a stand-alone unit for power distribution and data acquisition. One out of five storeys has a Master Local Control Module (MLCM) with an ethernet switch, a bidirectional concentrator and a Dense Wavelenght Division Multiplexing board (DWDM) which multiplexes the signal information from each sector onto one optical fiber. The MLCM contains all the electronic boards for all the functionalities at the sector level. Some storeys are equipped with receiving Rx hydrophones (5 per line) for the acoustic positioning system and a LED optical beacon (4 per line) for timing calibration.

Each detector line, 450 m long, is a chain of 25 OMFs connected by Electro-Mechanical Cable segments (EMC), each one 12.5 m long from storey to storey. Lines are arranged on the sea bed in an octagonal configuration 3.3, in order to minimize potential symmetries which could contribute to ambiguities in the reconstruction. There is a 60-75 m spacing between the lines, making the detector sensitive to muon energies greater than 100 GeV. The lines are anchored on the sea bed with a Bottom String Socket (BSS), while on the top of each line there is a buoy to maintain the verticality. The BSS is equipped with a String Power Module (SPM) in order to power supply all the instruments. There is also a String Control Module (SCM) which contains the electronics required by the slow control system, the clock and the instruments of the BSS and controls of the data traffic from the MLCMs.

On the seabed there is an infrastructure which connect ANTARES to the shore: it consists of a Junction Box (JB), the Main Electro-Optical Cable (MEOC) and the Inter Link cables (IL). The internal elements of the JB are protected from water pressure and corrosion by a titanium structure. On

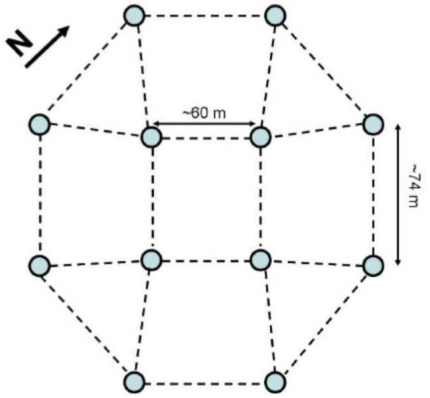

Figure 3.3: Schematic view of ANTARES detector, where each dot represents a line. The octagonal minimizes potential symmetries between the different detector parts, and thus minimizes the ambiguities at reconstruction stage.

the JB there are 16 connectors for the 12 lines, the instrumentation line and the spares. The MEOC contains an internal steel tube and 48 optical fibers, protected and insulated by a set of external layers of copper and steel, in order to avoid possible failure and breaking.

Data are sent from the detector to the control room, near Toulon, where they are stored in the PC farm. The operation of data filtering, triggering and communication with the database are performed before data are stored permanently at the Computer Center in Lyon.

The 13th line, the so-called IL07, is dedicated to the measurement of environmental parameters and equipped with oceanographic sensors. Along with the twelfth line, it also include storeys equipped only with hydrophones to study the ambient acoustic background.

3.1.2 Positioning and absolute time measurement

ANTARES lines are anchored on the seabed and sustained by a top buoy, along with other buoyancy for individual OMs. Lines are not fixed and even a small sea current ($\sim$5 cm/s) can displace the top storeys of several meters. For this reason, for each line a real time positioning system had been implemented. This is the sum of two independent systems: an acoustic positioning and a lattice of tiltmeters-compasses sensors. The information from both systems are combined in order to perform a global χ^2 and to reconstruct the line's shape. In a second time it is possible to compute the relative position of each OM, starting from line fit and using the known geometry of each individual storey.

For the measurement of the absolute time, a master clock system is implemented. This system delivers a common reference time to all the offshore electronics in the LCMs. A time stamp based on GPS time is sent via a fibre optic network from the shore to the junction box, where it is sent to all the lines. The clock has a frequency of 20 MHz and is able to to calibrate itself. Also, it measures the time path from shore to the LCM, using the echoes between the LCM and the shore station.

3.2 Environmental properties

Because of the nature of the ANTARES telescope, an extensive study of the detector site had been carried out, in order to evaluate environmental parameters and site properties.

3.2.1 Water optical properties

Detector's medium can affect Cherenkov light propagation by scattering or absorption, effects which can spoil the capabilities of the telescope. Absorption reduce the number of photons that reach the PMTs affecting the amplitude of the Cherenkov wavefront, while scattering change the direction of propagation and the arrival time distribution. In this case two different cases of photons are defined: direct photons, not affected by scattering, and indirect photons otherwise.

For a given wavelength λ, propagation of light in a transparent medium is defined by the latter's optical properties, such as the absorption $a(\lambda)$, the scattering $b(\lambda)$ and the attenuation coefficient $c(\lambda) = a(\lambda)+b(\lambda)$. Otherwise, these coefficients can be defined as lengths: $L_a(\lambda) = a(\lambda)^{-1}$, $L_b(\lambda) = b(\lambda)^{-1}$ and $L_c(\lambda) = c(\lambda)^{-1}$. Each one of these lengths represent the path after which a beam of intensity I_0 is reduced by a factor 1/e, according to the following relation:

$$I_i(x,\, \lambda) = I_0(\lambda)e^{-x/L_i(\lambda)} \quad i = a,\, b,\, c \tag{3.1}$$

where x is the distance covered by light.

The absorption length in ANTARES site was measured by a LED source at different distances from the OM. The value measured for a wavelength $\lambda = 466$ nm is [58]:

$$L_c(\lambda = 460 \text{ nm}) = 41 \pm 1_{\text{stat.}} \pm_{\text{syst.}} \text{ m} \tag{3.2}$$

The scattering length was measured with a different experimental setup (Fig. 3.4).

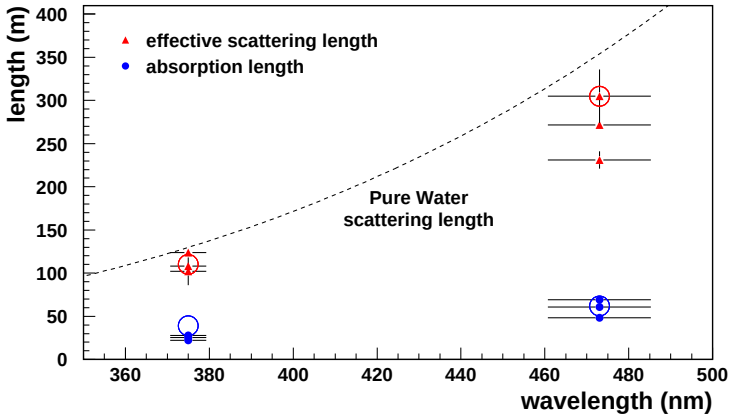

Figure 3.4: Absorption (dots) and effective scattering (triangles) lengths measured at the ANTARES site at various epochs for UV and blue data. Horizontal error bars illustrate the source spectral resolution ($\pm 1\sigma$). The large circles are estimates of the absorption and scattering lengths in pure sea water. The dashed curve is the scattering length for pure water, upper limit on the effective scattering length in sea water.

3.2.2 Biofouling and sedimentation

ANTARES is sited in a very particular environment and it is exposed to the so-called biofouling, i.e. particle sedimentation and adherence of bacteria. This effects affect light transmission through the glass sphere of the OMs [60].

For this measure an experimental setup made up by two resistant glass spheres, like the ones used to house the OMs. The first one was equipped with five photo-detectors glued at the surface with different inclinations respect the zenith angle θ. In the second sphere two blue light LEDs were housed. Several months of immersion were necessary to extrapolate data on long periods. Fig. 3.5 shows the light transmission as function of the immersion time for the five photodiodes. As expected, fouling tends to decrease when the zenith angle on the glass sphere increases. The process seems to reach a saturation after 8 month of operation and the loss of transparency in the equatorial region of the OM dropped of $\simeq$ 2.7%. For ANTARES configuration with PMTs pointing 45° downward, biofulding and sedimentation are not a major problem for the experiment.

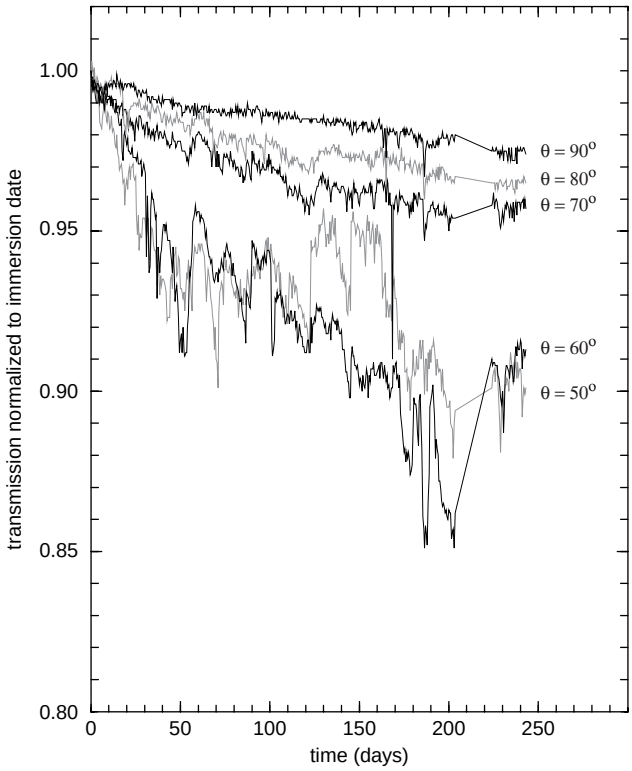

Figure 3.5: Light transmission as a function of time from the second immersion, with the two spheres mounted horizontally. The measurements for each of the 5 photodiodes are normalized to unity at immersion day. Curves are labeled according to the photodiode zenith angle θ [60].

3.2.3 Optical background in sea water

There are two main contribution to optical background in ANTARES: the decay of radioactive elements in water and the so-called bioluminescence, light produced by organisms.

The ^{40}K is the most present of all the radioactive natural isotopes. Its decay channels are:

$$\begin{array}{rcl} {}^{40}\mathrm{K} & \rightarrow & {}^{40}\mathrm{Ca} + e^- + \overline{\nu}_e \text{ (BR=80.3\%)} \\ {}^{40}\mathrm{K} + e^- & \rightarrow & {}^{40}\mathrm{Ar} + \nu_e + \gamma \text{ (BR=10.7\%)} \end{array} \tag{3.3}$$

Both the channel produce a noise detectable in ANTARES. The first decay channel produces electrons with an energy spectrum up to 1.3 MeV, producing 5 Cherenkov photons per electron on average in the wavelenght sensitivity window of the PMT. This gives rise to a photon flux of about 100 cm^{-2}s^{-1}

for a 50 m water attenuation lenght. The photon originating from the second chain has an energy of 1.46 MeV, sufficient to produce electrons able to give rise Cherenkov effect.

Light's intensity from Cherenkov emission is strictly bound to the ^{40}K concentration in water. This is not a feature of the site, since salinity in Mediterranean Sea has small geographical variations. Knowing that ^{40}K emission is stable, it can be used to measure the PMT detection efficiency.

Bioluminescence is diffused in all the oceans and is due to two main sources: a steady glow from bacteria and flashes produced by marine animals. Flashes are detected as burst while the animal is near the detector, while the bacterial glow has a quite constant rate, as seen in Fig. 3.6. Along with the ^{40}K decay, the bacteria colonies give rise to a typical baseline rate of 20-30 kHz. Measurement over 4 year have shown that the mean rate value is around 60 kHz.

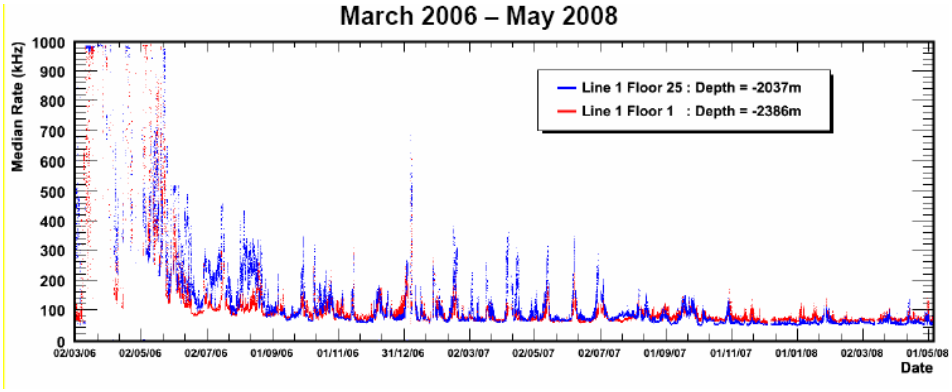

Figure 3.6: Mean rates (in kHz) measured by ANTARES' PMTs in the period from March 2006 to May 2008. The constant background rate is due to ^{40}K radioactivity and bacterial glow, while the bursts correspond to the passage of bioluminescent animal near the detector.

The second component of the bioluminescence is composed by short burst, due to the passage near the detector of light emitting organisms, which can last from hundreds of microseconds to seconds. These bursts are simultaneously detected by nearby optical modules and they are superimposed on the constant baseline rate, a 20% over it.

In order to avoid the aging of PMTs when high optical background rates are recorded, when a safety threshold is reached, the PMTs are tuned to low gain mode, until the stable rate is recovered. In the meantime, the rates are monitored by the instrumentation line (IL). The bursts rate can reach

values of some MHz, and an appreciable dead time can be produced in the acquisition system.

In order to find correlations with the biological activity, deep sea currents were monitored on long time periods. Even if long-term variations had been registered, the baseline component is not correlated nor with current nor with burst frequency. This may suggest that contributions are caused by different populations.

3.2.4 Deep sea currents

Sea currents have to be taken into account in the mechanical design of the detector. At the ANTARES site, the detector lines sway in the sea current which is typically 5 cm/s, with variations up to a maximum value of 30 cm/s.

3.3 Data Acquisition System

All the data from the ANTARES site are sent to the shore, where a data processing remove all the background. This data are signals with an amplitude larger than 0.3 photo electrons (p.e.), digitalized at LCM level [61]. All smaller signal are supposed due to dark currents inside the PMT and thus eliminated. To reject the contribution due to electronic noise, a timing gate is tuned to integrate PMT signals in a window of 35 ns.

PMTs produce an analogue signal which is read by two integrated circuits, the Analogue Ring Sampler (ARS), in charge of digitising the signal when triggered. The signal is then sent to the Data Acquisition (DAQ) board, in charge to envoy data to shore. The DAQ system is a network of hundreds of processors (Fig. 3.7). These offshore processors are integrated in custom made electronic. The MEOC links the DAQ system to the on-shore processors of the shore station.

To reconstruct the arrival moment of the photon it is mandatory to know the time offset between the local clock board and the PMT cathodes. This process is called time calibration. After that, the optical signal reaches the junction box and is converted in a data stream, readable by the front-end chips. For every signal above threshold (0.3 p.e., the so called L0 threshold) recorded by the PMT, the ARS counts the number of Time Stamp (TS) since the last reset of the master clock. A time stamp id the period of the master clock pulse, than permits to achieve a precision of 50 ns for the photon reaching the PMT. Clock pulses are the interpolated by a Time to Voltage Converter (TVC). The latter returns an analogue signal proportional to the

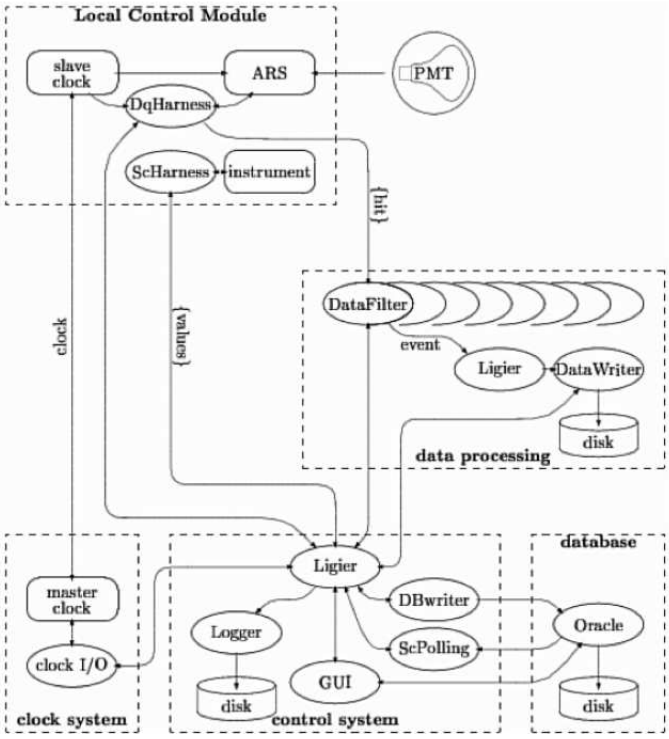

Figure 3.7: Schematic view of the DAQ hardware. Each storey has its LCM. The information is sent by sectors to the SCM of each line and then to the shore station via the JB.

moment in which the PMT signal took place within the TS. The TVC has a resolution of 8 bits, corresponding to 50 ns $\times 256^{-1} \simeq 0.2$ ns.

A time calibration is needed to reconstruct precisely the arrival time moment of the photon and to know the time offset introduced by the different optical paths.

The data writing in a temporary memory (pipeline) induces a dead time of 250 ns on the ARS. The dead time is reduced using both the ARS of each module, because the two samplers are alternated. ARSs are also able to work in waveform mode, sampling and digitizing the photomultiplier signal. This procedure is used only during certain calibration runs. The ARS integrates the charge from the start where the signal passes the threshold for a period of 40 ns.

Data coming out from the ARS contains arrival time and charge information. These quantities can be combined to form hits, procedure in charge of the Filed Programmable Gate Array (FPGA), that organize the hits in

frames covering a time period of 104.858 ms. Each frame is sent to the shore as a separate package. This transmission is performed by the DaqHarness, a program running in the CPU of LCMs. Control, monitoring and calibration are performed by the ScHarness, on the same CPU.

PMT signals are selected only on the base of the 0.3 pe threshold. However not all the raw data can stored because the storage space limitation, so a background suppression is necessary. For this operation a DataFilter program had been implemented on shore. This program perform a fast algorithm in real time suppressing background and keeping only muon track-like information. After the filtering, a DataWriter program store the data on the disk.

3.4 Calibration

In order to reconstruct the track of the incoming particle, it is necessary to know precisely the time and position. A calibration procedure allows to have the information as precise as possible

3.4.1 Position Calibration

As previously said, ANTARES is subject to the sea current and to monitor it continuously a system of acoustic positioning had been developed. On the BSS of each line, an acoustic transmitter send a pulse (range 40-60 kHz) which is received by all the hydrophones along the line. In order to monitor the depth, the BSS is also equipped with pressure sensors.

The instruments of the LCM (a bi-axial tilt meter and a compass) allow to measure the pitch, the roll and the heading. Combining their information, it is possible to know the OM position with a precision of 10-20 cm.

In Fig. 3.8 the results of the analysis of the signals received by the hydrophones on one ANTARES detection line is shown, along with the horizontal displacement form the nominal position.

3.4.2 Time Calibration

There are different factors which can affect the time resolution: time spread of the PMT, the scattering and chromatic dispersion of Cherenkov light in the environment. Delay from electronics is less relevant, being no more than 0.5 ns. With time calibration, it is possible to achieve a precision better than one nanosecond.

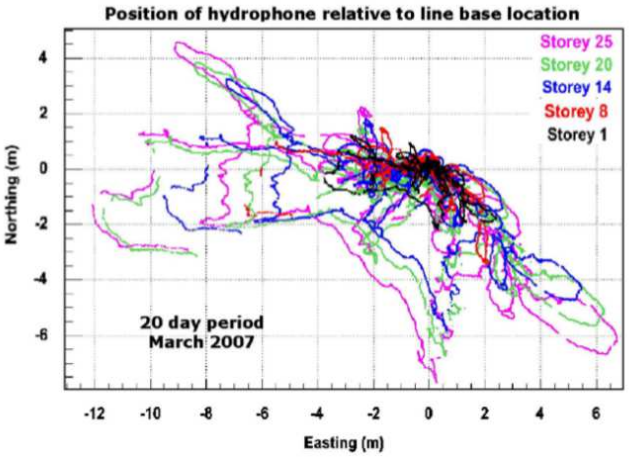

Figure 3.8: Horizontal tracking of the hydrophone of one particular line over a period of 20 days. The hydrophones are located at 100, 202, 289, 376 and 448 m from the sea floor. The measurement precision is $\sim$ 10 m.

The main uncertainties contributing to the relative time resolution come from the TTS of the signal in the PMT, around $\sim$ 1.3 ns. The calibration results show that the uncertainty of the transit time is around 0.5 ns. Taking into account the optical properties of the sea water, such as light scattering and chromatic dispersion, the uncertainty results 1.5 ns for a distance of 40 m. The contribution of the electronics would spread the timing accuracy, which contributes with less than 0.5 ns to the overall relative time resolution.

3.4.2.1 LEDs inside the optical module

Each OM is equipped with a blue LED glued to the back of PMT. This LED can illuminate the photocatode in the wavelength band where ANTARES is most sensitive (470 nm). This system measures the transit time of the PMT and dedicated runs for this calibration took place once a month.

3.4.2.2 Optical Beacon

This is a time calibration between different OMs. It also allows to measure the effects of water on light propagation.

An Optical Beacon can be a LED Beacon or a Laser Beacon. The first is made up by 36 LEDs arranged on the surface of hexagonal cylinders and pulsed by dedicated electronic circuits. LED Beacons are located uniformly

along the line, in order to illuminate all the storeys on the neighboring strings. The trigger for LED Beacon to fire is provided by a 1.5 V negative square pulse with a duration of around 150 ns superimposed on a negative direct current (DC) bias that can be varied from 0 to 24 V. Varying the DC voltage ti is possible to tune the amount of light emitted. The detector is not sensible when light is emitted below 8 V. When the DC is at 24 V, there is an emission of approximately $4 \cdot 10^8$ photons [**?**].

Laser Beacon uses a solid state pulsed laser whose light is spread out by a diffuser. They are located at the BSS of lines 7 and 8 and illuminate the lower part of the detector. Optical Beacon system has a precision of 0.3 ns, in agreement with the expected value spoiled by the electronics [63].

3.5 Data Processing and Triggering

ANTARES data taking is organized in runs, each one almost three hours long. A software called RunControl stores in the database run duration, starting time, ending time and trigger condition. During a run, the data frames from the LCMs are sent to a on-shore PC. When the time period change, the following frames are sent to a different PC. A set of frames during a period of 13 ms is called TimeSlice.

A first-level filtering can reduce the optical background, relying on the Cherenkov light emitted by a single muon track. The PMTs keep all the signal above 0.3 pe and data from the full detector are transferred to the computer at the processing farm within a time window of about 100 ms. This correspond to a data flow of 0.5 GB per second from the detector to the shore. The largest part of these data are composed by optical background and after the filtering the amount of data is reduced by a factor 10^4. The software in charge of filtering, the DataFilter, is referred to as trigger [65].

The first assumption is based upon coincidences: it is far less probable that hits caused by background appear in the same storey. The first level selection relies of hits coincidence within 20 ns in different PMTs of the same storey. Hits are however selected if they have a charge greater than 3 pe: these are the so-called L1 hits. After this selection, time and charge information are merged and the DataFilter looks for hits correlated by causal relation. Two hits in different parts of the detector are causally related if their timing and positioning satisfy the following condition that parametrize a light wave propagating from one PMT to another:

$$|\Delta t| \leq \frac{n_g}{c} d \tag{3.4}$$

where Δt is the time difference between two hits, d is the difference two hits

storeys and $v_g = n_g/c$ is the group velocity of light in sea water. To take account of all the uncertainties, trigger selection add 20 ns to the selection.

A set of L1 hits is called cluster and considered as a candidate event. Cluster are stored if they have a sufficient size ($N_{L1} \geq 5$). These data contain the triggered hits plus all the hits which happen between 2 μs before the first level hit and 2 μs after the last one. This last collection is called Snapshot, while all the hits are saved in a data structure referred as PhysicsEvent. Moreover, for each timeslice a SummaryTimeSlice is generated, containing the number of L0 hits recorded by the PMTs.

A second level trigger looks for coincidences with consistent with the Cherenkov angle emission. The solid angle is divided uniformly with a spacing of 10° and a search of hits which could form a track similar to that expected for Cherenkov photons is performed.

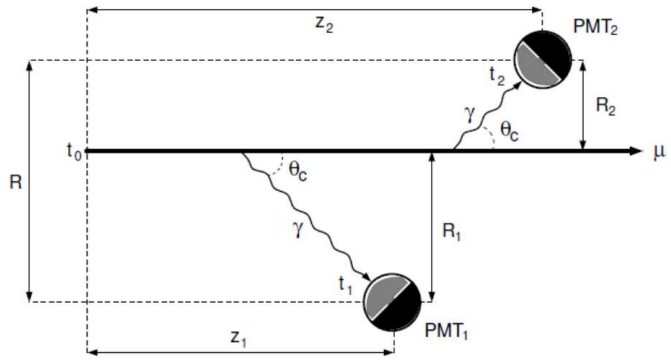

Figure 3.9: Schematic view of the track passing in the detector. The photons (γ) are emitted at the Cherenkov angle θ_c and reach the PMT$_i$ at time t_i. The PMT position is defined in this reference system as the distance between the PMT and the muon position at the time $t_0(z_i)$, while R_i is the distance of closest approach.

The reference frame chosen has the axis of the detector parallel to the suspected muon track. In this geometry, the expected time for a hit is:

$$t_i = t_0 + \frac{1}{c}\left(z_i - \frac{R_i}{\tan\theta_c}\right) + \frac{n_g}{c}\frac{R_i}{\sin\theta_c} \tag{3.5}$$

where t_0 is the initial time of the muon track, the second term represent the time that the muon takes to travel from the initial position to the point where the detected photons are emitted, and the last term is the time required for

the photons to reach the PMT. Assuming $\cos\theta_c = 1/n_g$, the time difference between two hits caused by Cherenkov radiation can be written as:

$$t_2 - t_1 \leq \frac{z_2 - z_1}{c} + \frac{R}{c}\tan\theta_c \tag{3.6}$$

where R is defined as the maximum distance between two PMTs perpendicular to the muon track. A pair of hits is considered a Cherenkov hits pair if it satisfies the following relation:

$$|t_2 - t_1| \leq \frac{z_2 - z_1}{c} + \frac{R}{c}\tan\theta_c + 20 \text{ ns} \tag{3.7}$$

For all the hits which obey the previous relation new clusters are formed. A more restrictive selection can be made selecting a certain size for clusters.

To summarize the basic three level triggers are:

- L0: the electrical signal has an amplitude greater than 0.3 p.e.;
- L1: the two possible kind of L1 hits:
  - an electrical signal with amplitude greater than 3 p.e.;
  - two L0 hits in time coincidence (time window smaller than 20 ns, to take into account the position of the PMTs and the scattering effects) on the same storey;
- T3: a cluster of L1 hits of two kinds:
  - coincidence of two L1 in a 80 ns time window;
  - coincidence of two L1 in a 160 ns time window.

There are then six trigger algorithms which could be applied at a higher level:

- 3N: it requires at least 5 L1 in a time window corresponding to a muon track;
- T3 (2T3): it requires at least 1 or 2 T3;
- GC: the Galactic Center trigger requires 1 L1 and 4 L0 in the direction of the galactic center. It is used to maximize the detection efficiency of neutrinos coming from galactic center;
- Minimum bias: each second, in a time window of 4 μs, the data is registered without any filter (it is a monitor for data quality);

- K40: used for in situ calibration, it requires 2 L0 on 2 optical modules of the same storey within a time window of 50 ns;
- TST: the Transient Source Trigger is activated in presence of an alert from γ ray satellites. In this case, 2 minutes of data around the trigger are saved without any filtering.

The main contribution to the trigger data stream is given by atmospheric muons crossing the detector. Their rate depends on the particular choice of the trigger logic, but it is the range 2-10 Hz. At trigger level there is no distinction between events due to atmospheric muons, atmospheric neutrinos or cosmic neutrinos.

3.6 High threshold measurement

The so called high threshold is a parameter used in the first level trigger for the selection of hits with large amplitude. Large hits are interesting because they are likely to be produced by physics signal. Higher values for the thresholds allow to reduce the background which is not able to produce such large amplitudes. In order to optimized the data taking, there is a compromise between the high threshold set and the L1 trigger rate. During the ANTARES data taking there are three main values used as high threshold: 3 p.e., usually for the scan runs, 5 p.e. and 10 p.e., used for test runs [59].

The high threshold value is measured in the charge distribution for triggered hits. As shown in Fig. 3.10, the charge distribution has two peaks. The first one, seen at 1 p.e., is due to the pure SPE signals, which are smeared by the resolution of PMT and ARS, while the second peak is the high threshold. The part below the high threshold is dominated by the SPEs which pass the trigger as a pair. The distribution above the cut is due to large hits that originate from the tails of SPE distribution.

To identify the high threshold, a custom SeaTray module able to identify the second peak had been written and tested on the November 2010 data sample. When no secondary peak is found, the threshold is set at 10 p.e. The module has been used to measure the high threshold value for all the runs from January 2007 until December 2011.

The thresholds of all the runs had been measured, taking into account all the triggered hits in the runs. When the high threshold value was different from the database one, also the charge distribution on different lines has been inspected. A crosscheck with the run table has been performed in these cases, in order to understand the reason of the difference between the measure and the database value.

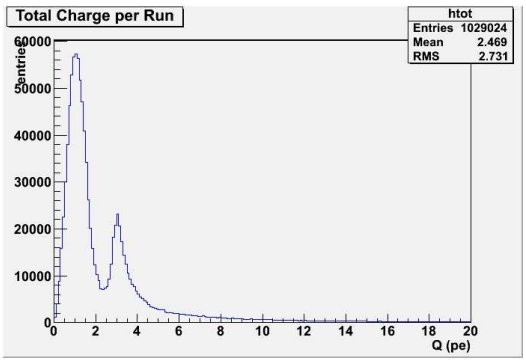

Figure 3.10: Typical charge distribution for a normal ANTARES run, without imposing any particular condition for the trigger choice.

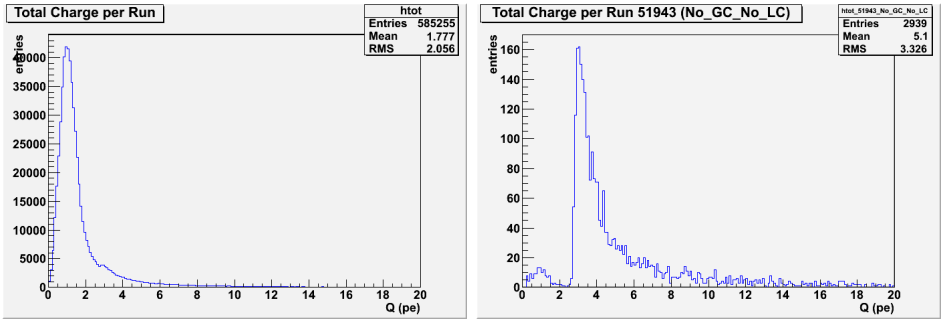

Figure 3.11: Left: charge distribution for run 51943 (September 2010), with misidentified threshold. Right: same distribution for the same run but without LC and GC hits, when the peak at 3 p.e. becomes visible.

There is a recurring problem of misidentified threshold when taking into account the hits due to all the triggers. The main problem looks like the 3 p.e. peak is overwhelmed by the local coincidence hits which are needed to fire trigger such as GC or TQ, as shown in Fig. 3.11. A second analysis has been performed removing all the LC and GC hits, in order to understand if the high threshold is really overwhelmed or if the runs are pathological. All the still remaining disagreements have been investigated and noted for further analysis [62].

3.7 Background rate

To estimate the rate from the optical background, it is necessary to separate the two components. In the 400 part per million (ppm) of potassium present in the sea water, the 0.0117% is ^{40}K. Simulation of this kind of back-

ground show a continuous behavior, with a rate of 30 ± 7 kHz per PMT [64]. For the bioluminescence the rate of light emitted changes in time. It is possible to define a baseline rate, taking into account the ^{40}K contribution and burst of bioluminescence from 50 kHz to several hundred kHz. A burst of bioluminescence at the top of this baseline rate can last several millisecond or minutes.

A completely different sort of background comes from cosmic rays. The largest part of muons crossing the detector are atmospheric muons produced in cosmic rays interaction with the atmosphere. There is a shielding effect because of the huge layer of water above ANTARES, but very energetic muons are however able to reach the detector. There are a few muons per second which are able to reach the detector. However, ANTARES PMTs are pointing downwards, in order to have a better sensibility to upgoing muons than to the downgoing ones. Being impossible for a muon to cross the Earth, upgoing muons can be generated only by neutrino interactions. If these neutrinos are produced by cosmic rays in atmosphere, they are called atmospheric neutrinos and mix with the cosmic signal. Rejection of this background is based on statistical tools. Atmospheric neutrino reaching the detector are around five or six per day. Their flux is visible in Fig. 3.12 as a function of the zenith angle[1]. A cut on the incoming direction can distinguish atmospheric muons, but there will be always a upward rate due to atmospheric neutrinos.

3.8 Detector performances

3.8.1 Visible sky

Neutrino telescopes are optimized to observe the upgoing signal from neutrinos which have crossed the Earth. This is the main criterion to distinguish between cosmic signal and atmospheric background. The fraction of visible sky is therefore on the other side of the Earth. ANTARES position at the coordinates 42°50' N, 6°10' E allows the telescope to cover a solid angle of 3.5π sr during the day rotation.

3.8.2 Effective Area

The effective area is the surface, perpendicular to the incident particle beam, of a perfect detector (100% of efficiency) to detect the same event number produced in the real data taking. It can be considered an expression

[1] Angle with which the muon cross the detector with respect to the vertical

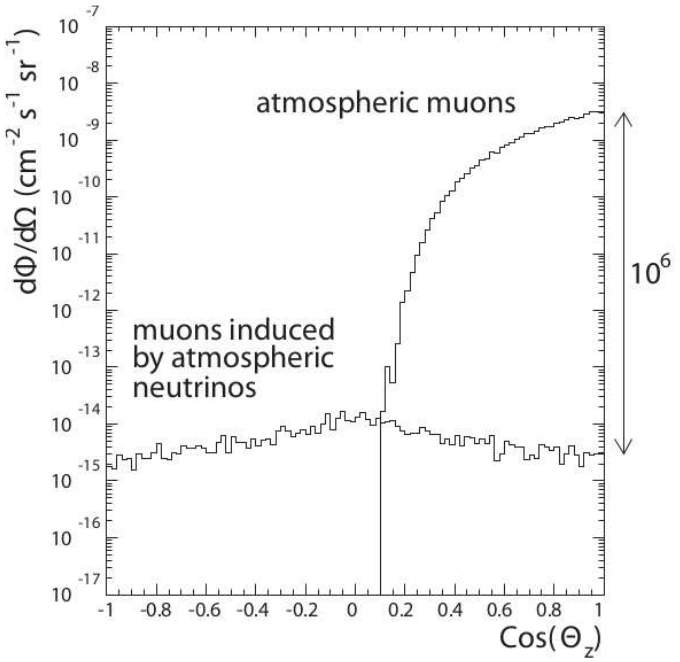

Figure 3.12: Muon flux at a depth of 2.1 km as a function of the zenith angle. A $\cos\theta > 0$ indicates downward-going particles.

the evolution of the detection efficiency It can be calculated as a function of the energy anf the direction. For neutrinos, the effective area is smaller than the muon one beacuse of the smaller cross-section. The effective area for neutrinos is energy-dependent, just like the cross section, thus it becomes greater than 1 m^2 for energies above 100 TeV. In this range there is a good probability for neutrinos crossing Earth at a nadir angle of 0° to interact during their long travel through the planet. This shows an opacity effect depending on the angle and it is the reason why neutrinos of the highest energies are expected for angles close to the horizon.

The effective are can be computed as following:

$$A^{\nu}_{\text{eff}} = \frac{N_{\text{sel}}}{N_{\text{gen}}} \times V_{\text{gen}} \times (\rho N_A) \times \sigma(E_\nu) \times e^{-N_A \sigma(E_\nu) \int \rho dl} \tag{3.8}$$

where:

- N_{sel} is the number of the selected events at the cuts' choice;
- N_{gen} is the number of generated events;

- V_{gen} is the generation volume;
- ρN_A is the nucleon density of the target;
- $\sigma(E_\nu)$ is the neutrino cross section;
- $\int \rho dl$ is the integrated density on the neutrino trajectory across the matter.

Fig. 3.13 shows the effective area for the different neutrino energetic range.

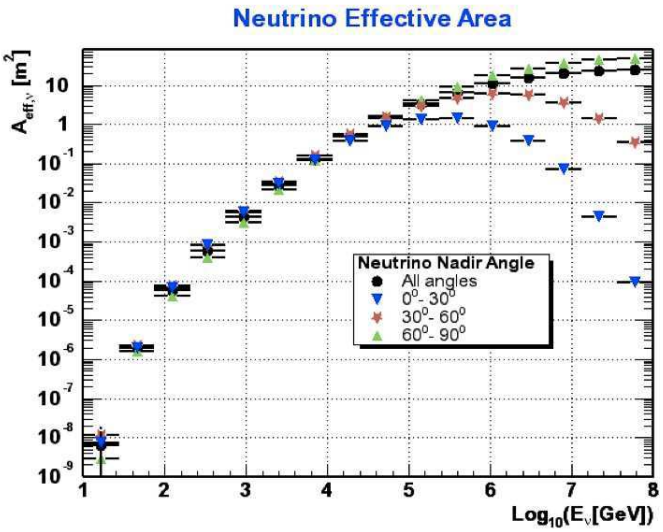

Figure 3.13: Effective area for neutrinos detected by ANTARES, as function of the neutrino energy for different angles of the primary neutrino. It can be noted that at the highest energies only the contribution from the component near the horizon has an appreciable effective area.

3.8.3 Angular resolution

Angular resolution is one of the most important features for a neutrino telescope. In ANTARES it is defined as the median of the distribution of the angle between the Monte Carlo neutrino direction and the reconstructed muon direction. The angular resolution is made up by two terms: one takes into account the kinematics, the other one the reconstruction. For the highest energies neutrino and produced muon are essentially aligned. When this occurs, all the errors which could spoil the pointing accuracy are due to the reconstruction of the muon trajectory.

Thanks to the water properties at the ANTARES site and the expected detector resolution, the angular resolution is better than 0.3° for neutrinos of energy greater than 10 TeV (Fig. 3.14). This is important to have a point-back to the cosmic neutrino sources.

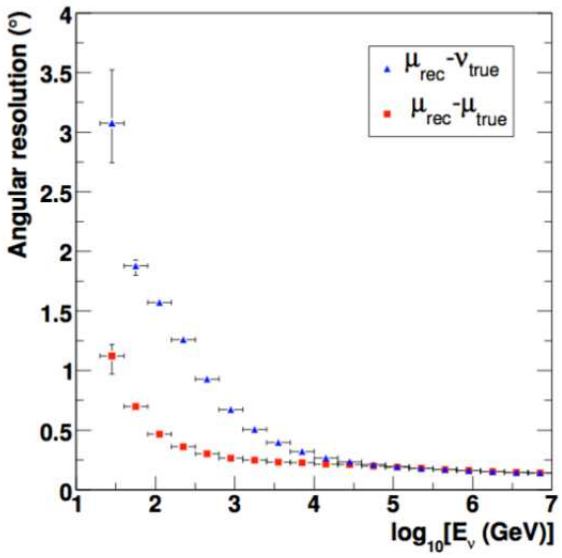

Figure 3.14: Angular resolution for ANTARES according to detailed simulation of the detector. The points represent the median of the angular error distribution for muons and neutrinos. Below 10 TeV the angular resolution is dominated by the kinematic angle between neutrino trajectory and muon track. Above this energy, it is dominated by the reconstruction.

Chapter 4

Monte Carlo Simulation Tools

The tools used to make simulation for this thesis are presented in this chapter. Also the chain of event generation (muons and neutrinos) used in the ANTARES experiment will be presented. There are three main steps:

- muons and neutrinos generation,
- particles propagation toward the detector volume,
- generation and propagation for Cherenkov radiation,
- coding of the signal inside the detector, along with a simulation for background noise.

At the end of this chain the event reconstruction follows, just like as for a physical event.

4.1 The SeaTray environment

ANTARES, like the majority of high energy physics experiments, deals with a huge amount of data on a daily basis. The raw data after triggering are more then 30 gigabytes per day, and all these data must be stored and later processed. To do so, a robust and reliable system of software is needed. In order to match this requirement and allow scientist to develop their personal code for each different analysis, it is desirable to have the entire software package organized in a modular way, so that the user can modify or add a single module, to perform a specific task, taking advantage of the simplicity of a fixed programming scheme. For this reason ANTARES and KM3NeT collaborations have adopted IceTray, the software framework used in the IceCube collaboration, detached from the IceCube version and modified in

order to suit the seawater detectors [76]. This new framework is named SeaTray. The user to follow a certain logic while developing software, so that the entire code remains readable by anyone who is familiar with this logic. At the same time it provides a large set of object classes and services that can be employed by the user in his own code.

This framework supplies a set of *dataclasses* C++ classes that describe how to store information such positions, directions, particles, hits or detector geometry. Each user can write SeaTray *modules*, objects dynamically linked into the framework which perform the actual data processing. Data is passed between modules in containers called *frames*, collections of dataclasses that can be written to disc or stored in memory. Each frame is associated with different *stream* corresponding to a different, aspect of the analysis. *Calibration frames* contain the calibration data of the detector, while *Geometry frames* describe the geometry of the detector, along with descriptions of optical modules and photomultipliers. The *Physic frame* stores all the typical event information, such as charge, times, simulated or real hits and reconstructed tracks.

SeaTray contains a set of classes that define its standard data format. By default it uses Boost libraries [77] for the I/O, but other methods and file types can be used, such as ROOT [78].

4.2 Simulation Tools

This part deals with the different programs used for the simulations, from the generation until the final reconstruction. It is necessary to study the different neutrinos sources and their flux on earth, so in ANTARES there are two main stages of simulation. First comes the neutrino interaction in the media in and around the detector volume, along with the propagation of the particles coming from the interaction. In the second stage there is the generation of Cherenkov light produced by the particles and the detector's response.

4.2.1 Generation requirement

In order to treat an easier problem, the detector volume is considered to be a cylinder which contains all the instrumentation. Outside this cylinder there is a larger one, called "the can". This can define the region where the Cherenkov light is generated, in order to determine the detector response. In this volume the full generation is performed.

The generator used for neutrinos study is called GENHEN [66]. It is

suitable for all the neutrino processes, from oscillations to high energy astrophysics (PeV range).

Statistical uncertainties should be at the level of 5%. To reach this level, the following requirements have to be satisfied:

- all the interactions must be correctly simulated in every energy range, from few GeV until the region of Deep Inelastic Scattering (DIS);
- there should be a correct proportion in the generation of neutrino interacting inside the can (volume events) and outside it (surface events);
- in the simulation of volume events, the Cherenkov light produced by shower at the interaction vertex must be take into account as light coming from secondary particles;
- the contribution of surface events is simulated as high energy muons, followed until they stop in the detector or reach the surface of the can;
- one must consider also the effect of the media (rock and water) surrounding the detector, which can affect the neutrino interaction or the muon propagation;
- in case of ultra high energy neutrinos the probability of absorption by Earth must be calculated, taking into account the neutrino interaction cross-section and the Earth density profile.

4.2.2 Event generator

The simulation of neutrino interactions inside the can is performed by GENHEN (v6r10), a software developed by the collaboration.

All the events are generated following a power-law spectrum ($E^{-\gamma}$) and they can be later weighted in order to obtain the different neutrino fluxes. Such an energy spectrum is motivated by the theory of Fermi shock acceleration. The direction of the generated particle is defined by the zenith angle θ and the azimuth angle χ. Events are sampled uniformly in the cosine of the zenith angle range $[\theta_{\min}, \theta_{\max}]$ and azimuth angle range $[0, 2\pi]$.

The chosen generation spectrum corresponds either to the flux of neutrinos at the interaction vertex close or inside the telescope, or to the flux of primary neutrinos crossing the Earth from the opposing side. A spectral index $\alpha = 1.4$ gives interacting neutrinos over all the energetic range. This value corresponds to a spectral index γ of 2.4 ($\alpha + 1$) for the neutrino flux

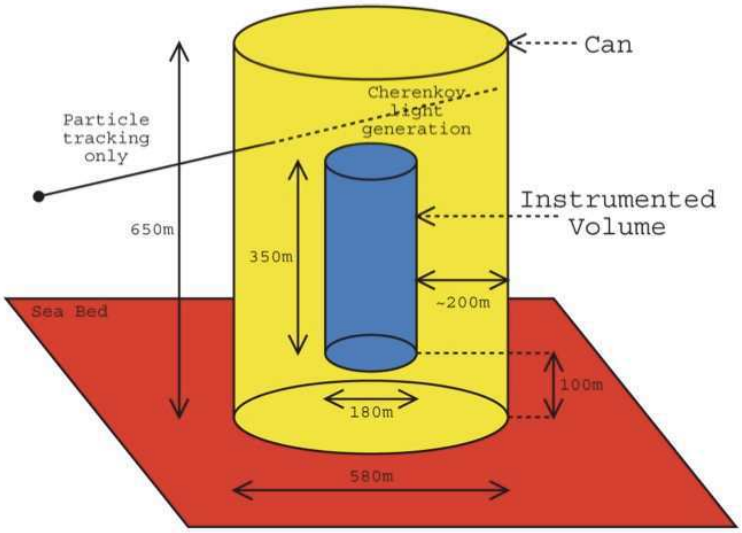

Figure 4.1: Definition of the ANTARES can. The can is built by extending the instrumented volume by three attenuation lengths (∼200 m), except from below where it is bounded by the sea bed from which no Cherenkov light can emerge. If the interaction vertex is outside the can, only the muon is propagated up to the can surface, since the Cherenkov light produced by the other particles would not reach the detector.

at the Earth surface. It is mandatory to have a full propagation of neutrinos inside the Earth in order to estimate the flux that reaches the detector.

In general, during the simulation there is the definition of a volume around the detector, where all the possible interactions for the observable neutrinos occur. The interactions are simulated inside that volume, while for neutrinos that interact outside the can the produced muon is propagated and stored if it reaches the surface of the can.

The maximum energy for the simulated muon corresponds to the upped limit on the neutrino energies $E_{\max}$, set by the user at as input parameter. This defines a maximum muon range $R_{\max}$ in water. In the neutrino interaction occurs farther than the maximum muon range, the muon cannot reach the detector. These distances allow to define the total simulation volume:

1. after the definition of $R_{\max}$, a cylindrical volume around the instrumented one is defined;

2. the energy range $[E_{\min},\, E_{\max}]$ is divided in equal bins in $\log_{10} E_\nu$. Also,

the calculation of the number of events N for each bin is performed;

3. A maximum range in rock and water is computed for each energy bin, relying on $E_{\max}$;
4. LEPTO integrates the cross-section in the energy bin of interest, initializing the generation in the energy range;
5. a loop over the number of events N_i^{scaled} inside the scaled volume starts:
   (a) inside the energy bin, the energy of the interacting neutrino is sampled according to the $E^{-\gamma}$ spectrum;
   (b) the neutrino position is chosen inside the scaled volume;
   (c) the vertex position is determined. If the interaction happens outside the volume, the shortest distance between the can and the neutrino last position is computed. If the distance exceeds $R_{\max}$, the event is rejected because the muon cannot reach the detector;
   (d) an isotropic distribution samples the neutrino direction. If the event is located outside the can, also the distance between the instrumented volume and the neutrino vertex is computed;
   (e) the particles produced in the interaction are simulated, using a dedicated code;
   (f) for events outside the can, only the information about the muon are kept;
   (g) the event weights are computed and event information are written on disk.
6. when all the stage above are completed, a record of every interesting event is stored and written on the output file.

4.2.2.1 Neutrino fluxes and event weights

The algorithm described above uses the user input power-law energy spectrum to generate events for the neutrino interaction rate. This could be interesting to calculate the effective areas and volumes, but to perform a physical analysis it is desirable to reweight the events to a particular differential neutrino flux.

Following the definition given in [67], the event weight is defined by the following parameters:

- V_{gen} (m^3): total generation volume;

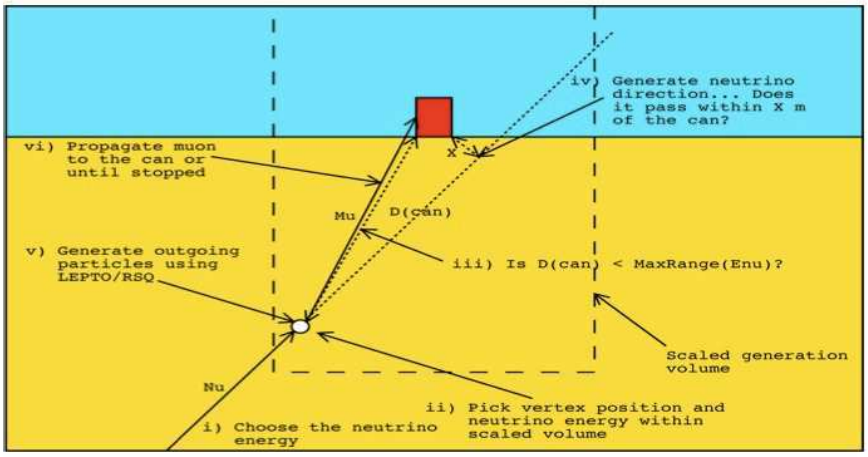

Figure 4.2: Schematic overview of the event generator algorithm.It begins by choosing the neutrino energy, then it compute the coordinates of the interaction vertex. If the muon track is not contained in the can, the volume is scaled and it is verified if the track passes inside this new scaled can. If it is positive, LEPTO generate the outgoing particle and the muon is propagated inside the can until it stops.

- I_θ (sr) $= 2\pi(\cos\theta_{\rm max} - \cos\theta_{\rm min})$: angular phase space factor depending on the specified range of $\cos\theta_\nu$. It is the integral of the solid angle;
- I_E: energy phase space factor depending on the input spectral index γ for the neutrino interaction rate. If $\gamma = 1$, $I_E = \ln(E_{\rm max}/E_{\rm min})$, otherwise $I_E = (E_{\rm max}^{1-\gamma} - E_{\rm min}^{1-\gamma})/(1-\gamma)$. It is the integral of the generation spectrum between the minimum and the maximum energy;
- $\sigma(E_\nu)$ (m^2): total neutrino cross-section of the charged current neutrino interaction;
- ρN_A (m^3): total number of target nucleons per unit volume (ρ is the target density and N_A is the Avogadro's number);
- $P_{\rm Earth}(E;\theta)$: probability of neutrino transmission through the Earth;
- $N_{\rm total}$: total number of generated events;
- $t_{\rm gen}$ (s): the arbitrary time represented by the simulation. This will appear in the flux calculations below and eventually cancel.

The following distribution describes the rate Γ_ν^I of interacting neutrinos (with units of $\mathrm{GeV}^{-1}\mathrm{m}^{-3}\mathrm{s}^{-1}\mathrm{sr}^{-1}$) from the generated events:

$$\frac{d\Gamma_\nu^I}{dE_\nu dV dt d\Omega} = \frac{E^{-\gamma}}{I_E}\frac{1}{I_\theta}\frac{N_{\mathrm{total}}}{V_{\mathrm{gen}}}\frac{1}{t_{\mathrm{ggen}}} \tag{4.1}$$

The number of generated events N_{total} is given by the integration of 4.1 over the range of angles, energy, time and volume simulated. The rate of interacting neutrinos depends on the incoming flux ϕ_ν (per unit area dS), the target density and the neutrino cross-section. It is interesting to convert the above interaction rate to obtain the neutrino events generated on so far. To do this, the interaction rate is divided by the target nucleon density and neutrino interaction cross-section:

$$\frac{d\phi_\nu}{dE_\nu dV dS dt d\Omega} = \frac{d\Gamma_\nu^I}{dE_\nu dV dt d\Omega}\frac{1}{\sigma(E_\nu)\rho N_A} = \frac{E^{-\gamma}}{I_E}\frac{1}{I_\theta}\frac{N_{\mathrm{total}}}{V_{\mathrm{gen}}}\frac{1}{t_{\mathrm{ggen}}}\frac{1}{\sigma(E_\nu)\rho N_A} \tag{4.2}$$

The latter is the neutrino flux which arrives on the detector. In turn, it represents the flux of neutrinos arriving on the Earth surface times the probability of transmission $P_{\mathrm{Earth}}(E;\,\theta)$, for a particular E_ν and θ_ν. Now it is possible to write the flux of simulated neutrinos arriving at the Earth surface:

$$\frac{d\phi_\nu}{dE_\nu dV dS dt d\Omega} = \frac{N_{\mathrm{total}}}{V_{\mathrm{gen}} I_\theta I_E E^\gamma \sigma(E_\nu)\rho N_A t_{\mathrm{gen}} P_{\mathrm{Earth}}(E;\,\theta)} \tag{4.3}$$

If a particular model is chosen, the flux can be expressed as:

$$\frac{d\phi_\nu^{\mathrm{model}}}{dE_\nu dV dS dt d\Omega} \equiv \phi(E_\nu;\, theta_\nu) \tag{4.4}$$

and the events can be re-weighted in each interval $dE_\nu d\theta_\nu$ by the ratio of the two fluxes at that point. To obtain a rate of events per second (setting t_{gen} equal to 1) corresponding to a specific neutrino flux model described by $\phi(E_\nu;\theta_\nu)$, each event sample is considered in the interval $dE_\nu d\theta_\nu$ from the simulation and weighted by the ratio of the model flux to the generated flux. In this way the weight W_{event} is computed with a flux independent part, called $W_{\mathrm{generation}}$, associated with each individual event for a particular model:

$$W_{\mathrm{generation}} = \left(\frac{V_{\mathrm{gen}} I_\theta I_E E^\gamma \sigma(E_\nu)\rho N_A t_{\mathrm{gen}} P_{\mathrm{Earth}}(E;\theta)}{N_{\mathrm{total}}}\right)$$
$$W_{\mathrm{event}} = W_{\mathrm{generation}} \cdot \phi(E_\nu,\, \theta_\nu)$$

The weight $W_{\mathrm{generation}}$ is computed for convenience during the generation phase. This allows for a range of different fluxes to be applied without recalculating all the individual elements of the weights. To obtain distributions or event rates corresponding to a particular model it is sufficient to multiply each event by its weight in the phase of histograms filling.

4.2.2.2 Neutrino absorption in the Earth

There is a possibility for the neutrino to be absorbed by Earth, depending on the neutrino cross-section and the density of matter through the Earth. The column density inside Earth can be parametrized as [43]:

$$\rho_l = \int_L \rho_{\text{Earth}}(r) dL \tag{4.5}$$

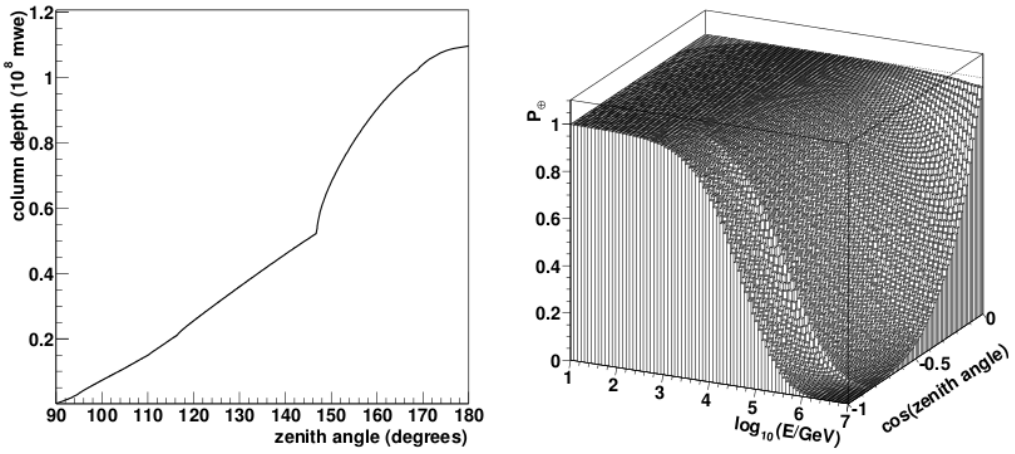

Figure 4.3: Left: The density of the Earth, integrated over the path of the neutrino as a function of the direction of the neutrino expressed in water equivalent meters. The kink in the figure is caused by the density discontinuity associated with the boundary of the Earth's core. Right: The probability of a neutrino to traverse the Earth without undergoing an interaction as a function of the direction (zenith angle) of the neutrino and its energy.

When the neutrino's direction has an angle greater than 145° the probability of absorption in enhanced due to the increasing density of the Earth core. The probability that a neutrino is able to cross the Earth is expressed as:

$$P_{\text{Earth}}(E_\nu;\, \theta_\nu) = \exp\left(-N_A \sigma(E_\nu) \rho(\theta)\right) \tag{4.6}$$

The shape is shown in Fig. 4.3 (right), with the probability as a function of the energy and zenith angle of the incoming neutrino. This probability is fundamental in the computation of the expected event rate in the simulation. For neutrinos with angles close to $\cos\theta = -1$, the absorption probability shows a maximum for energies above 10 TeV, while above 1 PeV only neutrinos close to the horizon remain unattenuated.

4.2.2.3 Atmospheric neutrino flux

Neutrinos from atmospheric background are the main source of signal in the ANTARES detector. Their flux can be computed in different ways, depending on the measurements of the primary cosmic ray flux and the models used for the interactions with the atmosphere. The most known ones are the models developed by Honda (HKKM) [68] and Bartol [69].

These calculations depend on the measured cosmic ray spectrum and extrapolation of hadronic interaction models to high energies. There are of course some uncertainties on the high energy atmospheric neutrino flux [70], estimated to be of order of 20% using the two inputs above as reference. The good agreement between the two models is a result of a cancellation between the differences in the primary cosmic ray spectrum used and the hadronic interaction models. The actual uncertainty is much larger than the difference between these two models suggests. In this analysis the default Bartol flux is used, with the extension to the high energy range as written in tables in [71].

In addition to the conventional neutrino flux produced by pions and kaons decays from cosmic showers, also the so-called prompt neutrino flux must be taken into account. It originates from the decay of charmed mesons with energy above 10^5 GeV. The interested range changes depending on the extrapolation of charm production cross-sections from accelerator energies. There are three main models for charm production[72]: Quark-Gluon String Model (QGSM), Recombination Quark Parton Model (RQPM) and Perturbative QCD (pQCD).

4.3 Atmospheric muon simulation

Muons resulting form the decay of particles produced in the CRs interaction with the atmosphere compose the largest part of the signal detected by a neutrino telescope. Even if ANTARES is shielded by the large amount of water above, a large flux of high energy atmospheric muons is able to reach the instrumented volume of the detector.

The main problem with the atmospheric muons is that they can mimic fake upgoing tracks with their Cherenkov light production. This signature can be confused with the genuine cosmic signal. On the other hand, atmospheric muons are useful to test the offline software, to check the good functioning of the detector and to estimate uncertainties.

A full MC simulation can reproduce accurately atmospheric muon bundles. The starting point is the simulation of primary CRs in their interaction

with the atmosphere, using software like CORSIKA [73], followed by the simulation of the air shower and the propagation of the muons through the sea water. This process is extremely time consuming, and therefore it is not easy to produce a large statistical sample.

In order to save computing time, it is mandatory to have a fast MC generator. ANTARES collaboration uses the MUPAGE package [74]. This software had been developed starting from the flux, the angular distribution and the energy spectrum of underwater muon bundles [75]. The muon flux and energy are parametrized in terms of the bundle multiplicity m. MUPAGE returns in output the kinematics of atmospheric muon bundles at the surface. Event generation is not weighted and the livetime corresponding to the simulated events is calculated automatically. On the other hand, the user is not able to change the generation spectrum.

4.4 Particle propagation and generation of light in water

All the information concerning long-lived particles generated by the software are stored and two GEANT-based packages [79], KM3 [80] and GEASIM, track the particles through the water in the sensible volume. For the water properties the values recorded at the experimental site are used.

GEASIM is in charge of tracking all the particles but muons. It takes into account all the physics processes such as energy loss, multiple scattering, radiative processes and hadronic interactions. At each tracking step the Cherenkov cone produced by charged particles is calculated. For all the OMs which are in the cone the hit probability is determined and converted into a photo-electron number using Poisson statistics. The wavelength considered is in the range of $300 \div 600$ nm and to evaluate the hit probability several factors (wavelength dependent absorption length, quantum efficiency and transmission coefficients of the glass sphere and the gel) are taken into account. Another important value which can affect the hit probability is the relative orientation of the PMT with respect to the Cherenkov front, along with the angular acceptance. The uncertainty on the angular acceptance of the OMs is the main systematic source of uncertainty for the simulated flux of atmospheric neutrinos and muons.

The arrival time is calculated based on the group velocity of the photon front and includes smearing factors from the TTS (time transit spread) of the PMT as well as from the wavelenght dispersion, where the latter depends on the distance between tack segment and OM. This effect can make

the Cherenkov cone fuzzy. The angular distribution of the Cherenkov light emitted in the shower is shown in Fig. 4.4. There is the Cherenkov peak well visible, while the tails extend over the whole angular range. In this way it is much more easy and time saving to parametrize the Cherenkov light production in a electromagnetic shower. Hadronic showers exhibit much larger fluctuations, occasionally giving rise to secondary muons, and thus no parametrization is used. The simulation of the adronic part is done with the package GHEISHA which is generated in GEANT [79].

It is mandatory to include also the effect of light diffusion when treating muon propagation. Before simulating physics events, a set of scattering tables is created. If the muon track is longer than one meter, it is sent to a dedicated GEANT-based program within a large water volume. All the radiative process below a given energy threshold (0÷1 GeV) are taken into account along with energy loss and multiple scattering. Cherenkov photons are created one by one and tracked in water, by a precise diffusion and absorption model, which allows to track each photon, including its scattering before the absorption. Each time a photon penetrates one of several concentric spheres around the muon track origin, its position, direction and time are stored. This photon field is then convoluted with possible orientations of OMs in the spheres which leads to a hit probability table in a 5 dimensional parameter space: R (distance from the muon origin), θ (latitude of the sphere), the pair (ϑ, φ) (orientation of OM with respect to muon direction), t (photon arrival time). Similar scattering tables are created also for electromagnetic shower and stored for the following processing step. Now muons from physics generator events are tracked in the usual can volume by MUSIC [81]. At the end of tracking for Cherenkov photons, the hits probabilities for all OMs are evaluated using the scattering tables. One set of scattering tables can be reused as long as the underlying scattering and absorption model does not have to be change.

4.5 Detector response and trigger simulation

A program called TriggerEfficiency program [82] is in charge to simulate the detector response. This software adds an optical background to the hits generated by physical events, the simulation of the electronics and the triggering of the events.

The optical background can be generated and added to the MC events, according to a Poisson distribution, using a fixed background rate specified by the user (for example a mean optical rate of 60 kHz), or using real data run. In this second case the TriggerEfficiency program adds to the PMTs a

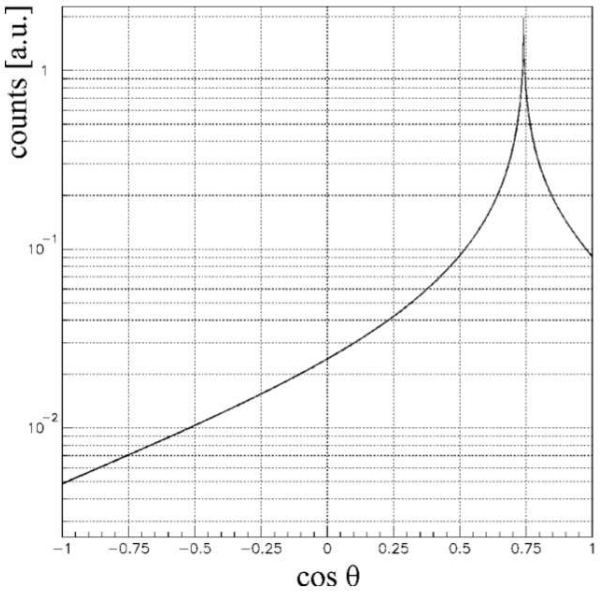

Figure 4.4: Angular distribution of Cherenkov light for electromagnetic showers with respect to the shower axis. The Cherenkov peak is well visible, while the tails extend over all the angular range.

background which corresponds to a counting rate taken from real detector simulation. In this way also the biological activity, such as bioluminescence or biofouling, or temporary problems related with electronics (charge saturation, temporary power off of single PMTs, sparks) are taken into account.

The front-end ARS chip integrates the analogue signal from the PMT over a typical time window of 25 ns. This is simulated by summing the number of detected photons in that window. After this integration, ARS cannot take data for about 250 ns. A second ARS, connected to the same PMT, digitizes signals arriving afterward. The time resolution for a single photo-electron signals is 1.3 ns and decreases for higher amplitudes. To simulate this effect, the hit times are smeared using a Gaussian function with a width $\sigma = 1.3$ ns$/\sqrt{N_\gamma}$, where N_γ is the number of simultaneously detected photons. The so-called level zero trigger (L0) selects hits that have a charge greater than a low threshold, typically set at 0.3 pe. The amplitude measurements is then simulated by smearing the integrated number of photons with an empirical function. This function results in a (roughly Gaussian) smearing of about 30% [82]. The dynamic range of the charge integration has a saturation level which correspond to about 20 photo-electrons.

Monte Carlo events are triggered with the same trigger algorithm used for real data. The first level trigger (L1) is built up of coincidence hits in the same storey within a 20 ns time window and a single hits with a large charge amplitude, greater than a high threshold tunable from 3 pe to 10 pe. A trigger logic algorithm, a level 2 trigger (L2), is then applied to data, operating on the L1 hits. The main physics triggers are the 3D-directional scan logic trigger 3N and the cluster logic trigger 2T3.

The 3N trigger process all data and declares an event as soon as a minimum number of L1 hits are found within a 2.2 μs time interval. In addition, each pair of L1 hits should verify the causality relation:

$$\Delta t_{ij} \leq \frac{d_{ij}}{c/n} + 20 \text{ ns} \tag{4.7}$$

where Δt_{ij} and d_{ij} are the time difference and the spatial distance between $(\text{hit})_i$ and $(\text{hit})_j$ respectively, c is the speed of light and n the index of refraction of the sea water. Eventually an extra scan of direction (1D trigger) is applied. The 1D trigger implements a standard 1-dimensional trigger looking for time correlated hits from a muon in a given direction.

The 2T3 trigger is based on the definition of T3 cluster of hits [83]. A T3 cluster is defined when two L1 hits on three adjacent storeys are in coincidence. The coincidence time window is set to 100 ns in case that the storeys are adjacent, and to 200 ns in case of next to adjacent storeys. The

2T3 trigger logic requires at least two T3 clusters within a time window of 2.2 μs.

The output of the TriggerEfficiency routine is in the same format (a *.root file) as the real raw data.

4.6 Track reconstruction

The track reconstruction relies on algorithms which estimates the direction and position of the muon, starting from the arrival times and amplitudes of the hits. In ANTARES there are two main reconstruction strategies, both in use and exploited for the different analysis, based upon different criteria: AAFit and BBFit. The first one is considered the high efficiency track reconstruction, while the second is the faster one.

4.6.1 The AAFit reconstruction strategy

4.6.1.1 Track description and relation to the OM

There are two main parameters which characterize the muon trajectory: the direction $\vec{d} = (d_x, d_y, d_z)$ and the position $\vec{p} = (p_x, p_y, p_z)$ of the muon at some fixed time t_0. Knowing that at energies above the detection ($\sim$10 GeV) the muon is relativistic, its speed is taken equal to the speed of light in vacuum. Zenith θ and azimuth ϕ angles are used to parametrize the direction as $\vec{d} = (\sin\theta\cos\phi, \sin\theta\sin\phi, \cos\theta)$. During the reconstruction is necessary to estimate five independent parameters. For a given track with known position and direction and an OM at position $\vec{q}$, whose field of view if oriented in the direction $\vec{w}$, there are three main relevant properties to take into account for an emitted Cherenkov photon:

- the theoretical arrival time of the photon (t^{th});
- the expected photon path length (b);
- the expected cosine of the angle of incidence of the photon on the OM (a), i.e. the angle between the direction of the photon and the pointing direction of the PMT.

With these three quantities it is possible to characterize the position and the orientation of the OM relative to the track. The true arrival time, path length and angle of incidence may differ from these values, because of photons emitted by secondary electrons and inferences due to the scattering.

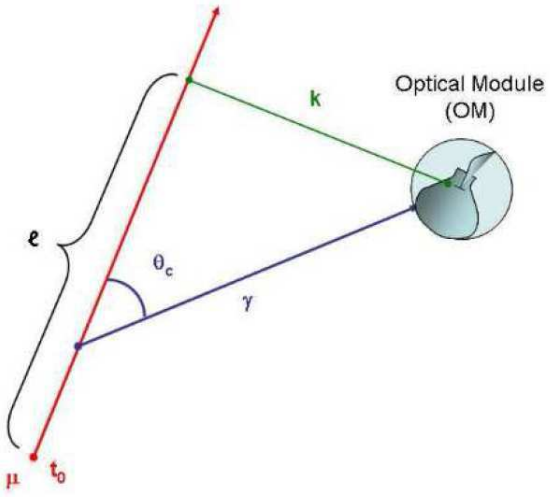

Figure 4.5: Description of the geometry of the detection of the Cherenkov light. The muon trajectory is identified by the red line. The Cherenkov light is emitted with an angle of θ_c with respect to the muon track and is detected by the OM. The blue arrow indicates the path of the light.

The theoretical time t^{th} is defined relying on the quantity:

$$\vec{v} = \vec{q} - \vec{p} \tag{4.8}$$

Knowing that the components of $\vec{v}$ parallel and perpendicular to the muon direction are $l = \vec{v} \cdot \vec{d}$ and $k = \sqrt{\vec{v}^2 - \vec{l}^2}$, the arrival time of the light in $\vec{q}$ is given by:

$$t^{th} = t_0 + \frac{1}{c}\left(l - \frac{k}{\tan\theta_c}\right) + \frac{1}{v_g}\left(\frac{k}{\sin\theta_c}\right) \tag{4.9}$$

where v_g is the group velocity of light (value taken at 460 nm). The second term is the time the muon takes to reach the point where the detected light is emitted, while the third term is the time the light takes to travel from that point to $\vec{q}$. The length of the photon path is given by

$$b = f\frac{k}{\sin\theta_c} \tag{4.10}$$

while the cosine of the angle of incidence of the photon on the OM is given by:

$$a = \left[\vec{v} - \vec{d}\left(l - \frac{k}{\tan\theta_c}\right)\right] \cdot \vec{w} \tag{4.11}$$

where $\vec{w}$ is the pointing direction of the OM.

4.6.1.2 Summary of the full reconstruction algorithm

Track reconstruction passes through several steps and its final result is the best estimation for track direction. These are the main reconstruction steps:

- **Preselection of hits**: this is a first selection to exclude hits due to the optical background. Hits selected must have $|\Delta t| \leq \frac{d}{v} + 100$ ns, where Δt is the time difference between a hit and the hit with the largest amplitude in the sample and d is the distance between the OMs of the two hits.

- **Linear prefit**: it is a linear fit through the positions of the hits, with the hit time as an independent variable. It is assumed that all the hits occur on points that are located on the muon track. Its main advantage: it does not require a starting point. It takes into account only hits in local coincidence (combination of two ore more hits on one floor in a time window of 25 ns) or with an amplitude larger than 3 pe.

- **M-estimator fit**: this method is weakly sensible to the quality of the linear prefit. The hits used in this step are selected on the basis of the result of the prefit. Hit time residuals are computed using the prefitted track, selecting hits that are far less than 100 meters from the track and with a time residual in the interval [-150, 150]. Hits with an amplitude greater than 2.3 pe are equally kept. Last step is the application of a minimization function to enhance the precision of track parameters.

- **Maximum likelihood with the original PDF**: it has the same hit selection as the previous step. It consists of the ML fit with the original PDF. Time residuals are computed using the track from M-estimator. Hits are selected if their time residual are in the interval [-0.5 R, R], where R is the root mean square of time residual distribution. Hits with amplitudes greater than 2.5 pe and in coincidence are also selected. The asymmetry in the selection interval reflects the fact that the original PDF is asymmetric.

- **Repetition of steps 3 and 4 with different staring points**: to make the algorithm efficiency better, the two previous steps are repeated changing the starting point with respect to the prefit. Rotating the prefit track by an angle of 25^o for of the additional starting point are obtained. The origin of rotation is the point on the track that is closest to the center of gravity of the hits. Four more starting points are obtained by translating the track ± 50 m in the direction $\vec{d} \times \vec{x}$ and

± 50 in the $\vec{z}$ (upward) direction. In total, steps 3 and 4 are thus done nine times.

- **Maximum likelihood fit with improved PDF**: the last step is done starting from the preferred result obtained in the previous step. Hits are selected if they have residuals between -250 and 250 ns with amplitudes larger than 2.5 pe or in local coincidences. Since background is taken into account in the PDF, the presence of background hits in the sample does not spoil the reconstruction accuracy.

The rejection of misreconstructed tracks can be made using two reconstruction quality related variables: the log-likelihood per degree of freedom ($\log(\mathcal{L})/N_{\mathrm{DOF}}$) and the number of compatible solutions (N_{comp}) found by the reconstruction program. The variable Λ combines the two quantity above and has been chosen as the quality fit estimator:

$$\Lambda = \frac{\log(\mathcal{L})}{N_{\mathrm{DOF}}} + 0.1(N_{\mathrm{comp}} - 1) \tag{4.12}$$

4.6.1.3 Performances

There is a fraction of 1.1% of tracks that are reconstructed with an error smaller than 1^o at the linear prefit stage. After the M-estimator stage this fraction rises up to 38%, than up to 57% after applying the original PDF. Last step enhances efficiency up to 59%, which is not so significant on the whole reconstruction strategy. The last step is however able to raise to 20% the tracks reconstructed with a precision lesser than 0.1°. In Fig. 4.6 the error on the reconstruction at every stage is shown.

Reconstruction in details is presented in [84].

4.6.2 The BBFit reconstruction strategy

The BBfit algorithm does not precise positioning calibration, relying on a strict hit selection and still keeping a good efficiency. In this strategy, both a detector line and a muon track are considered as straight lines in space and a point of closest approach for the muon is defined. The Cherenkov light produced must be in the vicinity of this point to be considered for the fit.

The geometry of the optical modules plays no important role, since storeys are considered as space points centered on the detector line. To be considered as hits to be fitted, a calibration on time for time and charge is applied and only one hit per storey is allowed in the fitting procedure. The event hits are then ordered and merged in time and amplitude if closer than 20 ns (the

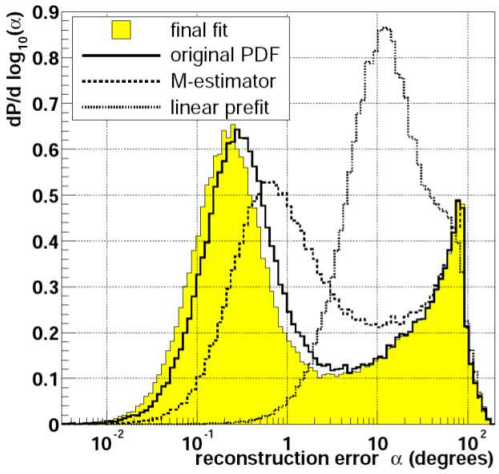

Figure 4.6: Distribution of the reconstruction angle for tracks in different stages of reconstruction. The error is reduce more and more at the progressing stage of the distribution. The final stage is the one with the smallest error.

time kept is the one of the first hit). All the hits must be triggered as L1 hits and if there are two L1 hits in two adjacent floors within 80 ns or within 160 ns in two next-to-adjacent floors, a T3 is defined. The hits contributing to a T3 are then selected for the fit. New hits are then searched for within a time window around the T3 times, calculating their expected hit time in an adjacent floor, assuming these hits arrive linearly in the z-t plane, as a plane wave front. These hits are searched in an asymmetric time window because of the generic shape of the Cherenkov cone with a recursive procedure.

The detector geometry is considered invariable, using the measured BSS positions from acoustic triangulation. In these configurations, lines are perfectly vertical, thus lines distortions due to sea current are ignored, and the detailed geometry of a floor is considered negligible.

4.6.2.1 Fitting procedure

Before fitting, the list of selected hits is examined and if there are less than 5 hits, no fit attempt is made. There are two procedures depending on the number of lines involved: a single line or a multi lines.

Ignoring all the effect due to multiple scattering and other deviations, the track is considered a straight line in space, with the particle moving a the speed of light in vacuum. Space-time points are parametrized as:

$$\vec{p}(t) = \vec{q}(t_0) + c(t - t_0)\vec{v}_0 \tag{4.13}$$

where the particle passes through point $\vec{q}$ at time t_0 moving in the direction $\vec{v}$. The track is defined by a total of 5 parameters: the three $\vec{q}$ coordinates and two angles to define $\vec{v}$. If a detector line is described as (0,0,z), the point of closest approach is defined:

$$z_c = \frac{q_z - v_z(\vec{q}\cdot\vec{v})}{1 - v_z^2} \tag{4.14}$$

while its time is:

$$t_c = t_0 + \frac{q_z v_z - \vec{q}\cdot\vec{v}}{c(1 - v_z^2)} \tag{4.15}$$

at the distance of:

$$d_c = \sqrt{p_x^2(t_c) + p_y^2(t_c) + (p_z(t_c) - z_c)^2} \tag{4.16}$$

In this way the track is conveniently parametrized.

To build a fitting function it is necessary to know the time arrive t_γ of a Cherenkov photon on the line, its travel path d_γ and its inclination with respect to the line ($\cos\theta_\gamma$). These values can be derived from the parameters above:

$$d_\gamma(z) = \frac{n}{\sqrt{n^2-1}}\sqrt{d_c^2 + (z - z_c)^2(1 - v_z^2)} \tag{4.17}$$

$$t_\gamma(z) = (t_c - t_0) + \frac{1}{c}\left((z - z_c)v_z + \frac{n^2-1}{n}d_\gamma(z)\right) \tag{4.18}$$

$$\cos\theta_\gamma(z) = (1 - v_z^2)\frac{z - z_c}{d_\gamma(z)} + \frac{v_z}{n} \tag{4.19}$$

where $n = 1.38$ and it is the refractive index. All the dispersion and group velocity effects are ignored.

On the other hand, if the event has a structure more bright point-like, the emission of light is assumed to be isotropic. This model is applied to sources such as LED and laser beacon, but also to sparks and electromagnetic or hadronic showers. Each bright point is defined by four parameters: the position $\vec{q}$ and the time t_0. The distance of closest approach is then calculated, taking into account that for a bright point we have $z_c = q_z$ and $t_c = t_0$, thus:

$$d_c = \sqrt{q_x^2 + q_y^2} \tag{4.20}$$

With these three parameters, the bright point is located with respect to a single detector line. It is now possible to compute the parameter of a photon arriving on the line:

$$d_\gamma(z) = \sqrt{d_c^2 + (z - q_z)^2} \tag{4.21}$$

$$t_\gamma(z) = t_0 + \frac{n}{c} d_\gamma \tag{4.22}$$

$$\cos\theta_\gamma(z) \frac{z - q_z}{d_\gamma} \tag{4.23}$$

The fitting function relies on the difference between the measured hit time t_i and the expected time of the photon t_γ, computed for a track or a bright point, like in a χ^2 procedure. In a second time, the expected amplitude versus distance relation of the measured hit amplitudes a_i is computed:

$$Q = \sum_{i=1}^{N_{hits}} \left(\frac{(t_\gamma - t_i)^2}{\sigma_i^2} + \frac{a(a_i) d(d_\gamma)}{\langle a \rangle d_0} \right) \tag{4.24}$$

where the time error σ_i is set at 10 ns for amplitudes greater than 2.5 photoelectrons and 20 ns otherwise. The second term is not organized as a difference between theoretical value and measured amplitude in order to avoid penalties from large theoretical amplitudes. Instead, the chosen form gives a penalty to the combination of high amplitude and large distance. Instead, the combination of hits with large amplitude and large distance is penalized. The amplitudes are first corrected with the angular acceptance of the floor in question:

$$a_i' = \frac{2 a_i}{\cos\theta_\gamma + 1} \tag{4.25}$$

thus the average amplitude is computed with these corrected hit amplitudes:

$$\langle a \rangle = \frac{1}{N_{\text{hits}}} \sum_{1}^{N_{hits}} a_i' \tag{4.26}$$

Before use them in the fit function, the amplitudes are still modified as following:

$$a(a_i) = \frac{a_0 a_i'}{\sqrt{a_0^2 + a_i'^2}} \tag{4.27}$$

This function introduces an artificial saturation at $a_0 = 10$ pe, to obtain $a \sim a'$ for $a_i' \ll a_0$, and $a \sim a_0$ if $a_i' \gg a_0$. In this way the influence of the large dispersion in the dynamic ranges of the different modules is limited. A quite similar modification is applied also to the distance:

$$d(d_\gamma) = \sqrt{d_1^2 + d_\gamma^2} \tag{4.28}$$

where $d_1 = 5$ m. This avoids an excessive pull of the fit object toward the detector line.

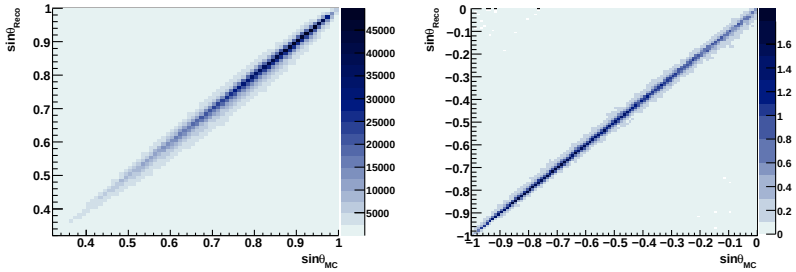

Figure 4.7: Correlation between reconstructed and simulated elevation angle. On the left for downgoing atmospheric muons, on the right for upgoing atmospheric neutrinos [86].

At the end, a procedure of minimization using the MIGRAD function of MINUIT is applied, for both bright point or track hypothesis. After minimization, the value of the fit quality, divided by the number of degrees of freedom, is retained for further analysis [85].

4.6.2.2 Performances

The accuracy in the reconstruction of the angle with respect to the horizontal plane (elevation angle), required to be well reconstructed to separate upgoing and downgoing tracks, is shown in Fig. 4.7. The reconstructed elevation angle is plotted as a function of the true elevation angle, for muons and atmospheric neutrinos, reconstructed in as multilines events. More than 95% of fits converge for all events with selected hits on at least two lines. Most events are located within a narrow band around the diagonal and 80% of the events have their elevation angle reconstructed with an error smaller than 5°. The agreement is robust even when the triggered atmospheric muon events are muon bundles, reconstructed as a single track [86].

4.7 Monte-Carlo samples

In this thesis two main kinds of simulation have been used: muonic neutrinos (along with antineutrinos) and muons. In ANTARES experiment the current simulations exploited are called *run by run simulation*. This system, used in ANTARES since 2010, is based upon the idea to produce a sample of muons or neutrinos for each run recorder by the detector. It allows to follow the detector behavior, with several thousands of Monte-Carlo events available to be compared to each data run, and have a more reliable estimator for the analysis. At the top the simulation chain, only the run number

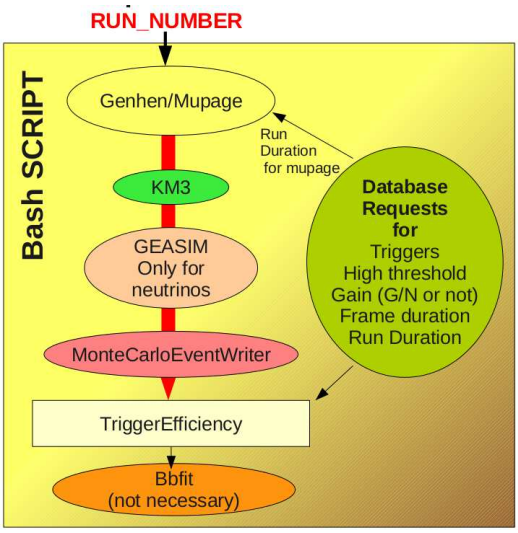

Figure 4.8: Schematic view of the simulation chain before the reconstruction stage. It begins with the generation phase (GENHEN/MUPAGE), to go through detector simulation (KM3) and hadronic interaction computation (GEASIM). The different triggers are then taken into account (TriggerEfficiency) before the final reconstruction step.

is injected. With it, it is possible to extract from data detector conditions for the particular period, calibrations and all the needed parameters for the following sub-programs (Fig. 4.8).

4.7.1 Neutrinos

There is no difference at the generation and reconstruction stages between atmospheric and astrophysical neutrinos. The same files are used for both signal and background, applying different weights depending on the chosen flux.

4.7.1.1 High energy range (up to 10^8 GeV)

For this simulation, ν_μ and $\overline{\nu}_\mu$ events interacting via charged current interaction are produced. The energy range has been split in two, a high energy range (100-10^8 GeV) and a low energy one (5-3000 GeV). The spectral index of the generated spectrum is -1.4 in both cases [87].

In the following steps of the chain, KM3 propagates the primary muons, while GEASIM takes care of all the other particles. The OM response is split between KM3/GEASIM and TriggerEfficiency.

To summarize the details of this simulation:

- two energy range, 100-10^8 GeV and 5-3000 GeV;
- for each run, 5×10^8 events are generated;
- generation performed on the whole solid angle;
- the flux used to weight the atmospheric events is the Bartol one;
- the probability density function for the interaction is the one defined by [47].

4.7.1.2 Ultra high energy range ($10^8 - 10^{10}$ GeV)

In order to complete the already existent simulation sample, I have performed a personal simulation production restricted to the energy range $10^8 - 10^10$ GeV. The simulation chain has not been changed, only some parameters of the GENHEN part has been adapted for this particular request. To briefly summarize them:

- energy range restricted to $10^8 - 10^{10}$ GeV;
- generation performed on the whole solid angle;
- for each run, 9×10^6 events are generated.

4.7.2 Muons

As said previously, the atmospheric muonic component is simulated with the software MUPAGE. For this kind of analysis, two productions of muons with different parameters has been exploited.

4.7.2.1 Low multiplicity muon bundles

This simulation production is the standard one used for analysis in the whole ANTARES collaboration. It concerns atmospheric muons in the energy range 4 GeV - 1 PeV, simulated between 0° and 85°. Each shower generated with these parameters must have a multiplicity between 1 and 200, with an energy threshold of 0.02 TeV.

For reasons of CPU time, it has been decided to generate only one third of the livetime of the whole simulation volume. To take into account this deficit, an appropriate weight is applied to the simulation at analysis stage.

4.7.2.2 High multiplicity muon bundles

In order to have a better background estimation in the case of an ultra high energy analysis, it is mandatory to take into account also the muonic component when the latter has an high multiplicity. In order to have a sort of high energy background estimation, also the minimum energy threshold of all muons combined in the event bundle should be higher than the standard one.

To accomplish this, I have performed a special production of muons, always exploiting the MUPAGE software, with a maximum multiplicity of 1000 and an energy threshold for the shower of 3 TeV.

A potential problem for this production is the huge CPU time required to generated the high multiplicity muons. Instead of generating one third of each run livetime, it has been chosen to fix instead the number of generated events per run. This has an effect on the run livetime, which is calculated automatically [74]. Since the flux of muon bundles of a given multiplicity m is known for each value of depth H at a given zenith angle ϑ_i, the expected rate on the *can* upper disk at the depth $H = H_{\min}$ is:

$$\dot{N}_{MC}(\Delta\Omega_i) = \Phi(H_{\min}, \theta_i, m) \cdot S \cdot \Delta\Omega_i \quad [\mathrm{s}^{-1}] \tag{4.29}$$

where, $\Delta\Omega_i = 2\pi(\cos\theta_{1i} - \cos\theta_{2i})$ is the solid angle centered at $\theta_i = (\theta_{1i} + \theta_{2i})/2$, and $S = \pi R_{ext}^2 \cos\theta_i$ $[\mathrm{m}^2]$ is the projected area of the upper disk. The equivalent livetime is computed from the number of generated events $N(\Delta\Omega_i)$ on the upper disk in the solid angle $\Delta\Omega_i$ as:

$$T(\Delta\Omega_i) = N(\Delta\Omega_i)/\dot{N}_{MC}(\Delta\Omega_i) \quad [\mathrm{s}] \tag{4.30}$$

The livetime is computed as the weighted average on 33 different solid angle regions of $T(\Delta\Omega_i)$, which have the same value, within statistical error.

For this production, 1827 runs taken randomly on the period 2008-2011 have been used to start the production. Each run has a livetime of 3800 s, for a total production time of more than 80 days. In order to apply this background to the other run by run simulations, it is necessary to scale it to the desired livetime.

Chapter 5

Diffuse Flux analysis

In this chapter it is presented the analysis of simulations in search of a diffuse neutrino flux in a very high energy range, for a Waxman-Bahcall flux and a cosmogenic one. The presence of an astrophysical signal is registered as an excess of events over the atmospheric background, without any particular assumption on the source direction. A limit on the sensitivity for ANTARES detector, relying on the simulations described in the previous chapter, will be presented.

To perform this analysis, in the ideal case the energy of every event should be estimated to evaluate if the event is signal or background. Even if some energy estimators are current developed for ANTARES detector, there is no reliable method able to estimate events of such elevate energy. To perform this analysis, it has been chosen a set of six variables, each one representative of one aspect of the event, to later use a combination of them to evaluate the events.

Before combining the variables into one single estimator, it is necessary to clean the sample from misreconstructed events. For this reason, some sequential cuts has been defined. Moreover, to maximize the possibility to kept signal over background and search in particular for ultra high energy events, a cut on the zenith angle near the horizon has been defined.

The last step concerns the statistical analysis of the multivariate estimator. Finally, the Model Rejection Factor techniques has been use to estimate ANTARES sensitivity for both the flux models of interest.

5.1 Simulation summary

The simulations for neutrinos and muons are those described at the end of the previous chapter, following the run by run policy. The two main

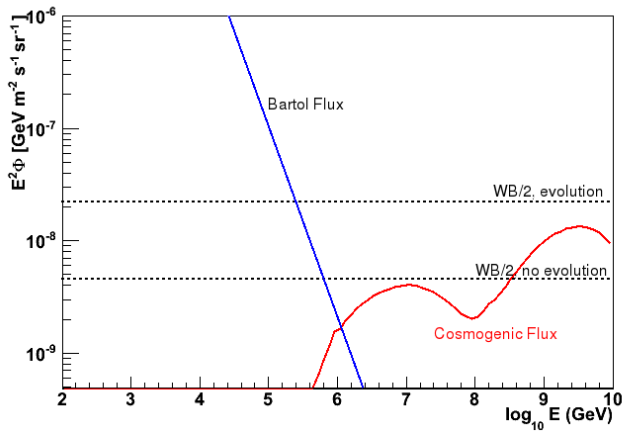

Figure 5.1: Summary of all the neutrino fluxes exploited in this analysis. The signal has been weighted using in the first case the Waxman-Bahcall flux taking into account sources evolution, in the second case a cosmogenic neutrino flux, in the hypothesis of protons at the CRs sources. The atmospheric background component has been weighted with the Bartol flux.

samples are neutrinos (standard plus ultra high energy custom simulations) and muons (standard plus high multiplicity).

Neutrino productions must be weighted in order to have atmospheric neutrinos and cosmic signal. The generic weight to apply to the simulations is defined in Par. 4.2.2.1. This latter is then multiplied by the flux of interest, being it an astrophysical flux for the signal or an atmospheric one for the background (Fig. 5.2).

5.2 Criteria for data quality selection

Before beginning into applying quality cuts or analysis high-level cuts, it is mandatory to define some requirements for the runs to be analyzed. Normally this stage should be applied directly to data, but knowing the run by run character of ANTARES simulations (described in the previous chapter), it is mandatory to select the runs with the best quality parameter, in order to exploit only their corresponding simulations runs and estimate a realistic sensitivity for the detector.

The selection of the runs according to detector conditions is based on a flag of data quality stored for each run and called quality basic. It is a parameter which regroups some low-level data quality parameters concerning detector or environmental conditions and their effect on the run during the

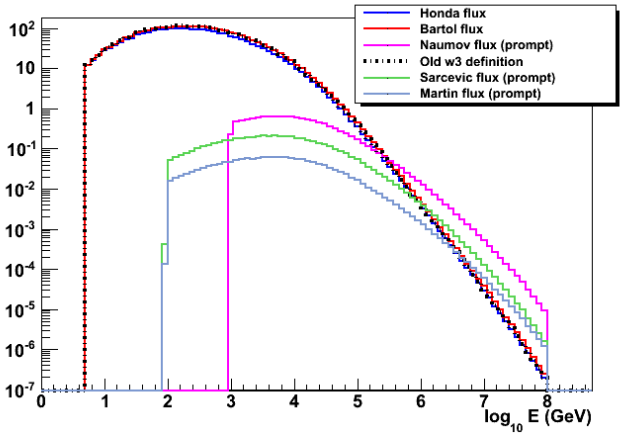

Figure 5.2: Plot of the possible neutrino energy weighted all the atmospheric fluxes considered for ANTARES analysis. There are two flux diffuse flux model (Bartol and Honda) and three prompt one (Martin, Sarcevic and Naumov).

data taking. The quality basic flag can take five different values:

- **QB=0**: possible pathological run, it is unwise to use it for the analysis. These runs come from period when detector is not reliable for data taking, because of sea operations or malfunctioning or testing;
- **QB=1**: basic selection, minimum requirement for a run to be included in the analysis. These are the minimum requirements for this flag:
  - a run must have an effective duration of $T_{\text{eff}} > 1000$ s;
  - there are no double frames;
  - there are no problems of synchronization;
  - for 2007 runs, the sampling must be smaller than three;
  - the muon rate must be between 0.01 Hz and 100 Hz;
  - the apparent duration i.e. the time from run start to run stop must be quite similar to the effective duration: $0 \geq T_{\text{app}} - T_{\text{eff}} \geq 450$ s;
- **QB=2**: the same requirements as QB=1 and at least 80% of the OMs expected to work at the time of the run are effectively working (former copper run classification);
- **QB=3**: the same requirements as QB=2, with baseline less than 120 kHz and burst fraction less than 0.4 (former silver run classification);

- **QB=4**: the same requirements as QB=3, with baseline less than 120 kHz and burst fraction less than 0.2 (former golden run classification).

For this analysis, all the runs with QB≥1 on the period December 2007 - December 2011 have been considered. With this selection, there are 9615 runs for a total livetime of 933.17 days, exploited for the following analysis and sensitivity estimation.

5.3 Preliminary cuts

Before starting with the analysis tools aiming to discriminate signal and background, it is necessary to clean the sample from all the events which suffer from a bad reconstruction or detector defects able to feign possible signal events. At the end of the quality cuts, an additional angular selection is performed, in order to maximize the probability to have ultra high energy signal and to minimize the surviving background.

5.3.1 Preliminary event selection

As already explained, in ANTARES the so-called L1 hits mainly used for analysis can be due to a time coincidence of two hits on a PMT in a time window smaller than 20 ns or a single having a charge greater than 3 p.e. For this analysis, in order to exclude at least a part of the false events due to optical background or detector artifacts (such as afterpulses), only L1 hits due to time coincidences have been taken into account.

Also, in order to analyze an event, it must contain a track reconstructed by both the strategies, AAFit and BBFit.

5.3.2 Event time structure

The time structure of the events must be well defined. As can be seen in Fig. 5.3, when a PMT is hit multiple times by a bunch of photons gives rise to a reliable time structure. So it has been decided that, to keep en event for further analysis, its number of PMTs touched by more than one hit should be at least greater than zero.

5.3.3 AAFit track quality cut

In order to face the difficulty of reconstruction for ultra high events, the AAFit strategy requests two cuts on its quality parameter, the quality of the

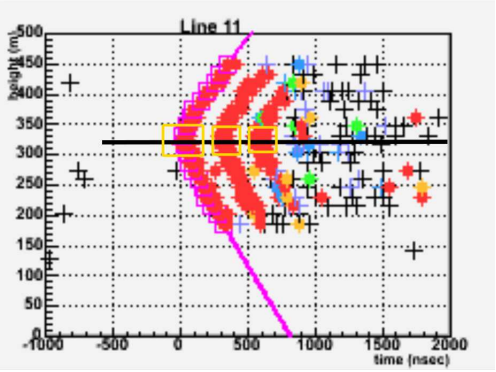

Figure 5.3: Event display from a MC ultra high energy event on a particular detector line. As can be seen, the same PMT is hit several time by different photon wavefronts, giving rise to a particular time structure which could be later exploited for the analysis.

track fit Λ and the angular error β. As can be see on the left of Fig. 5.4, the ultra high energy part of the signal has a peak near $\Lambda = -6.5$, because the large amount of hits produced in a ultra high energy event is difficult to manage for this reconstruction strategy. The distribution of β is shown in Fig. 5.5.

5.3.4 Agreement between the two reconstruction strategies

For ultra high energy events it may happen that the two reconstruction strategies give very different results in terms of zenith angle or track direction, even if their quality parameters are *per se* good. In order to have a consistency between the two strategies, a cut on the difference of the cosine of the zenith angles has been set, as shown in Fig. 5.6. This cut is just for the sanity of the angular selection, not intended to separate signal and background.

5.3.5 BBFit track quality cut

There are two main quality parameters, defined as χ^2 probabilities, in BBFit: the tchi2, which is the probability for an event to have a good fit as track, and bchi2, which is the same probability associated to a bright point.

Since the tchi2 parameter is not optimize to reconstruct ultra high energy events, it is mandatory to modify the variable with the aid of a quantity representative for this kind of events. The number of couples of floors in T2

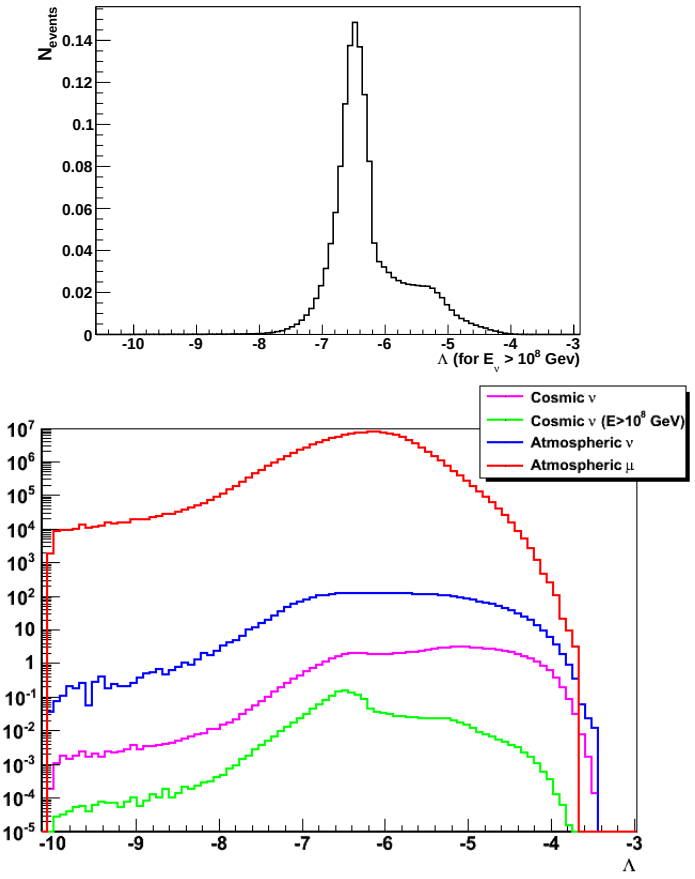

Figure 5.4: On top: distribution of Λ parameter for ultra high energy sample, i.e. neutrinos weighted with a Waxman-Bahcall flux model for energies greater than 10^8 GeV. On bottom: distribution of Λ parameter for the Monticello samples.

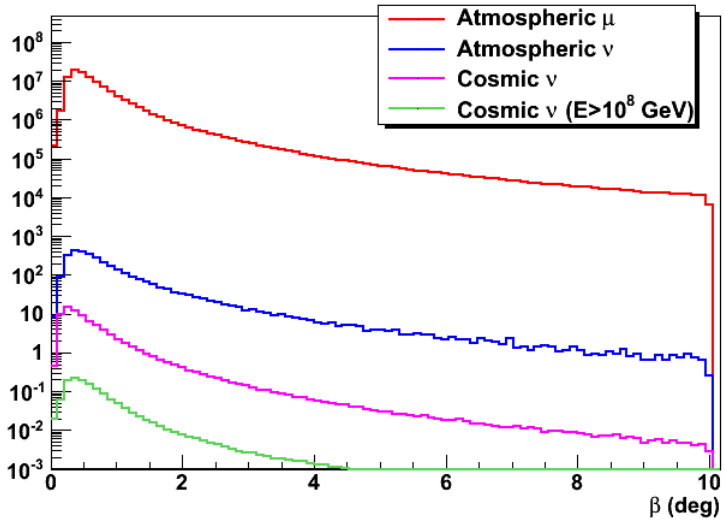

Figure 5.5: Distribution of β parameter for the Monte Carlo samples.

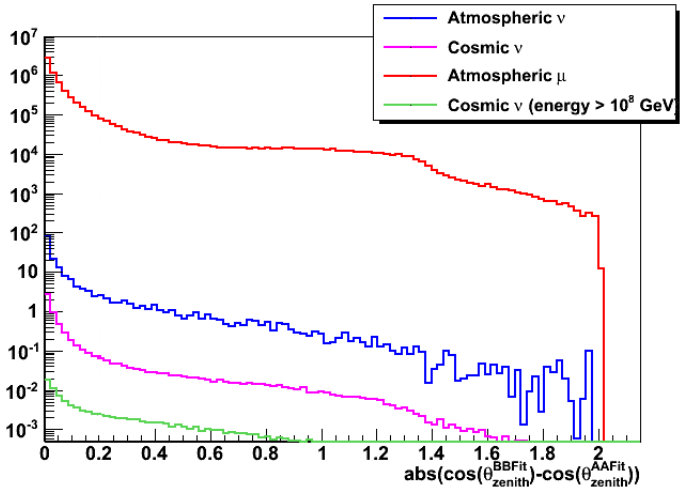

Figure 5.6: Distribution of the difference between the cosinus of the zenith angle, according to AAFit and BBFit.

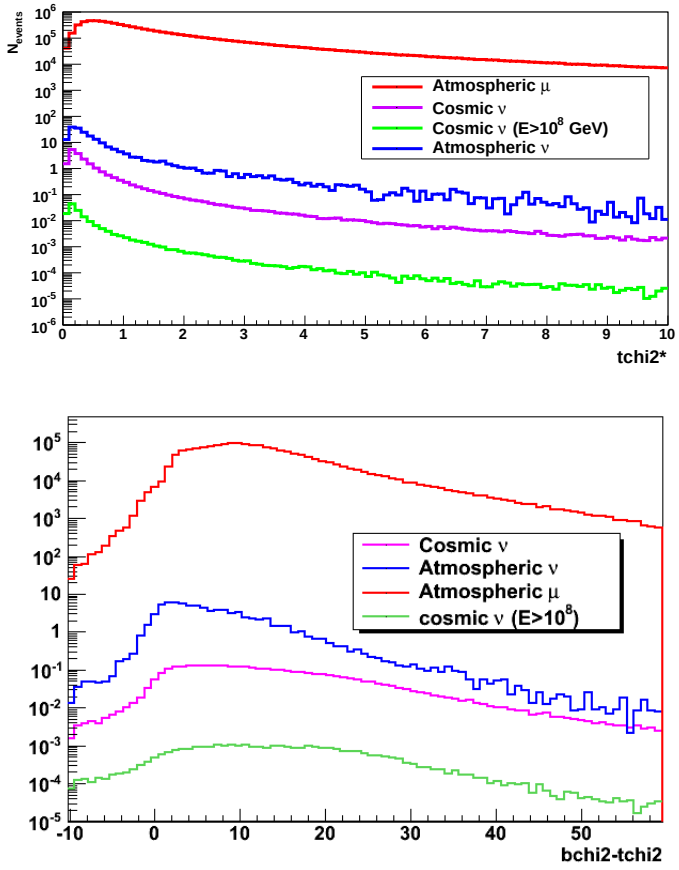

Figure 5.7: On top: distribution of tchi2* parameter for the Monte Carlo samples (in red the chosen analysis cut). On bottom: signal to noise ratio used to tune the cut, with only the ultra high energy events (energy greater than 10^8) used as signal (in red the chosen analysis cut).

status (both in a L1 status in a time window of 200 ns) has been exploited. This is the modified definition of tchi2*:

$$\text{tchi2}^* = \frac{\text{tchi2}}{(\text{floor\_T2} - 1) \cdot 0.5} \tag{5.1}$$

The distribution of this variable is in Fig. 5.7 on top.

The second cut concerning BBFit strategy is to set to reject the bright point. In order to prefer track-like topologies, a cut on the difference between bchi2 and tchi2 is chosen, as shown in Fig. 5.7 on bottom.

5.3.6 Angular selection

After the quality cuts, all the surviving events are selected by the angle of incidence.

Earth becomes opaque to neutrinos of energy greater than 10 PeV, so there is an angular sector of interest near the horizon. This zone has been chosen to reject the most muons as possible in the downgoing region, because even if they are reduced in number, their signature is very similar to a cosmic neutrino's one. The cut in the upgoing region is set to collect a part of the upgoing events before the atmospheric neutrino background becomes too important.

Since events near the horizon are difficult to reconstruct, in order to minimize the risk of taking into account misreconstructed tracks, it has been chosen to request that both the reconstruction strategies must have the zenith angle inside the chosen range. In Fig. 5.8 the distributions of the zenith angle according to the Monte Carlo truth, AAFit and BBFit.

5.4 Analysis technique

Even if the ANTARES collaboration has developed a certain number of algorithms for energy estimation, there is no reliable energy estimator reliable and tested over 10^8 GeV. A good technique to discriminate ultra high energy events is the exploitation of a set of variables (six in the present case), later combined in a single estimator. Each variable is representative of one aspect to describe an event inside ANTARES detector.

In this section the detailed list of variables will be analyzed. The best multivariate technique is then tested and applied to simulations, to estimate the sensitivity by model rejection factor technique.

5.4.1 List of variables

All the variables listed in this section have been calculated after the application of preliminary cuts detailed in Par. 5.3.

5.4.1.1 Number of hits in time coincidence

This is the most common variable, as it is just the number of total hits deposed in the instrumentation volume by an event. In this case, hits taken into account are the L1 due only to time coincidences.

This variable is strongly correlated to the number of photons emitted along a particle's track, giving a measurement of the event luminosity. This

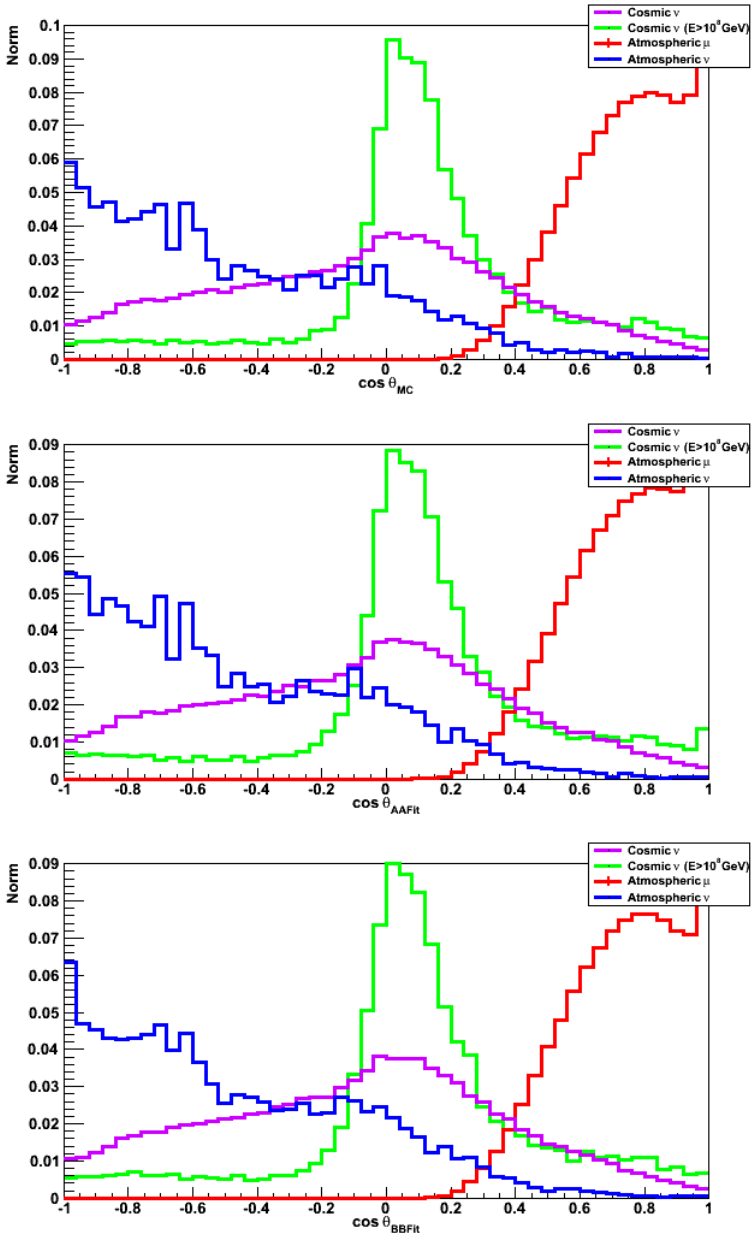

Figure 5.8: Distribution of the zenith angle according to Monte Carlo truth (top), AAFit (middle) and BBFit (bottom). On the Y axis the number of events is normalized at the integral.

variable has higher values for ultra high energy neutrinos, because of the amount of light produced in their events.

In order to compensate the loss of light for all the tracks passing nearby the detector, this variable is multiplied by a function of the distance of closest approach computed with respect to the center of gravity for the detector.

$$f(\text{dca}) = 1 + \frac{\text{dca}}{\langle \text{dca} \rangle} \tag{5.2}$$

The distance of closest approach is computed for the track reconstructed with AAFit and its mean is taken 100 m.

5.4.1.2 Number of PMTs with more than one hit

The number of PMTs touched by more than one hit is correlated to the spatial extension of an event. Moreover, it assure that the event has a time structure, as already said in the dedicated section. This variable has higher values for ultra high energy neutrinos because they produce more light along their trajectory, touching the same PMT several times.

Also atmospheric muons can have an important spatial extension, but being less energetic, they touch a PMT less times than the ultra high energy neutrinos.

Also for this variable, it is necessary to multiply the value by the function of the distance of closest approach in Eq. 5.2.

5.4.1.3 Number of neighbor floors in time coincidence (T2)

A couple of T2 floors consists of two adjacent floors touched at least by a L1 hit in a time window of 100 ns, as shown in Fig. 5.9.

This selection is not exclusive: the same floor can make part of two couples, with the two adjacent floors.

Also this variable is multiplied by the function in Eq. 5.2.

5.4.1.4 Inertia tensor

This technique considers each PMT i as a point in the space whose virtual mass A_i is the sum of the amplitudes of all the hits recorded by the PMT. The inertia tensor is defined as its analogue for classic mechanics:

$$I^{k,l} = \sum_{i=1}^{885} (A_i)^w \left[\delta^{k,l} \cdot (\mathbf{r})^2 - r_i^k \cdot r_i^l \right] \tag{5.3}$$

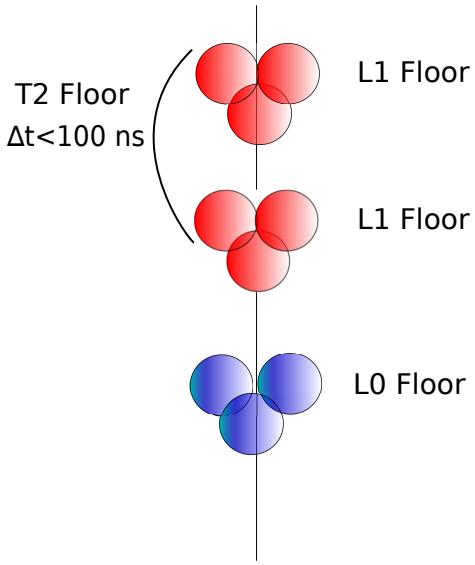

Figure 5.9: Scheme of a couple of T2 floors.

This tensor is computed in the reference system of the detector center of mass and the weight factor w can be defined by the user. In this analysis, knowing the potential ANTARES charge calibration problems, it is set to zero.

This technique, based on the position of all the PMTs which recorded hits, results in three eigenvalues ($e_1 > e_2 > e_3$) corresponding to the three main axis of the event (Fig. 5.3). The e_3 eigenvalue correspond to the eigenvector which approximates the track direction.

5.4.1.5 Dispersion of hit time weighted by charge

Hit time dispersion is the mean, calculated of the all the PMTs touched by the root mean square of the time distribution Δt weighted by the amplitude A:

$$S = \frac{1}{N_{\text{PMTs}}} \sum_{p=1}^{N_{\text{PMTs}}} \text{RMS}(A\Delta t) = \frac{1}{N_{\text{PMTs}}} \sum_{p=1}^{N_{\text{PMTs}}} \sqrt{\frac{1}{N_p} \sum_{k=1}^{N_p} \left[A_k(t_k - \overline{t_p})\right]^2} \quad (5.4)$$

N_p is the number of hit on every PMT and $\overline{t_p}$ is the mean time of the hits on every PMT. A_k and t_k are the time and the amplitude of the k hit. The sum is performed over all the PMTs which have recorded L1 hits. This kind of normalization allow to rely on the instrumented volume. In this way

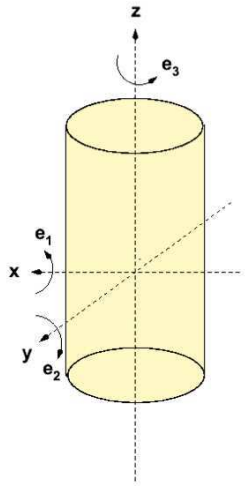

Figure 5.10: Schematic representation of inertia eigenvalues e_i, representing the inertial momentum with respect to the event's axis.

the spatial extension of the event is taken into account, along with the time extension.

The time dispersion is higher for ultra high energy neutrinos because they produce more hits inside the detector, resulting in a greater time residual distribution and thus a greater S.

5.4.1.6 Mean dead time

In an ultra high energy event lots of photons are created along the muon track and they will arrive as frontwave on the PMTs. It is possible that the two ARS are occupied, giving rise to a dead time of 250 ns during which the electronic is blind.

The mean dead time is defined as the mean value $\Delta t = |t_1 - t_2|$ on all the 885 PMTs for all the N_{pairs} pairs of hits of time t_1 and t_2 on the same PMT, in a time window greater than 50 ns:

$$\overline{d} = \frac{1}{N_{\text{double}}} \sum_{i=1}^{N_{\text{hits}}} \sum_{j>i}^{N_{\text{hits}}} \delta^{PM_i PM_j} |t_i - t_j| \tag{5.5}$$

It is a way to look for events with a well-defined time structure.

5.4.2 Multivariate analysis

The variables defined in the previous list are not use in the purpose of a classical analysis with sequential cuts, but in the aim of a multivariable analysis. Their different power of discrimination is used to male the analysis more efficient.

For this aim, ROOT software tools for multivariate analysis, TMVA, has been exploited [89]. This tool provides a ROOT-integrated environment for the processing, parallel evaluation and application of multivariate classification and regression. All its techniques belongs to the family of supervised learning algorithms. They make use of training events, for which the desired output is known, to determine the mapping function that either describes a decision boundary (classification) or an approximation of the underlying functional behavior defining the target value (regression). The software package contains an abstract, object-oriented implementations in C++/ROOT for each of these multivariate analysis, as well auxiliary tools such as parameters fitting and transformations. It provides training, testing and performances evaluation algorithms, along with visualization scripts.

Training and testing for all the methods is performed with an user-supplied data set, in form of ROOT trees or text files, where each event can have an individual weight. The true sample composition in these data sets must be supplied for each event. TMVA works in transparent factory mode to guarantee an unbiased comparison between MVA methods: they all see the same training and test data, and are evaluated following the same prescriptions within the same execution job.

A typical TMVA classification analysis consists of two independent phases: the training, where the multivariate methods are trained, tested and evaluated, and an application phase, where the chosen methods are applied to concrete classification problem they had been trained for.

In the training phase, the TMVA factory provides member functions to specify the training and testing data set, to register the discriminating input variables, and to book the multivariate methods. After, the factory calls for training, testing and evaluation of the booked MVA methods. Specific results files in XML format, called weights, are created after the training phase by each booked method.

The application of training results to a data set with unknown sample composition is the following step. The weight file provides for each of the methods full and consistent configuration according to the training setup and results. Within the event loop, the input variables are updated for each event, and the MVA response values are computed.

For this analysis the training sample chosen is 10000 events for signal and

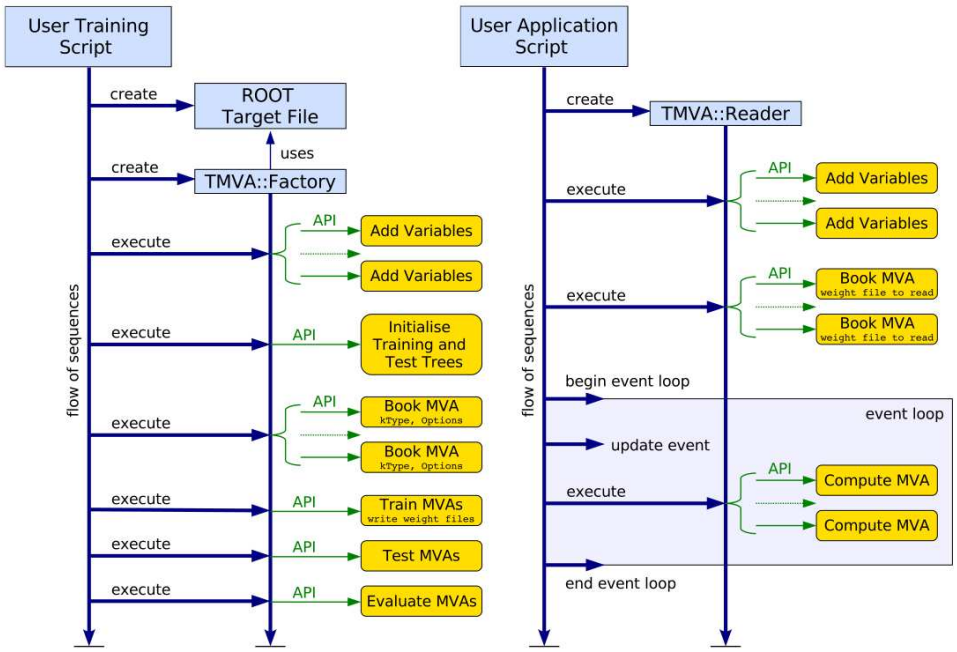

Figure 5.11: On the left, the flow of a typical TMVA training application. On the right, the flow of a typical analysis application.

backgrounds. The methods booked for estimation are two linear discriminant analysis (Fisher test and LD), a multidimensional likelihood and boosted decision trees. As shown in Fig. 5.12, the best method to use is the boosted decision trees.

5.4.2.1 Boosted decision trees

A decision tree (BDT) is a binary tree structured classifier, as can be seen in Fig. 5.13. Starting from the root node, a sequence of binary splits using the discriminating variable x_i is applied to data. Repeated left/right or yes/no decision are taken on a single variable at a time until a stop criterion is fulfilled. Each split uses the variable that at this node gives best separation between signal and background. The phase space is split this way into many regions that are eventually classified as signal or background, depending on the majority of training events that end up in the final leaf node.

There are different separation criteria that can be implemented in the growing of a boost decision tree, most of them symmetric with respect to the event class. All separation criteria have a maximum where the samples are fully mixed (at purity $p = 0.5$) and fall to zero when the sample consist of one event class only. For this analysis the chosen discrimination criterion is

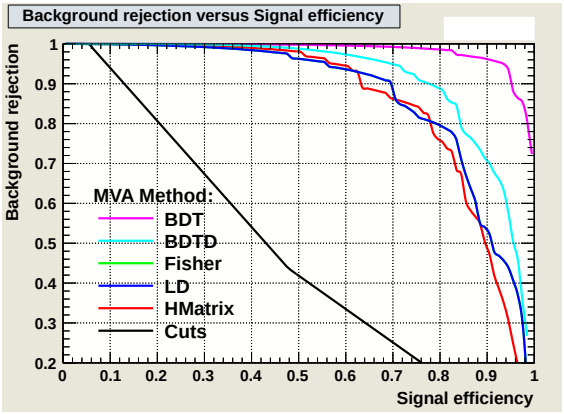

Figure 5.12: Signal efficiency versus background rejection for the booked methods in TMVA, applied to this particular analysis.

the so-called Gini index, defined by $p(1-p)$. Each event i is weighted by a factor W_i and the purity of the node is computed like:

$$p = \frac{\sum_s W_s}{\sum_s W_s + \sum_b W_b} \tag{5.6}$$

defined as the ratio between the sum of the weight of signal events in the node and the sum of all the weights of all the events present in that node. The purity $p = 0$ is reached when there are only background events in the sample, $p = 1$ if there are only signal events and $p = 0.5$ is they are equally mixed. For a node with n events, the Gini index is computed as the following:

$$\text{Gini} = \sum_{i=1}^{n} W_i p(1-p) \tag{5.7}$$

The method wants that the separation between the variables of different classes increases from a level to a deeper level of the tree.

The main problem of a single decision tree is the stability: a small change or fluctuation in the data can make a large difference in the classification. The boosting of a decision tree extends this concept from one tree to several trees which form a forest, solving the stability problem. The trees are derived from the same training ensemble by reweighting events, and are finally combined into a single classifier which is given by an average of the individual decision trees. Boosting stabilizes the response of the decision trees with respect to fluctuations in the training sample and is able to considerably enhance the performance with respect to a single tree.

After the training of a boost decision tree with a certain Monte Carlo sample, for each event i at each node depth there is a factor Y_i whose value

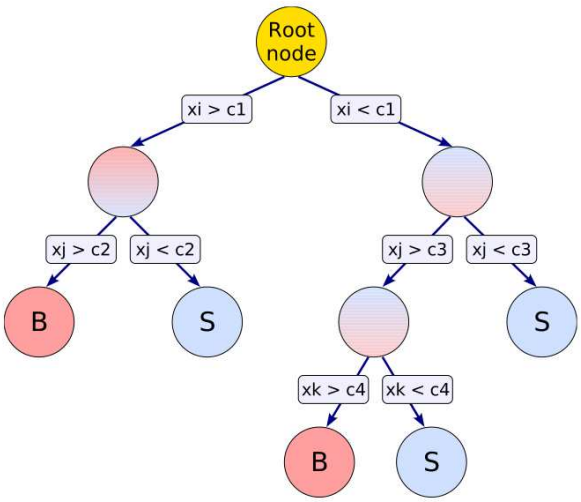

Figure 5.13: Schematic view of a decision tree. The leaf nodes at the bottom end of the tree are labeled S for signal and B for background depending on the majority of events that end up in the respective nodes.

is 1 is the event i is signal, -1 if it is background. Coming to an unknown sample, the boost decision tree overall decision for a tree m is summarized in the factor $T_m(x_i)$, which is 1 if the event is attributed to a signal leaf, -1 if it falls into the background leaf. The goal is to have $T_m(x_i) = Y_i$, otherwise the event is misclassified. If the event is misclassified, the method increase its weight:

$$W_i \to W_i \cdot e^{\alpha_m} \text{ with } \alpha_m = \beta \cdot \ln \frac{1 - err_m}{err_m} \tag{5.8}$$

where β is a constant and the function err_m is defined:

$$err_m = \frac{\sum_{T_m(x_i) \neq Y_i} W_i}{\sum W_i} \tag{5.9}$$

In this case, a new tree is built. At the end, the final boost decision tree variable is obtained summing over the trees:

$$T(x_i) = \sum_{m=1}^{N_{\text{tree}}} \alpha_m T_m(x_i) \tag{5.10}$$

5.4.2.2 Model rejection factor

This method is thought to optimize experimental cuts in order to place the strongest constraints, or upper limits, on theoretical signal models [90]. The

upper limit of a diffuse flux $\Phi(E)$ for a certain confidence level C.L. depends on the number of events observed $n_{\rm obs}$, on the number of expected background events $n_{\rm bg}$ and on the number of expected signal events $n_{\rm s}$, according to the ratio:

$$\Phi(E)_{CL} = \Phi(E)\frac{\mu_{CL}(n_{\rm obs}, n_{bg})}{n_{\rm s}} \tag{5.11}$$

where $\mu_{\rm CL}(n_{\rm obs}, n_{\rm bg})$ is the upper limit of Feldman-Cousins for a certain confidence level CL [91]. In order to avoid the any bias when setting the cut on th multivariate estimator, this choice must be done without any information about the data. Only Monte Carlo are used to calculate this average upper limit, under the hypothesis of no true signal ($n_s = 0$) and expected background n_b. This ratio depends only on the number of observed events, weighted according to their Poisson probability of occurrence, giving an upper limit as the following:

$$\overline{\mu}_{\rm CL}(n_{\rm bg}) = \sum_{n_{\rm obs}=0}^{\infty} \mu_{\rm CL}(n_{\rm obs}, n_{\rm bg})\frac{n_{\rm bg}^{n_{\rm obs}} e^{-n_{\rm bg}}}{n_{\rm obs}!} \tag{5.12}$$

This mean upper limit does not depend from expected background, obtained by Monte Carlo studies. The 90% confidence level sensitivity is defined as the following:

$$\overline{\Phi}(E)_{90\%} = \Phi(E) \cdot {\rm MRF} = \Phi(E) \cdot \frac{\overline{\mu}_{90\%}(n_{\rm bg})}{n_{\rm s}} \tag{5.13}$$

where MRF$= \overline{\mu}_{90\%}(n_{\rm bg})/n_{\rm s}$ is the so called model rejection factor. The MRF value represents the factor to be applied to the flux in order to have it observable on the detector of interest. Its computation on different cuts on a chosen variable allows also the optimization for the minimization selection. In the following this technique has been employed to choose the best cut on the multivariate estimator, for both the flux model investigated.

5.5 Optimization of the cuts

The cuts shown in Par. 5.3 must be optimized to have a good signal efficiency and background rejection. However, knowing the very weak signal expected for this kind of analysis, the best method to chose the most efficient cut is evaluating which sample can lead to the best model rejection factor. To have this result, for every cut at least three possible values have been taken into account.

- Number PMTs with ore than one hit: 1, 0;

- Λ: -6 (taken into account only in the Waxman-Bahcall analysis), -6.2, -6.6, -6.8, -7, -7.2, -7.4;
- β: 0.3°, 0.5°, 1°, 1.2°;
- reconstruction agreement: 0.15, 0.20, 0.25;
- tchi2*: 0.75, 1, 1.5;
- bchi2-tchi2: 1, 2, 3;
- lower limit of the angular selection (zenith angle): 75°, 79°, 81°, 83°;
- upper limit of the angular selection (zenith angle): 112°, 120°, 150°, 180°.

All the possible combinations are around 25000 and for each one of them the corresponding MRF factor have been computed. The process has run separately for Waxman-Bahcall and cosmogenic flux, in order to have two real optimizations.

In the majority of these cuts combinations the muons' sample ranges from few to few hundreds. This reduced number can be a problem when the model rejection factor minimization is applied: the absence of tail in the distribution of boost decision tree variable for muons could result in a too optimistic sensitivity estimation. For this reason a gaussian fit is performed over the muon distribution, in order to smooth it and extrapolate the tails (see Fig.5.14).

The combination chosen after this cut optimization is the one which has the smallest model rejection factor, along with a correct muon fit evaluation, to avoid all the bad muon's estimation which can lead to wrong minima.

For the atmospheric sample, during the training phase only the diffuse flux from Bartol model is used, because a prompt component spoils the signal recognition. In order to evaluate the background coming from prompt flux, the atmospheric neutrino events have been weighted with a sum of Bartol flux and Sarcevic flux when the weights coming from the multivariate technique are applied.

5.5.1 Analysis for Waxman-Bahcall flux

The cut combination with the best model rejection factor taking into account a signal weighted with Waxman-Bahcall flux is the following:

- Number PMTs with ore than one hit$>$ 0;

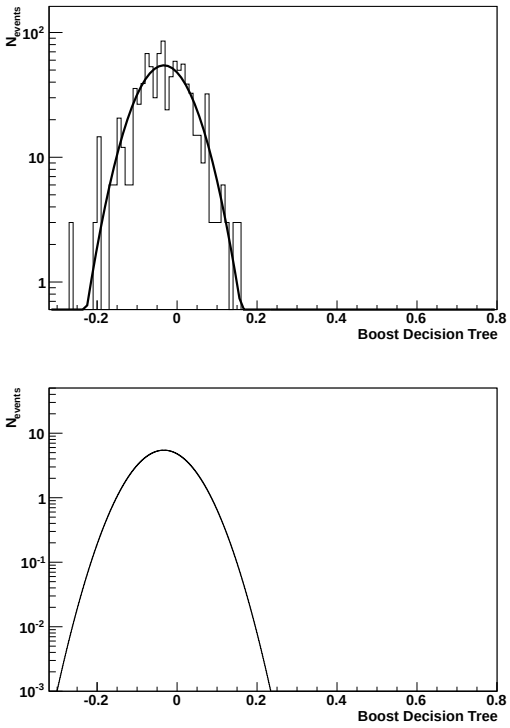

Figure 5.14: On the left: the histogram of muon background (with an appropriate binning) fitted with a gaussian function in order to evaluate the tails. On the right: the histogram derived from the fit, used to compute the model rejection factor.

- $\Lambda >$ -6.2;
- $\beta < 0.3°$;
- reconstruction agreement$<$ 0.20;
- tchi2* $<$ 1;
- bchi2-tchi2$>$ 3;
- angular selection (zenith angle): 81°-150°;

In the Tab. 5.1 there all the effects of the sequential cuts are summarized, scaling over a year of data taking.

Samples	L1	$N_{\mathrm{PMT}} > 0$	$\Lambda > -6.2$	$\beta < 0.3°$	Cons.<0.20	t$\chi^{2*} < 1$	bχ^2-tχ^2 >3	Angular selection
Cosmic ν	150.8	78.671	72.347	21.207	20.385	17.553	17.387	10.9
UHE ν	1.56	1.46	1.07	0.197	0.154	0.132	0.130	0.078
Atmo ν	3414	2947.5	2319	245.61	217.59	175.47	168.29	100
Std μ	$4.87{\cdot}10^8$	$1.19{\cdot}10^8$	$8.97{\cdot}10^7$	$9.96{\cdot}10^6$	$8.97{\cdot}10^6$	$3.42{\cdot}10^6$	$3.40{\cdot}10^6$	60
HM μ	$2.40{\cdot}10^7$	$1.28{\cdot}10^7$	$1.09{\cdot}10^7$	$1.41{\cdot}10^6$	$1.33{\cdot}10^6$	$5.76{\cdot}10^5$	$5.75{\cdot}10^5$	34.7

Table 5.1: Number of events surviving the different analysis pre-cuts, computed over a period of 933 days. Cosmic neutrinos are weighted with Waxman-Bahcall flux ($E^2\Phi = 4.5 \times 10^{-8}$ GeV m^{-2}s^{-1}sr^{-1}). The line labeled as UHE-ν refers to the simulation in the energy range $10^8 - 10^{10}$ GeV, the HM-μ to the special MUPAGE production with high multiplicity.

Samples	L1	$N_{\mathrm{PMT}} > 1$	$\Lambda > -7.4$	$\beta < 0.5°$	Cons.<0.20	t$\chi^{2*} < 1.5$	bχ^2-tχ^2 >3	Angular selection
Cosmic ν	4.04	2.88	2.87	1.64	1.41	1.22	1.15	0.64
UHE ν	0.4106	0.362	0.358	0.151	0.096	0.076	0.069	0.042
Atmo ν	3414	2947.5	2881.7	945.04	666.91	512.71	378.17	266.20
Std μ	$4.87{\cdot}10^8$	$1.19{\cdot}10^8$	$1.15{\cdot}10^8$	$4.43{\cdot}10^7$	$3.55{\cdot}10^7$	$1.63{\cdot}10^7$	$1.49{\cdot}10^7$	837
HM μ	$2.40{\cdot}10^7$	$1.28{\cdot}10^7$	$1.26{\cdot}10^7$	$5.60{\cdot}10^e$	$5.00{\cdot}10^e$	$2.67{\cdot}10^e$	$2.54{\cdot}10^e$	141

Table 5.2: Number of events surviving the different analysis pre-cuts, computed over a period of 933 days. Cosmic neutrinos are weighted with cosmogenic flux [35]. The line labeled as UHE-ν refers to the simulation in the energy range $10^8 - 10^{10}$ GeV, the HM-μ to the special MUPAGE production with high multiplicity.

After the application of the previous set of cuts, the simulation is used to train the multivariate analysis, in particular the technique of boost decision tree (Fig. 5.15 at the top). In order to set the cut for this analysis method, the model rejection factor has been employed, as can be seen in the bottom of Fig. 5.15. Scaling over a year of data taking:

$$\text{on one year: MRF} = 1.85 \text{ corresponding to bdt} > 0.195 \tag{5.14}$$

Over a year of data taking, this cut results in a certain number of events for signal and background:

- 1.43 cosmic neutrinos from Waxman-Bahcall flux ($E^2\Phi = 4.5 \times 10^{-8}$ GeV $\text{m}^{-2}\text{s}^{-1}\text{sr}^{-1}$);
- 0.14 atmospheric neutrinos (Bartol model for diffuse component and Sarcevic model for prompt component);
- no atmospheric muons;
- 0.10 atmospheric muons coming from the fit extrapolation.

The absence of muons in the final sample is important, because even a single event can spoil the value of the model rejection factor. This effect is produced because these muons are very difficult to eliminate, having a topology very similar to the one of an ultra high energy neutrino.

Taking into account the whole livetime of the simulations of 933 days of data taking, the model rejection factor has been computed:

$$\text{on 933 days: MRF} = 0.80 \text{ corresponding to bdt} > 0.195 \tag{5.15}$$

obtaining these events after the cut:

- 3.66 cosmic neutrinos from Waxman-Bahcall flux ($E^2\Phi = 4.5 \times 10^{-8}$ GeV $\text{m}^{-2}\text{s}^{-1}\text{sr}^{-1}$);
- 0.33 atmospheric neutrinos (Bartol model for diffuse component and Sarcevic model for prompt component);
- no atmospheric muons;
- 0.27 atmospheric muons coming from the fit extrapolation.

With the current events obtained after the model rejection factor cut, the energy range covered at 90% is from 56 TeV to 28 PeV, as can be seen in Fig. 5.16.

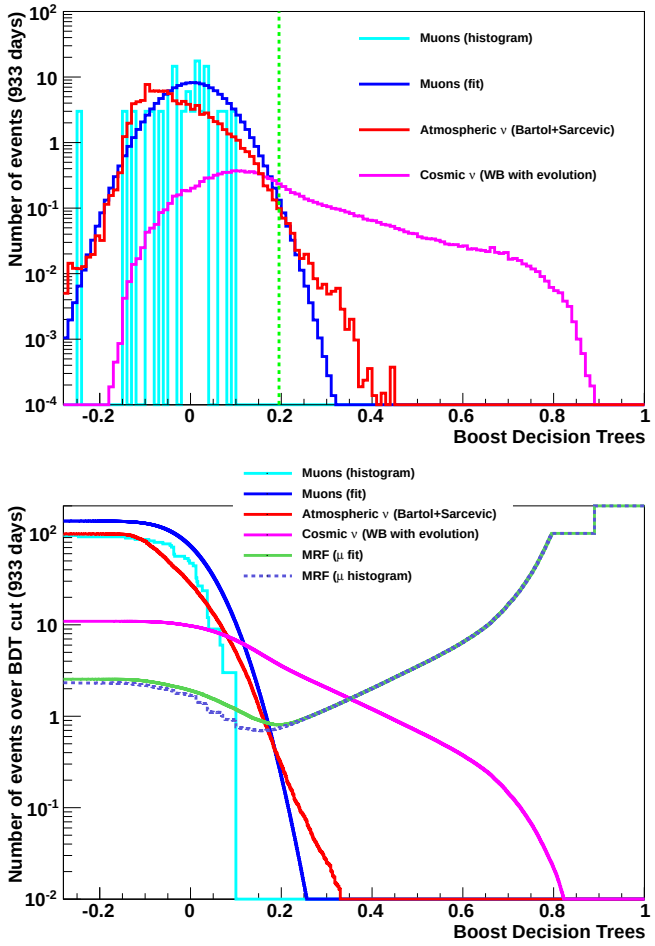

Figure 5.15: On top: application of the boost decision trees technique on the three Monte Carlo samples, with the signal weighted with Waxman-Bahcall flux. The distribution of muons according to fit extrapolation is also shown. The green line represent the cut set by model rejection factor. On bottom: distribution of the boost decision trees value for the three samples (signal weighted with Waxman-Bahcall flux with evolution), plus the fit performed for the muons, given in cumulative distribution. Superimposed, the fit for the MRF computer over 933 days of livetime, in case of muon fit and muon histogram.

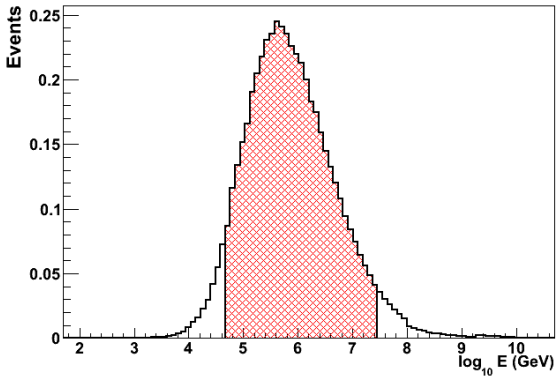

Figure 5.16: Energy of primary neutrinos survived after the application of the cut on boost decision trees, when weighted with a Waxman-Bahcall flux. The area in red represents the 90% of the signal.

5.5.2 Analysis for cosmogenic flux

The cut combination with the best model rejection factor taking into account a signal weighted with cosmogenic flux is the following:

- Number PMTs with ore than one hit: 1;
- $\Lambda >$ -7.4;
- $\beta < 0.5°$;
- reconstruction agreement$<$ 0.20;
- tchi2* $<$ 1.5;
- bchi2-tchi2$>$ 3;
- angular selection (zenith angle): 81°-150°;

In table Tab. 5.2 the effects of the different pre-cuts are shown, on the different samples.

The application of the Boost Decision Trees algorithm to the whole Monte Carlo sample is presented in Fig. 5.17. The cut on this variable has been estimated via the model rejection factor (Fig. 5.17 on bottom shows rejection factor plot, in the case of muon fit and muon histogram). Taking into account a year of data taking, the model rejection factor reports:

$$\text{on one year: MRF} = 21.4 \text{ corresponding to bdt} > 0.197 \tag{5.16}$$

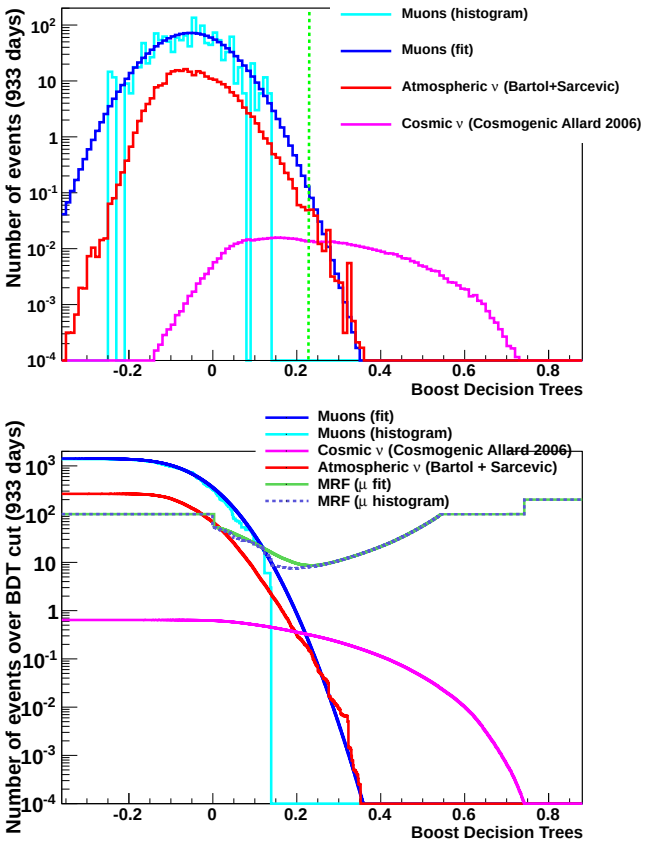

Figure 5.17: On top: application of the boost decision tree technique on the three Monte Carlo samples, with the signal weighted with the cosmogenic flux. The dotted line represents the cut set by model rejection factor. On bottom: distribution of the boost decision trees value for the three samples (signal weighted with cosmogenic flux), plus the fit performed for the muons, given in cumulative distribution. Superimposed, the fit for the MRF computer over 933 days of livetime, in case of muon fit and muon histogram.

After this final cut, scaling over a year we can expect the following number of events:

- 0.12 cosmic neutrinos from cosmogenic flux;
- 0.06 atmospheric neutrinos (Bartol model for diffuse component and Sarcevic model for prompt component);
- no atmospheric muons;
- 0.08 muons from fit extrapolation.

On the whole simulation period, for a total data taking time of 933 days, the model rejection factor has been recomputed:

$$\text{on 933 days: MRF} = 8.6 \text{ corresponding to bdt} > 0.229 \tag{5.17}$$

On this livetime the expected number of events surviving the cut:

- 0.32 cosmogenic neutrinos from cosmogenic flux;
- 0.15 atmospheric neutrinos (Bartol model for diffuse component and Sarcevic model for prompt component);
- no atmospheric muons;
- 0.21 muons from fit extrapolation.

With the current events obtained after the model rejection factor cut, the energy range covered at 90% is from 562 TeV to 139 PeV, as can be seen in Fig. 5.18.

5.5.3 ANTARES sensitivity

At the end of the analysis chain, the sensitivity for both the flux models has been estimated. It is computed as the product between the model rejection factor and the flux value. In Fig. 5.19 all the sensitivities are summarized, along with the reference fluxes from models.

For Waxman-Bahcall flux, the sensitivity is estimated:

$$E^2\Phi < 3.6 \times 10^{-8} \text{ GeV m}^{-2}\text{s}^{-1}\text{sr}^{-1} \tag{5.18}$$

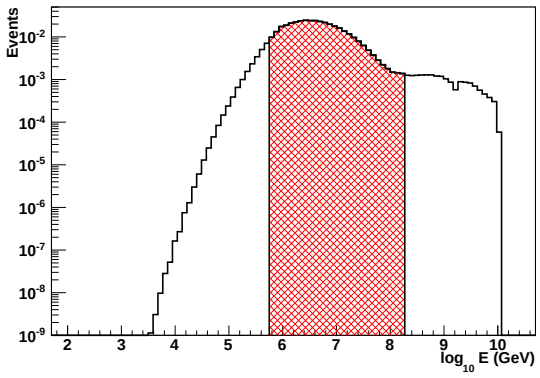

Figure 5.18: Energy of primary neutrinos survived after the application of the cut on boost decision trees, when weighted with a cosmogenic flux. The area in red represents the 90% of the signal.

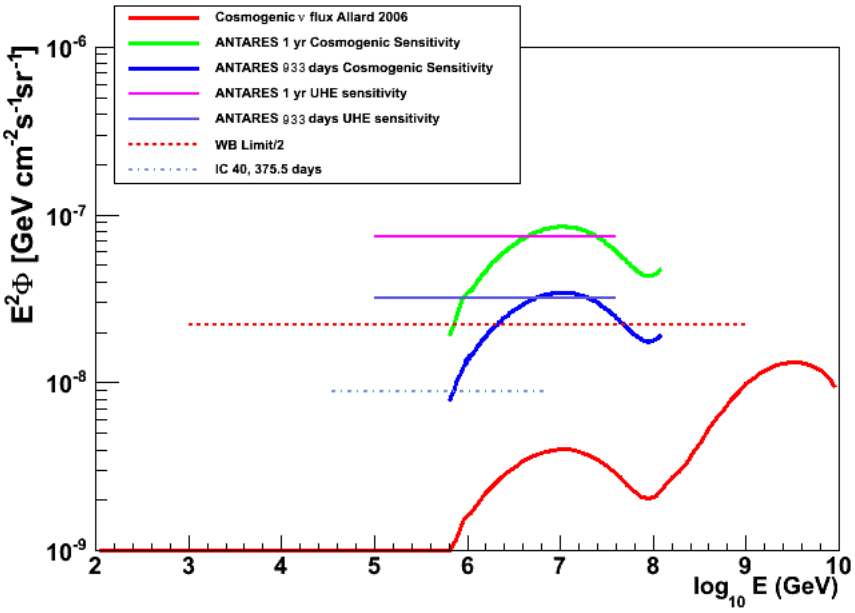

Figure 5.19: ANTARES sensitivity for this analysis, in the case of Waxman-Bahcall and cosmogenic flux for one year and 933 days of data taking. The reference fluxes are shown. For reference, IceCube sensitivity is reported. All the sensitivity are shown as $\nu_\mu + \overline{\nu}_\mu$.

Chapter 6

Application to data and results

The analysis chain described in the previous section has to be applied to real ANTARES data in order to give an upper limit for the fluxes of interest. The same data quality selection chooses the runs to be analyzed, for a total of 933 days of data taking. This period does not take into account some pathological runs, such as sparking runs or runs which have resulted to be problematic, as explained in the following.

6.1 Sparking optical modules

When analyzing ANTARES data, there is a severe detector defect which could feign astrophysical signal (see Fig. 6.1 and Fig.6.2 to compare the topologies of a problematic run and an ultra high energy event generated by Monte Carlo simulations): the phenomenon of sparking optical modules. Sparking OMs are due to some Antares photomultipliers which suffer from an effect of high voltage surges that cause the photomultiplier to spark [88]. A run containing such events is called a sparking run and poses some problems for the following physical analysis, being it able to feign a high energy neutrino event. So it is mandatory to identify the sparking runs, in order to exclude them from the analysis dataset, and also the optical module which originates the scintillation.

Sometimes this kind of runs is identified during the data taking, if the shift crew in charge of the detector is able to find them. However, normally a sparking runs is not identified as one until the physical analysis stage. The problem of conceiving a sparking identification algorithm is well known in ANTARES collaboration. A method based on the shower reconstruction has been already proposed and exploited. It relies on the localization of the shower's vertex: if it is quite near a photomultiplier, then the event is

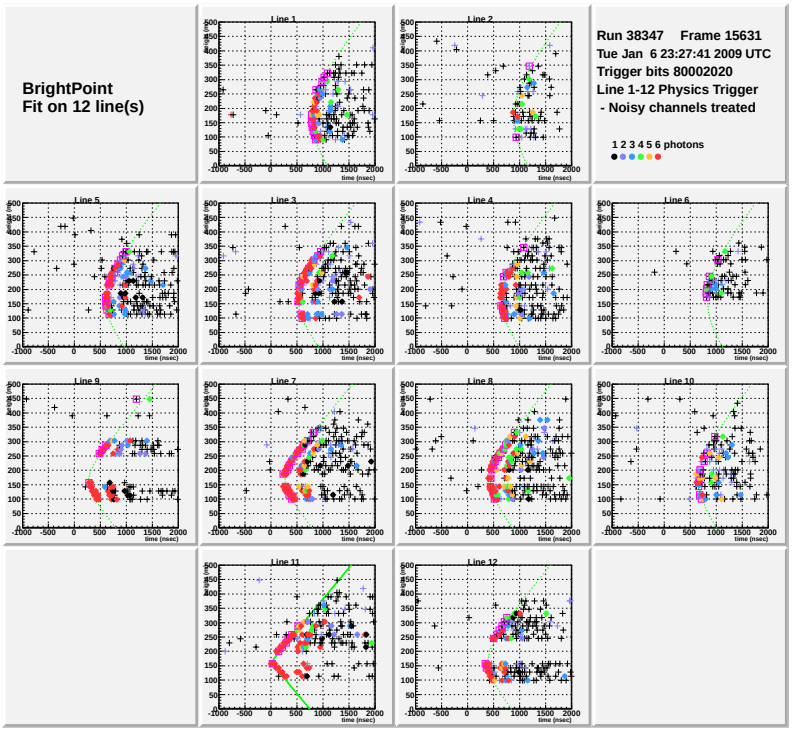

Figure 6.1: Event display of a sparking run. In this case it is possible to see the amount of light produced by the scintillation phenomenon. The reconstruction strategy identifies it as a bright point, with the vertex located inside the detector, near the instrumentation lines.

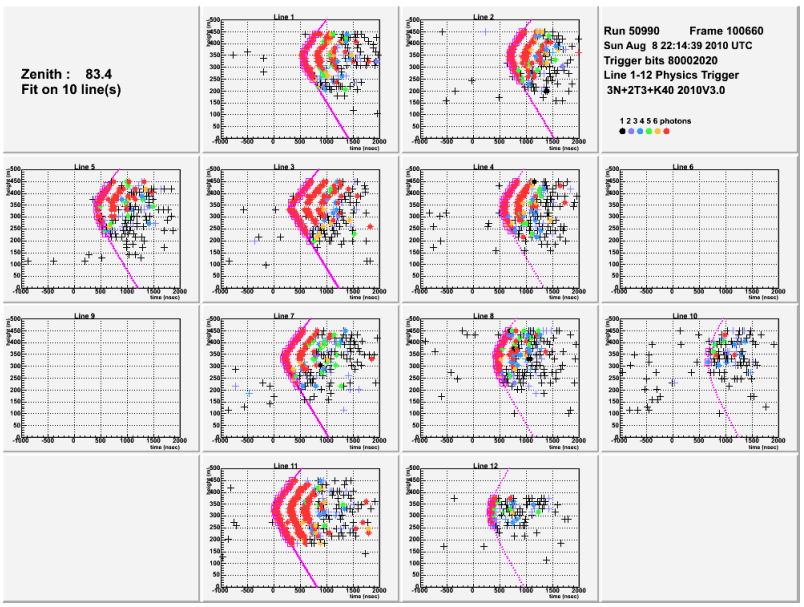

Figure 6.2: Event display of ultra high energy neutrino event, taken form the Monte Carlo simulation sample.

identified as sparking. However, the algorithm is not able to identify precisely the OM, knowing the distance computation is more precise in Z than in the plane X-Y, making it reliable for the floor identification but for the optical module precisely. It was mandatory to develop an algorithm able to identify at the same time the run and the OM responsible of the scintillation, starting from the simplest quantities and independent from track reconstruction.

6.1.1 Run Identification

A sparking optical module produces lot of light in the detector, so a cut on the number of hits is a good estimator to discriminate a candidate sparking run. Considering only L1 hits, without taking into account hits form the galactic center trigger, an event is considered a sparking candidate if it has more than 100 hits. This kind of precut identifies a possible sparking event and reject all the other, with a gain on CPU time.

6.1.2 Optical module Identification

In order to identify the optical module candidate for the sparking origin, a series of three preliminary cuts is applied, in order to clean up the event from spurious hits:

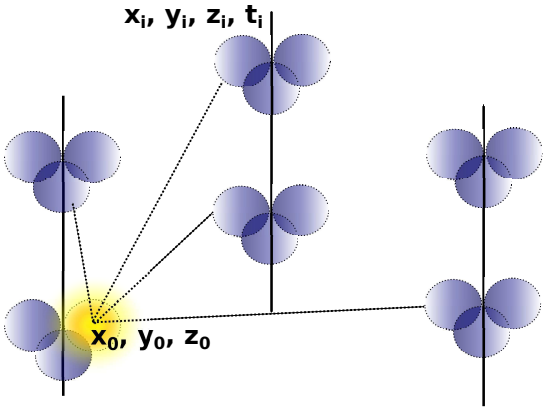

Figure 6.3: Schematic view of the time residual computation starting from a sparking optical module.

- each hit must have a charge greater than 5 p.e. in order to not take into account the photons due to secondary ionization from muonic showers;
- all the hits must be in the zone in front of the photomultiplier, under the hypothesis that a sparking OM emits only in the right direction;
- the hits taken into account must be in a spherical shell of radii between 20 and 200 meters all around the candidate OM: they should be in a different floor and not exceed the detector size.

For each event with more than 100 hits, the time residual distribution is studied. Time residuals are computed in this way: taking each optical module as reference, the difference between the hit arrival time on the optical module and the distance between the OM recording the hit and the optical module reference, as shown in Fig. 6.3:

$$\text{res} = t_i - \frac{\sqrt{(x_i - x_0)^2 - (y_i - y_0)^2 - (z_i - z_0)^2}}{v_g}$$

where $\mathbf{x}_i$ are the coordinates of the optical module recording the hit, t_i is the arrival time of the hits, $\mathbf{x}_0$ the ones of the optical module reference and v_g is the group velocity.

In this way, a time residual distribution for every OM is obtained. The candidate sparking optical module is the one corresponding to the distribution with time smallest σ, after a cleaning up of all the hits exceeding the 3σ.

For each sparking event, the candidate sparking optical module is identified and an additional cut is applied: the event must have more than 30

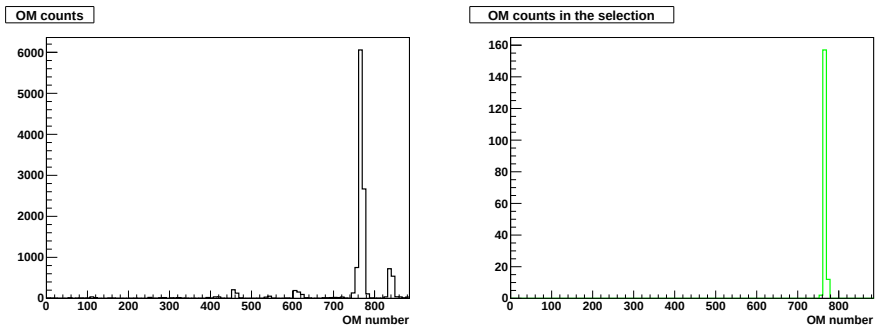

Figure 6.4: Distribution of the optical modules with the minimum σ for the sparking run 38351. On the left the peak representing the sparking OM is emphasized after the cut on σ and number of hits.

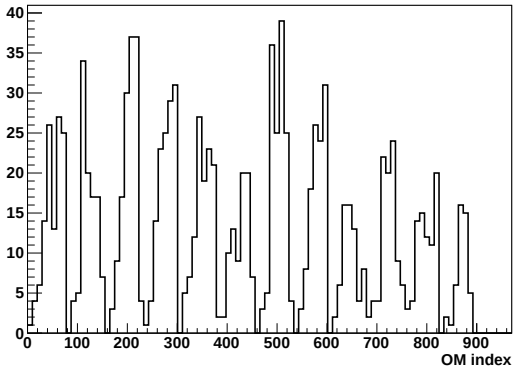

Figure 6.5: Distribution of the optical modules with the minimum σ for a set of genuine non-sparking runs, taking as reference for the χ^2 computation.

hits after the cleaning up and a σ smaller than 125 ns. In this way it is possible to identify a single sparking event in a run. At the end, the OM distribution is traced for the whole run. In this way it is possible to observe a peak corresponding to the sparking optical module, as seen in Fig. 6.4.

If there is no candidate peak but still some event with small σ has been detected, the optical modules distribution for the run is compared with the same plot for a set of non-sparking runs (Fig. 6.5). The χ^2 for this comparison is calculated and if the χ^2-probability is less than 1%, the run is considered sparking.

6.1.3 Treatment of the sparking runs

In the ideal case, when a sparking event is identified, it should be removed from the analysis sample, keeping all the other events from the same run. However, this procedure is rather dangerous, because of some events which could be particularly difficult to detect as sparking. Since the identification of the single could fail, the safest way to treat the sparking runs is to remove the whole suspected run from the data sample. An even more severe criterion to be really sure that there are no surviving sparking events in the sample is to remove also the previous and the following run with respect to the one where the sparking phenomenon has been identified, because of some tails of the scintillation hard to identify.

It is also interesting to verify in ANTARES' elog if the optical module responsible of the sparking phenomenon has been switched off (dead state) or not.

6.2 Analysis of the data sample

In this section the analysis chain defined in the previous chapter is applied to the whole data sample. The quality selection for this sample is the same as the one for Monte Carlo, illustrated in Par. 5.2. The two different procedures has been applied separately, for the search for Waxman-Bahcall (results in Tab. 6.1) or cosmogenic signal (results in Tab. 6.2).

Samples	L1	$N_{\mathrm{PMT}} > 0$	$\Lambda > -6.2$	$\beta < 0.3°$	Cons.< 0.20	t$\chi^{2*} < 1$	bχ^2-tχ^2 >3	Angular selection
Cosmic ν	150.8	78.671	72.347	21.207	20.385	17.553	17.387	10.9
UHE ν	1.56	1.46	1.07	0.197	0.154	0.132	0.130	0.078
Atmo ν	3414	2947.5	2319	245.61	217.59	175.47	168.29	100
Std μ	$4.87{\cdot}10^8$	$1.19{\cdot}10^8$	$8.97{\cdot}10^7$	$9.96{\cdot}10^6$	$8.97{\cdot}10^6$	$3.42{\cdot}10^6$	$3.40{\cdot}10^6$	60
HM μ	$2.40{\cdot}10^7$	$1.27{\cdot}10^7$	$1.09{\cdot}10^7$	$1.41{\cdot}10^6$	$1.33{\cdot}10^6$	$5.76{\cdot}10^5$	$5.75{\cdot}10^5$	34.7
Data	$5.78{\cdot}10^8$	$1.40{\cdot}10^8$	$1.02{\cdot}10^8$	$1.21{\cdot}10^7$	$1.06{\cdot}10^7$	$3.85{\cdot}10^6$	$3.83{\cdot}10^6$	164

Table 6.1: Number of events surviving the different analysis pre-cuts, computed over a period of 933 days. Cosmic neutrinos are weighted with Waxman-Bahcall flux. The line labeled as UHE-ν refers to the simulation in the energy range $10^8 - 10^{10}$ GeV, the HM-μ to the special MUPAGE production with high multiplicity.

Samples	L1	$N_{\mathrm{PMT}} > 1$	$\Lambda > -7.4$	$\beta < 0.5°$	Cons.< 0.20	t$\chi^{2*} < 1.5$	bχ^2-tχ^2 >2	Angular selection
Cosmic ν	4.04	2.88	2.87	1.64	1.41	1.22	1.15	0.64
UHE ν	0.4106	0.362	0.358	0.151	0.096	0.076	0.069	0.042
Atmo ν	3414	2947.5	2881.7	945.04	666.91	512.71	378.17	266.20
Std μ	$4.87{\cdot}10^8$	$1.19{\cdot}10^8$	$1.15{\cdot}10^8$	$4.43{\cdot}10^7$	$3.55{\cdot}10^7$	$1.63{\cdot}10^7$	$1.49{\cdot}10^7$	837
HM μ	$2.40{\cdot}10^7$	$1.28{\cdot}10^7$	$1.26{\cdot}10^7$	$5.60{\cdot}10^e$	$5.00{\cdot}10^e$	$2.67{\cdot}10^e$	$2.54{\cdot}10^e$	141
Data	$5.76{\cdot}10^8$	$1.40{\cdot}10^8$	$1.36{\cdot}10^8$	$5.33{\cdot}10^7$	$4.04{\cdot}10^7$	$1.74{\cdot}10^7$	$1.53{\cdot}10^7$	1049

Table 6.2: Number of events surviving the different analysis pre-cuts, computed over a period of 933 days. Cosmic neutrinos are weighted with cosmogenic flux [35]. The line labeled as UHE-ν refers to the simulation in the energy range $10^8 - 10^{10}$ GeV, the HM-μ to the special MUPAGE production with high multiplicity.

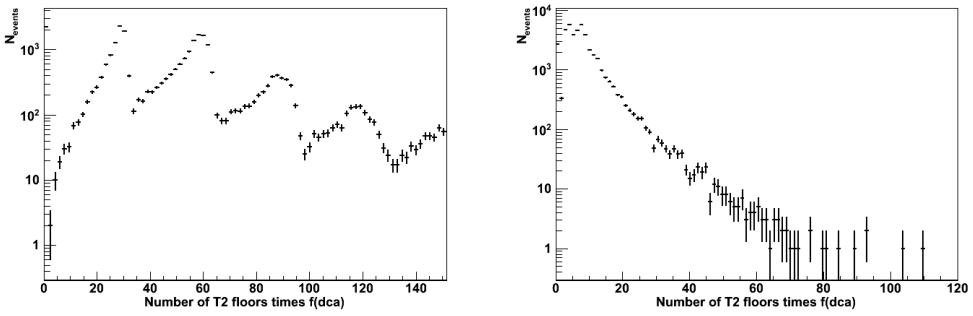

Figure 6.6: The plot of the variable number T2 floors for the period of the marine campaign (34420) on the left and another from a standard period (34470) on the right. The slope of the variable for run 34420 is spoiled by the bad computation of the distance of closest approach.

6.2.1 Problematic runs

When analyzing the sample and comparing it with the Monte Carlo simulation, a strange behavior has been recorded. When comparing the variables multiplied by the function of the distance of closest approach, such as the number of T2 floors (Fig. 6.6) and number of PMT recording more than one hit (Fig. 6.7), a bump is observed. This problem concerns a run in particular, the 34420 from May 2008, classified as QB=3. It is interesting to note that in this particular period a sea operation has been performed to connect lines 11 and 12.

As can be seen in Fig. 6.8, the distribution of the distance of closest approach for this run is completely false, if compared to the one of a non-problematic run. The problem concerns the detector geometry, which affects the reconstruction strategy and thus the computation of the distance of closest approach with respect to the detector center.

For the physical analysis, this run has been removed from the sample, along with all the runs of the period of the sea campaign.

6.2.2 Data/Monte Carlo comparisons

In this section the agreement between data and simulations is evaluated, in order to verify if they match i.e. if physical data are well reproduced during the simulation process. Different stages are presented, in order to show the goodness of the cuts, which improve the agreement. For the comparisons, the analysis chain for cosmologic flux is presented. The one for Waxman-Bahcall flux is reported in Appendix B.

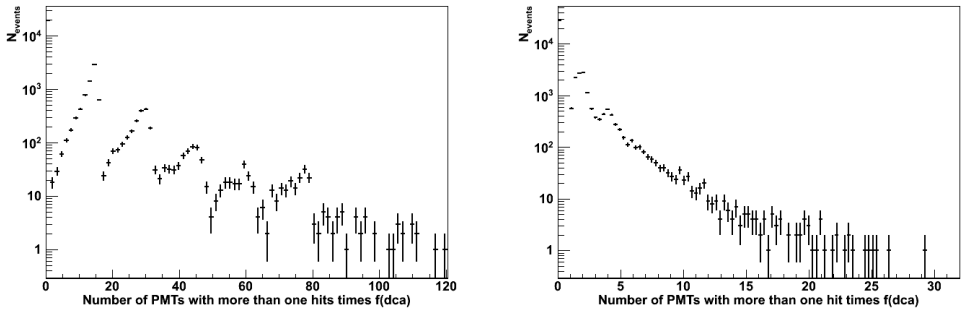

Figure 6.7: The plot of the variable number of PMTs with more than one hit for the period of the marine campaign (34420) on the left and another from a standard period (34470) on the right. The slope of the variable for run 34420 is spoiled by the bad computation of the distance of closest approach.

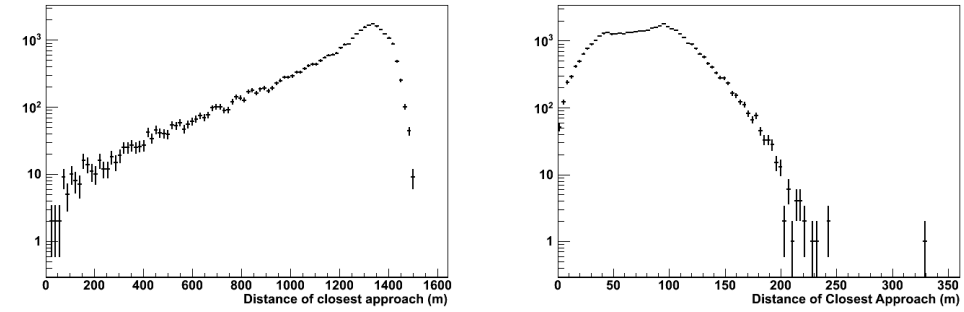

Figure 6.8: The plot of the distance of closest approach for the period of the marine campaign (34420) on the left and another from a standard period (34470) on the right. As it can be observed, for the marine campaign the computation of the DCA is completely wrong, maybe due to a bad AAFit reconstruction or a problem in the geometry. No cut on track quality has been applied.

6.2.2.1 Comparisons of the cut variables

Before going on comparing the variable exploited in the multivariate analysis, it is interesting to look at the agreement for the quality parameters used to clean the sample from pathological events (listed in 5.3). These variables are presented each one before the cut of interest. In this section, the chain used for cosmogenic flux is presented, while the one dedicated to Waxman-Bahcall flux is reported in Appendix B.

- Λ (AAFit quality parameter) (Fig. 6.9, left): data and Monte Carlo are in a good agreement, reproducing quite the same slope;
- β (AAFit quality parameter) (Fig. 6.9, center): globally the agreement between data and simulation is good;
- Reconstruction agreement (Fig. 6.9, right): data and Monte Carlo are compatible, showing an acceptable agreement on the whole range;
- tchi2* (BBFit quality parameter) (Fig. 6.10, left): the compatibility between data and Monte Carlo is kept, with the two distributions having the same slope;
- bchi2-tchi2 (BBFit quality parameter) (Fig. 6.10, center): the agreement between data and Monte Carlo is globally good, with compatible slopes;
- Zenith angle (according to AAFit reconstruction) (Fig. 6.10, right): for this plot, it necessary to consider the sum of background components, in order to evaluate the neutrino contribution in the upgoing region. The agreement is still good, even if the plot is scattering in the upgoing region, due to the low statistic.

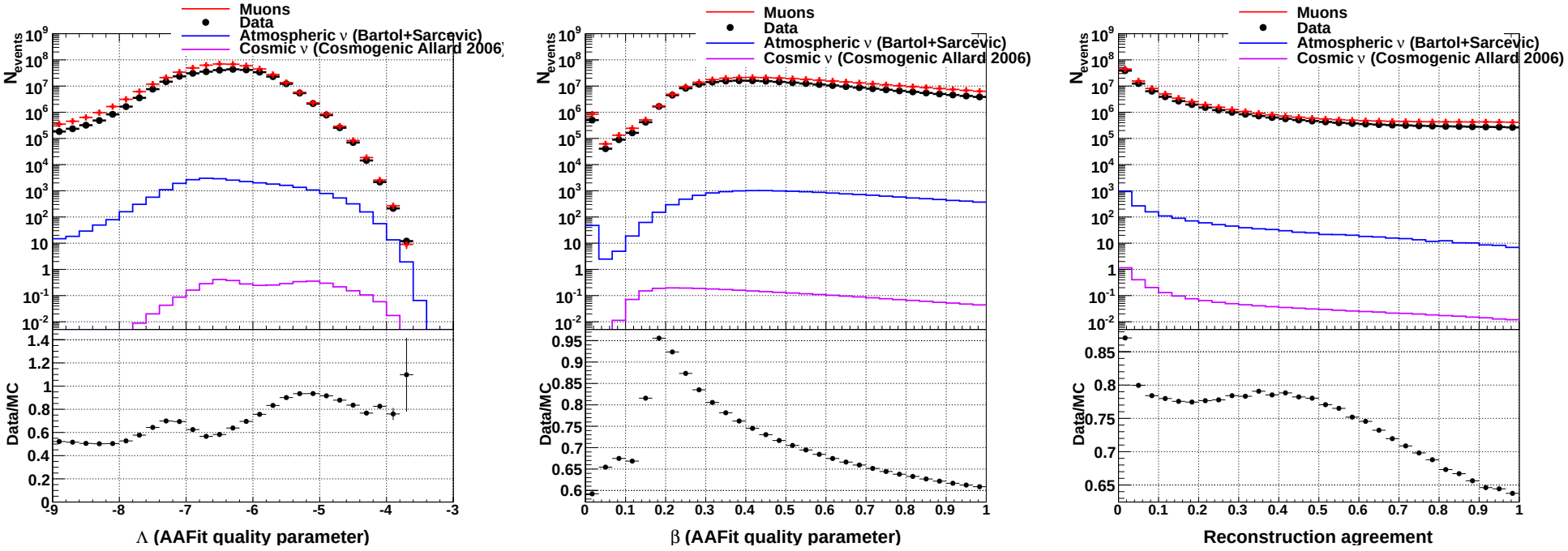

Figure 6.9: **Left:** Λ: data and Monte Carlo are in a good agreement, reproducing quite the same slope. **Center**: β: globally the agreement between data and simulation is good. **Right**: reconstruction agreement: data and Monte Carlo are compatible, showing an acceptable agreement on the whole range.

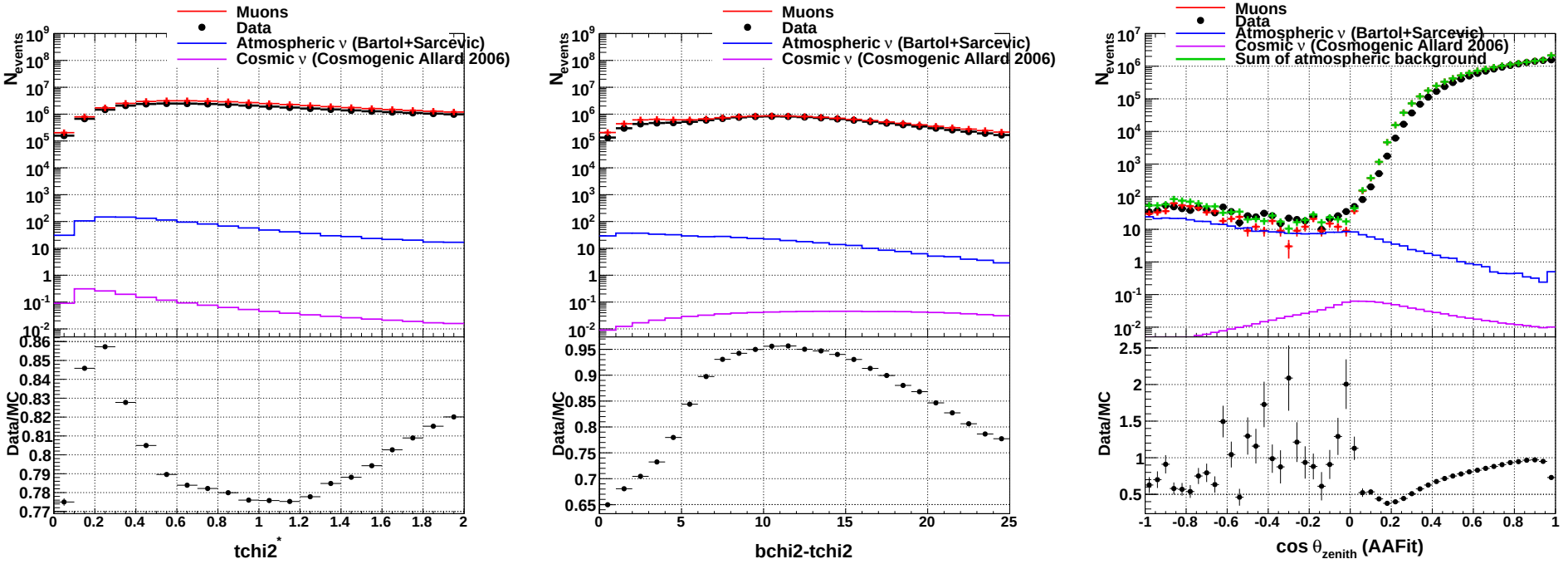

Figure 6.10: **Left:** tchi2*: the compatibility between data and Monte Carlo is kept, with the two distributions having the same slope. **Center**: bchi2-tchi2: the agreement between data and Monte Carlo is globally good, with compatible slopes. **Right**: angular selection: or this plot, it necessary to consider the sum of background components, in order to evaluate the neutrino contribution in the upgoing region. The agreement is still good, even if the plot is scattering in the upgoing region, due to the low statistic.

6.2.2.2 Comparisons after preliminary cut

At this stage the events made up by L1 hits in time coincidence only and having a track reconstructed by both reconstruction strategies, AAFit and BBFit. For each one of the six variables listed in Par. 5.4.1, a comparison between the possible background sources and the data is reported. It should be noted that at this stage there is no cut on the fit quality or the time structure, so some non-physical events present in data and not simulated by Monte Carlo can spoil the agreement.

- Number of hits (Fig. 6.11, left): data reproduce quite well the slope of Monte Carlo, leading to an acceptable agreement at this stage;
- Number of PMTs with more than one hit (Fig. 6.11, center): a certain consistency can be seen between data and Monte Carlo in the low range, while in the high range the agreement is spoiled by ill-reconstructed and non physical events, later eliminated by the quality cuts;
- Number of T2 floors (Fig. 6.11, right): globally the agreement is good, showing a consistency between data and Monte Carlo;
- Inertia tensor (Fig. 6.12, left): data and Monte Carlo have a similar slope in the low region, while for higher values ill-reconstructed events from data spoil the agreement. The cuts on track quality are able to heal this effect, as shown in the following steps;
- Hit time dispersion (Fig. 6.12, center): the agreement between data and Monte Carlo is globally good, but in the queue the surviving bioluminescence spoils the agreement;
- Mean dead time (Fig. 6.12, right): data and Monte Carlo have quite the same slopes, showing an acceptable compatibility between the two histograms.

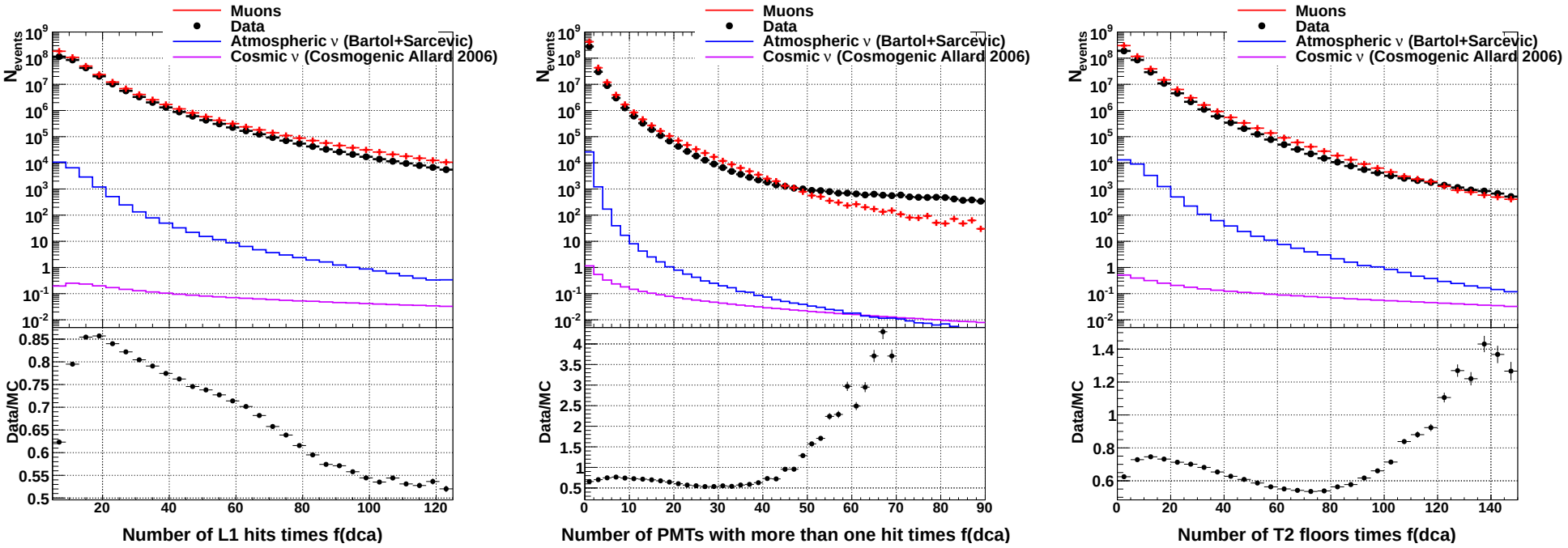

Figure 6.11: **Left:** Number of hits: data reproduce quite well the slope of Monte Carlo, inside statistical fluctuations. **Center**: Number of PMTs with more than one hit: a certain consistency can be seen between data and Monte Carlo in the low range, while in the high range the agreement is spoiled by ill-reconstructed and non physical events, later eliminated by the quality cuts. **Right**: Number of T2 floors: globally the agreement is good, showing a consistency between data and Monte Carlo.

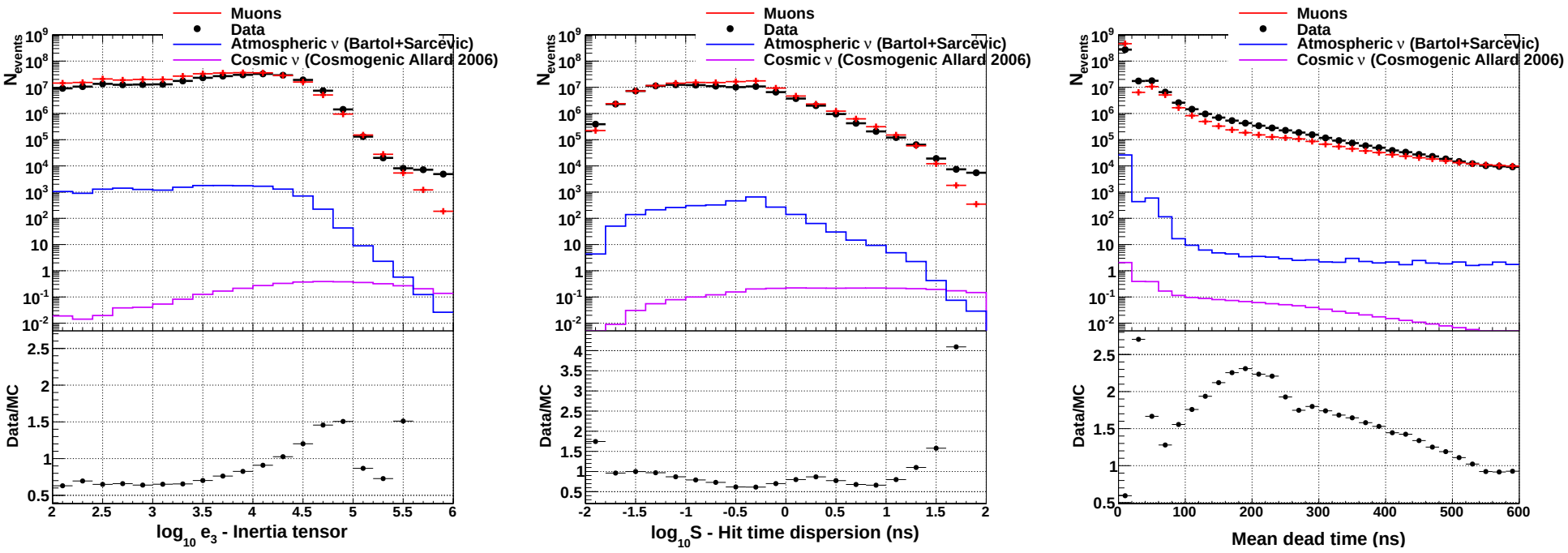

Figure 6.12: **Left:** Inertia tensor: data and Monte Carlo have a similar slope in the low region, while for higher values ill-reconstructed events from data spoil the agreement. The cuts on track quality are able to heal this effect, as shown in the following steps. **Center**: Hit time dispersion: the agreement between data and Monte Carlo is globally good, but in the queue the surviving bioluminescence spoils the agreement. **Right**: mean dead time: data and Monte Carlo have quite the same slopes, showing an acceptable compatibility between the two histograms.

6.2.2.3 Before application of the angular selection

Before show the comparisons of data and Monte Carlo at the final stage, when the statistics is very reduced because of the angular selection, it is interesting to verify that the agreement is maintained when the statistics is more significative. The following plots show the comparisons after the cut on BBFit reconstruction strategy, with the cuts chosen for the cosmogenic analysis chain. The same plots of the analysis under the hypothesis of a Waxman-Bahcall flux are shown in Appendix B.

- Number of hits (Fig. 6.13, left): data and Monte Carlo have quite the same slope, showing a good compatibility;
- Number of PMTs with more than one hit (Fig. 6.13, center): there is a good compatibility between data and Monte Carlo, which results in similar slope. The disagreement present at the preliminary stage is removed by quality cuts;
- Number of T2 floors (Fig. 6.13, right): the agreement is good, with an acceptable compatibility within the error bars;
- Inertia tensor (Fig. 6.14, left): the ratio between data and Monte Carlo is close to one, making the agreement acceptable;
- Hit time dispersion (Fig. 6.14, center): the agreement is acceptable, with data and Monte Carlo compatible inside the errors bars;
- Mean dead time (Fig. 6.14, right): globally the agreement is quite good, with a overestimation of data in the low range, compensated in the medium one, effect which could be due to a limited description by the simulations.

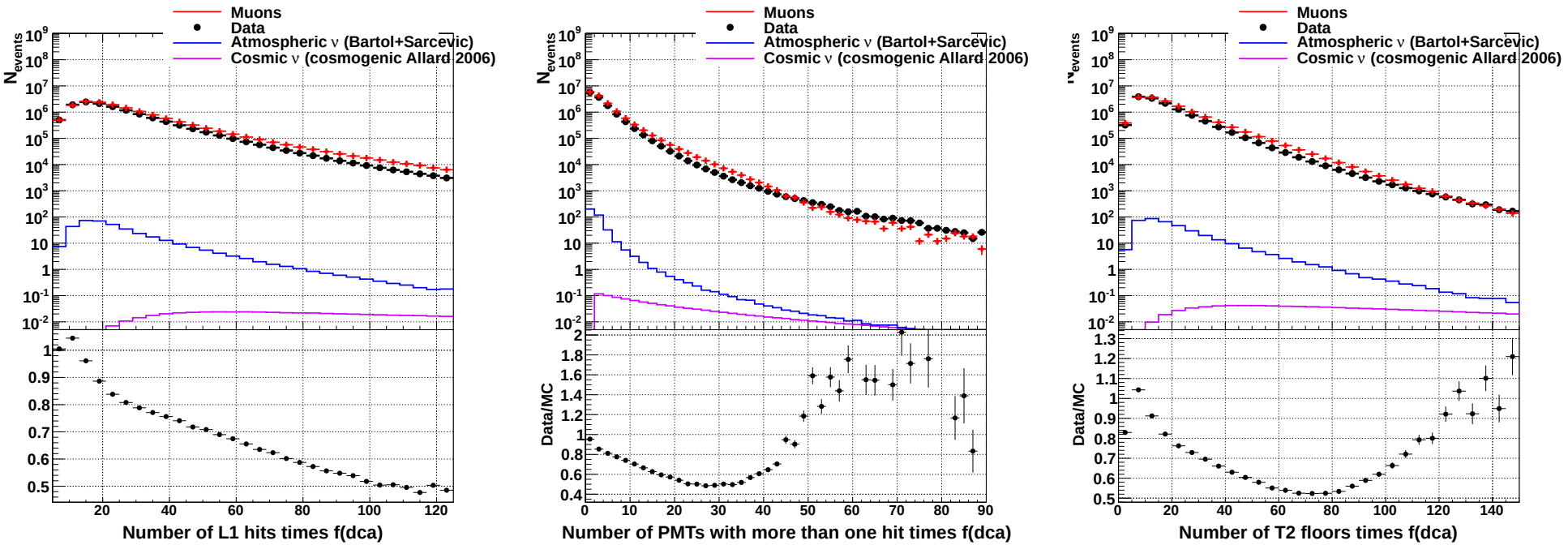

Figure 6.13: **Left:** Number of hits: data and Monte Carlo have quite the same slope, showing a good compatibility. **Center**: Number of PMTs with more than one hit: there is a good compatibility between data and Monte Carlo, which result in similar slope. The disagreement present at the preliminary stage is removed by quality cuts. **Right**: Number of T2 floors: the agreement is good, with an acceptable compatibility within the error bars.

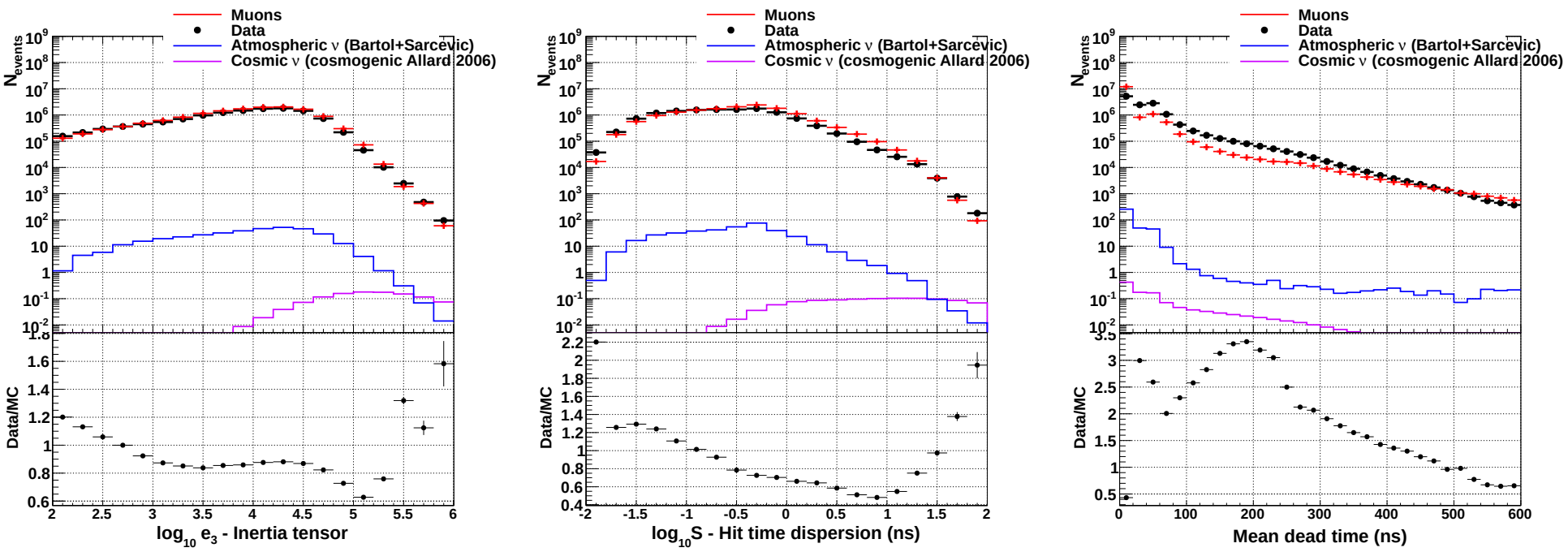

Figure 6.14: **Left:** Inertia tensor: the ratio between data and Monte Carlo is close to one, making the agreement acceptable. **Center**: Hit time dispersion: the agreement is acceptable, with data and Monte Carlo compatible inside the errors bars. **Right**: mean dead time: globally the agreement is quite good, with a overestimation of data in the low range, compensated in the medium one, effect which could be due to a limited description by the simulations.

6.2.2.4 After the angular selection

As can be seen in Tab. 6.2, at this final stage the statistic is reduced with respect to the previous steps. In order to have a better estimation of the agreement between data and simulations and taking into account also the contribution of atmospheric neutrinos, the sum of the background components is reported.

- Number of hits (Fig. 6.15, left): data reproduce quite well the slope of the sum of backgrounds. The disagreement toward the highest value is likely due, other than statistical fluctuation, to a lack of muons simulation for this particular phase space;
- Number of PMTs with more than one hit (Fig. 6.15, center): a certain consistency can be seen between data and the sum of background components, which are in a very good agreement;
- Number of T2 floors (Fig. 6.15, right): as for the number of hits, the slope of data is compatible Monte Carlo simulations;
- Inertia tensor (Fig. 6.16, left): data and Monte Carlo have a similar slope, resulting in an acceptable agreement;
- Hit time dispersion (Fig. 6.16, center): the agreement between data and Monte Carlo is globally good, their slopes are compatible inside error bars and considering statistical fluctuations;
- Mean dead time (Fig. 6.16, right): data and Monte Carlo have quite the same slopes, showing an acceptable compatibility between the two histograms.

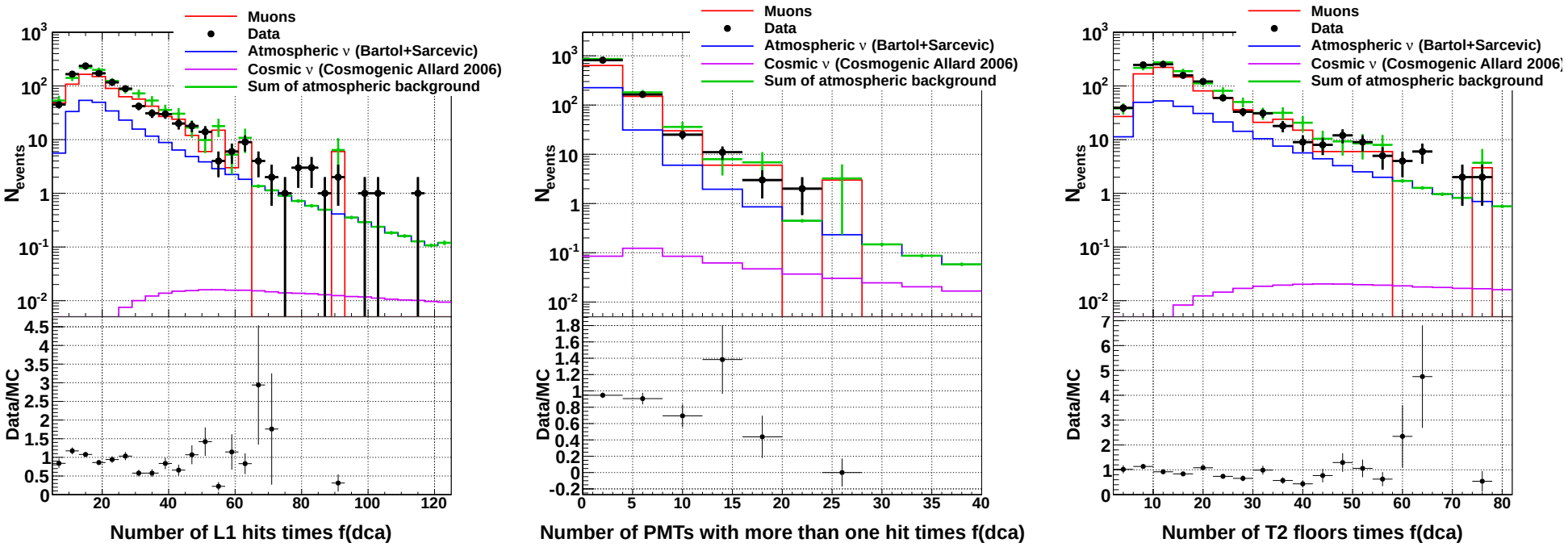

Figure 6.15: **Left:** Number of hits: data reproduce quite well the slope of the sum of backgrounds. The disagreement toward the highest value is likely due, other than statistical fluctuation, to a lack of muons simulation for this particular phase space. **Center**: Number of PMTs with more than one hit: a certain consistency can be seen between data and the sum of background components, which are in a very good agreement. **Right**: Number of T2 floors: as for the number of hits, the slope of data is compatible Monte Carlo simulations.

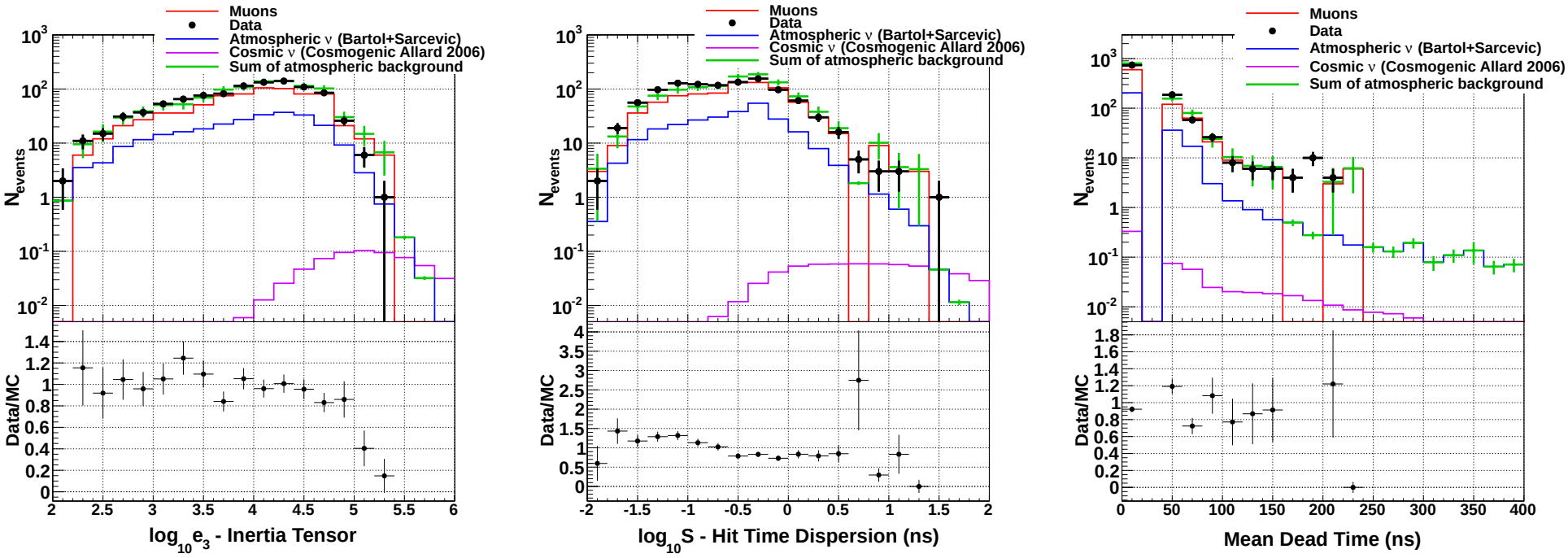

Figure 6.16: **Left:** Inertia tensor: data and Monte Carlo have a similar slope, resulting in an acceptable agreement. **Center**: Hit time dispersion: the agreement between data and Monte Carlo is globally good, their slopes are compatible inside error bars and considering statistical fluctuations. **Right**: Mean dead time: data and Monte Carlo have quite the same slopes, showing an acceptable compatibility between the two histograms.

6.2.3 Application of the multivariate analysis and upper limit

The last step of the analysis is the application of the chain developed in the previous chapter, in order to look for signal events in data. As explained, a different boost decision trees training has been applied for Waxman-Bahcall and cosmogenic flux.

The case of Waxman-Bahcall diffuse flux is shown in Fig. 6.17. This is fully compatible with the background slope and no data event survives the cut set by model rejection factor.

The comparisons of data and Monte Carlo in the case of cosmogenic flux is presented in Fig. 6.18. As it could be seen, the agreement is good between data and the sum of background components, with no event surviving the cut chosen by model rejection factor.

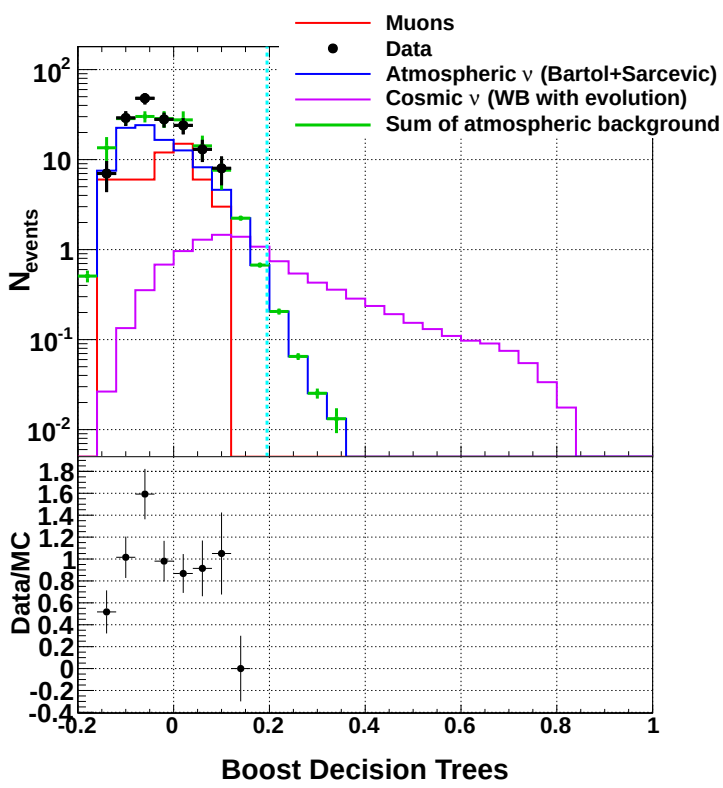

Figure 6.17: Agreement between data and Monte Carlo for the boost decision trees in the case of signal weighted with Waxman-Bahcall flux. Black dots are data, in red muons, in blue atmospheric neutrinos, in violet cosmic signal and in green the sum of the background components. The ratio between data and Monte Carlo is very close to 1, so the agreement could be considered satisfactory. No data survives the cut set by model rejection factor.

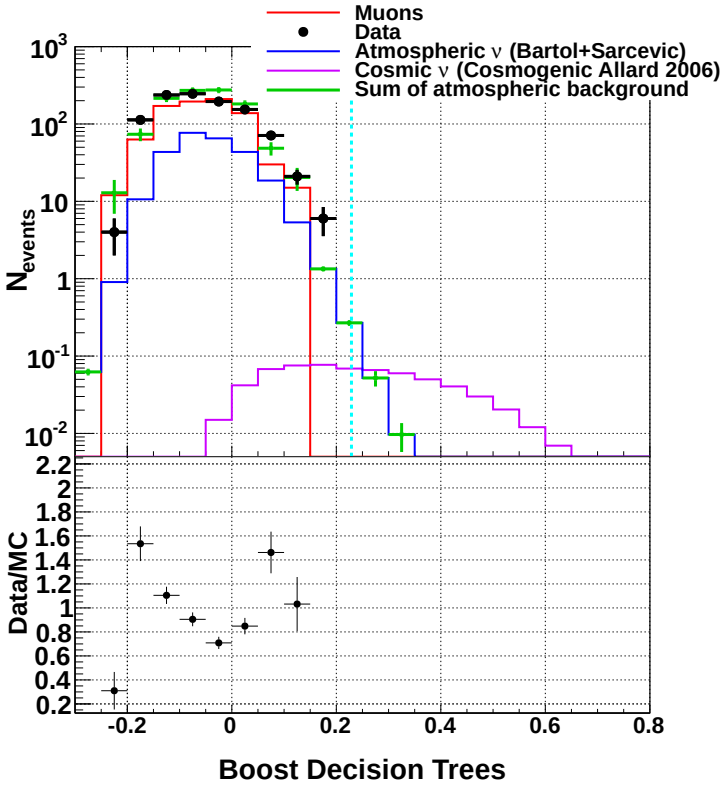

Figure 6.18: Agreement between data and Monte Carlo for the boost decision trees in the case of signal weighted with cosmogenic flux. Black dots are data, in red muons, in blue atmospheric neutrinos, in violet cosmic signal and in green the sum of the background components. The agreement between data and Monte Carlo is very good, compatible with the sum of the background components. No data survives the cut set by model rejection factor.

With these zero events surviving, it is possible to compute the upper limit to the fluxes. Using the Feldman-Cousins method [91], the upper limit resulting for Waxman-Bahcall is:

$$E^2\Phi < 2.2 \times 10^{-8} \text{ GeV m}^{-2}\text{s}^{-1}\text{sr}^{-1} \tag{6.1}$$

For the cosmogenic flux, the corresponding MRF to multiply the flux is 6.47. The upper limits for the analysis are shown in Fig. 6.19 in the case of Waxman-Bahcall and cosmogenic flux, computed with the Feldman-Cousins method. The sensitivity, defined as the average upper limit that would be obtained by an ensemble of experiments with the expected background and no true signal, is based on several realizations of the experiment, whereas the upper limit assessed here is computed for a unique realization: our data. The Poisson probability to get 0 events when 0.6 are expected, as in the case of Waxman-Bahcall flux, is 0.55. This is the probability of obtaining data given the hypothesis. In situations near a physical limit, it is possible to obtain a smaller upper limit estimate simply by random fluctuation: as in the present case, observing fewer events than were expected from background alone. This approach however suffers from some practical drawbacks: being it a fully frequentist construction, it does not handle background expectations or signal efficiencies which are known only with some limited accuracy.

An alternative to Feldman-Cousins, always following the frequentist approach, has been developed by Rolke [92]. It is based on the combination of a two dimensional confidence region and the large sample approximation to the likelihood ratio test statistic, which is more robust in presence of background uncertainty. The construction of the confidence region is the same as the one used in the Feldman-Cousins method, but the probabilities of the observations are exploited as ordering quantities to sort the observations to reach the desired confidence level. The main advantage of this method is being able to treat the background uncertainty as a statistical error [92]. For the present analysis, in the case of Waxman-Bahcall flux, the upper limit according to this method is set to:

$$E^2\Phi < 2.0 \times 10^{-8} \text{ GeV m}^{-2}\text{s}^{-1}\text{sr}^{-1} \tag{6.2}$$

The upper limit for cosmogenic analysis is equal to the flux multiplied by a factor 4.77.

It is interesting to compute also the upper limit (or rather the credibility level) using the Bayesian approach. In absence of a clear discovery, using the likelihood function for a Poisson distributed events, the upper limit can be derived from the posterior density. In this case of zero event found it is

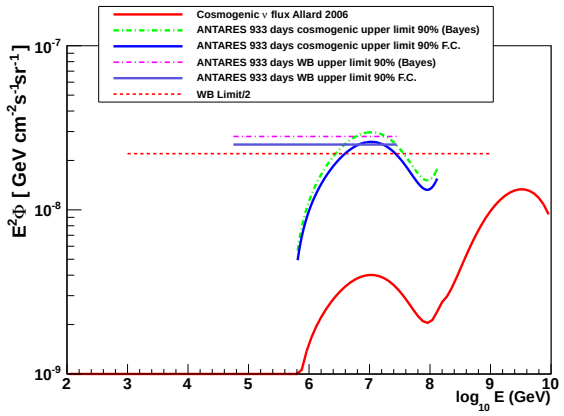

Figure 6.19: ANTARES upper limit for this analysis, in the case of Waxman-Bahcall and cosmogenic flux for 933 days of data taking. The reference fluxes are shown. The solid lines stand for the upper limits computed with the Feldman-Cousins method, the dot-dashed ones for the bayesian upper limits. All the upper limits are shown as $\nu_\mu + \overline{\nu}_\mu$.

rather simple to compute and for the Waxman-Bahcall it reports an upper limit of:

$$E^2\Phi < 2.8 \times 10^{-8} \text{ GeV m}^{-2}\text{s}^{-1}\text{sr}^{-1} \tag{6.3}$$

For the cosmogenic analysis, the corresponding MRF to multiply the flux to obtain the upper limit is equal to 7.66. However, like in any Bayesian analysis, this result is dependent from the different prior probabilities.

Conclusions

ANTARES telescope has been completed with 12 lines in May 2008, but the data taking has started since the 5-lines period in 2007. Since then, data taking is going on without interruptions. The main goal of ANTARES is now to search for cosmic neutrinos in the amount of data taken.

Diffuse fluxes originate from the sum of different possible astrophysical sources, able to produce high-energy neutrinos. The main contribution is given by AGN, GRB and the interaction of protons from cosmic rays with the cosmic microwave background and interstellar gas. Neutrinos are a good proof the existence of hadronic processes in cosmic accelerator like AGN or GRB (like the fireball model developed by Waxman and Bahcall). In this latter case, neutrinos are produced during the interaction of accelerating protons with the photons produced from electron bremsstrahlung radiation, and the flux depends also on the optical thickness of the source. Another hypothesis of neutrino diffuse flux is the production during the interaction of cosmic rays protons with different photon backgrounds (optical, infrared and microwave). This flux originates from pion decay and it is called cosmogenic, having also a higher energy range with respect to the Waxman-Bahcall one. The work presented in this thesis is finalized to the search for diffuse flux of astrophysical muon neutrinos, in the range of the ultra high energies (from 100 GeV to 100 EeV). The flux models exploited are the classic Waxman-Bahcall flux [32, 33] and a cosmogenic one [35], under the hypothesis of protons as primary cosmic rays.

The first step of this analysis is a study based on Monte Carlo simulations, in order to develop a robust algorithm able to keep the very feeble signal and reject the two sources of atmospheric background, coming from neutrinos and muons produced in cosmic rays interaction with the atmosphere. For this aim, a list of preliminary selection criteria has been chosen (see Par. 5.3), consisting essentially in the event time structure and track quality from the two reconstruction strategies used in ANTARES. Also, knowing that for energy above 10 PeV the Earth is opaque to neutrinos, the choice of an angular selection near the horizon is mandatory, to select a region where the

signal is more significative.

The best way to analyze this kind of signal is to perform a multivariate analysis, with the aid of the ROOT tool TMVA [89], exploiting a set of six variables (listed in Par. 5.4.1) each one representative of one aspect of the event, such as the event topology, its luminosity, its spatial and time extension. These variables are then combined via TMVA in a single estimator: the best one has happened to be the boost decision trees. After the application of this technique to the three different simulations (cosmic neutrinos, atmospheric neutrinos and atmospheric muons) the best cut to optimize the sensitivity to a given signal is chosen with the model rejection factor technique [90].

In order to choose the best set of cuts for the flux of interest, a scan on a large number of cut's combinations has been performed. For each cut, a set of three or more possible values has been defined and for each possible combination the boost decision trees technique has been trained, and the best achievable has been assessed. The combination reporting the best sensitivity has finally been chosen for the analysis.

The analysis for Waxman-Bahcall flux is described in Par. 5.5.1, with the number of expected events for one year of data scaling and over all the simulation livetime (933 days). The similar analysis for the cosmogenic flux is reported in Par. 5.5.2. The sensitivity for ANTARES is then estimated and presented in Fig. 5.19, resulting in a sensitivity for Waxman-Bahcall flux evaluated as $E^2\Phi = 3.6 \times 10^{-8}$ GeV $\mathrm{m}^{-2}\mathrm{s}^{-1}\mathrm{sr}^{-1}$ in the energy range from 58 TeV to 28 PeV. For the cosmogenic flux, the analysis on 933 days has reported a model rejection factor of 8.6, in the energy range form 562 TeV to 139 PeV.

The last chapter deals with the application of the analysis algorithm, both for Waxman-Bahcall and cosmogenic flux, to ANTARES data. Before that, the identification and treatment of the so-called sparking runs, able to feign astrophysical signal, is presented in Par. 6.1, with the list of runs identified as sparking reported in Appendix A. The preliminary cuts and analysis algorithm have been applied on the full data sample, in order to search the presence of a signal. In the end, the boost decision trees has been applied to the sample, finding no event passing the analysis cuts. For the Waxman-Bahcall flux, an upper limit of $E^2\Phi < 2.2 \times 10^{-8}$ GeV $\mathrm{m}^{-2}\mathrm{s}^{-1}\mathrm{sr}^{-1}$ is obtained. The upper limits are summarized in Fig. 6.19.

Appendix A

List of sparking runs

In this the list of sparking runs identified by the algorithm described in Par. 6.1 is presented. For each run also the corresponding position is shown. These runs has been retired from the analysis final sample.

RUN	**OM index**	**Line**
31309	41	L1 F14 OM2
33608	500	L7 F17 OM2
33610	500	L7 F17 OM2
36600	32	L1 F11 OM2
36666	839	L12 F5 OM2
36670	838	L12 F5 OM1
36689	839	L12 F5 OM2
38347	767	L11 F6 OM2
38348	767	L11 F6 OM2
38351	767	L11 F6 OM2
38352	767	L11 F6 OM2
38353	767	L11 F6 OM2
38355	767	L11 F6 OM2
38357	767	L11 F6 OM2
38342	354	L5 F19 OM0
41668	618	L9 F7 OM0
42507	812	L11 F21 OM2
42509	812	L11 F21 OM2
42511	812	L11 F21 OM2
42513	812	L11 F21 OM2
42746	812	L11 F21 OM2
42915	812	L11 F21 OM2

42919	812	L11 F21 OM2
43196	812	L11 F21 OM2
43202	812	L11 F21 OM2
43206	812	L11 F21 OM2
43210	812	L11 F21 OM2
43996	152	L3 F20 OM2
44030	152	L3 F20 OM2
44035	152	L3 F20 OM2
44070	152	L3 F20 OM2
54512	584	L8 F20 OM2

Appendix B

Data/MC comparisons for Waxman-Bahcall analysis

In this appendix the plots of data and Monte Carlo comparison for the Waxman-Bahcall analysis chain are shown, at same steps chosen for the cosmogenic analysis.

B.1 Comparisons of the cut variables

Before going on comparing the variable exploited in the multivariate analysis, it is interesting to look at the agreement for the quality parameters used to clean the sample from pathological events (listed in 5.3). These variables are presented each one before the cut of interest.

- Λ (AAFit quality parameter) (Fig. B.1, left): data and Monte Carlo are in a good agreement, reproducing quite the same slope;
- β (AAFit quality parameter) (Fig. B.1, center): globally the agreement between data and simulation is good;
- Reconstruction agreement (Fig. B.1, right): data and Monte Carlo are compatible, showing an acceptable agreement on the whole range;
- tchi2* (BBFit quality parameter) (Fig. B.2, left): the compatibility between data and Monte Carlo is kept, with the two distributions having the same slope;
- bchi2-tchi2 (BBFit quality parameter) (Fig. B.2, center): the agreement between data and Monte Carlo is globally good, with compatible slopes;

- Zenith angle (according to AAFit reconstruction) (Fig. B.2, right): for this plot, it necessary to consider the sum of background components, in order to evaluate the neutrino contribution in the upgoing region. The agreement is still good, even if the plot is scattering in the upgoing region, due to the low statistic.

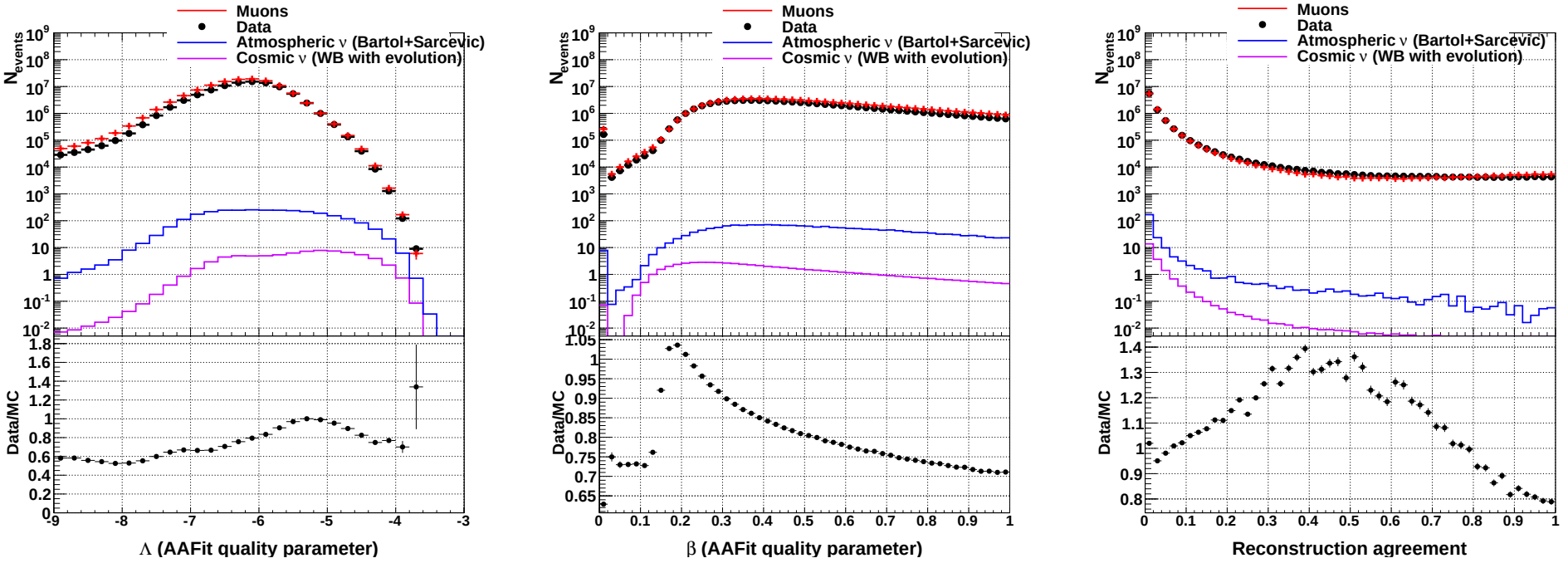

Figure B.1: **Left:** Λ: data and Monte Carlo are in a good agreement, reproducing quite the same slope. **Center**: β: globally the agreement between data and simulation is good. **Right**: reconstruction agreement data and Monte Carlo are compatible, showing an acceptable agreement on the whole range.

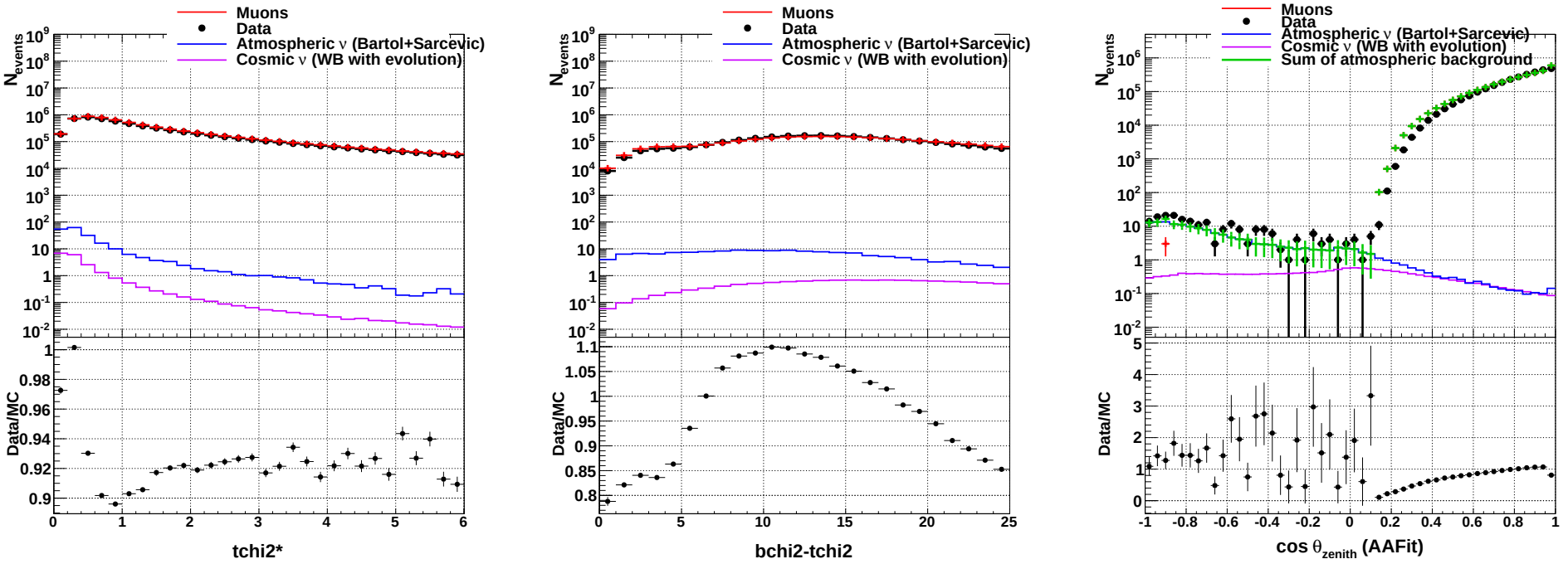

Figure B.2: **Left:** tchi2*: the compatibility between data and Monte Carlo is kept, with the two distributions having the same slope. **Center**: bchi2-tchi2: the agreement between data and Monte Carlo is globally good, with compatible slopes. **Right**: angular selection for this plot, it necessary to consider the sum of background components, in order to evaluate the neutrino contribution in the upgoing region. The agreement is still good, even if the plot is scattering in the upgoing region, due to the low statistic.

B.2 Comparison after the cut on reconstruction consistency

- Number of hits (Fig. B.3, left): there is a consistency between data and Monte Carlo, which show the same slope and have a ratio quite close to one;
- Number of PMTs with more than one hit (Fig. B.3, center): the slopes are inside statistical fluctuations and the agreement is good, especially in the lower range. The data fluctuation in the queue are most probably due to some bright-point-like events, later rejected by the cut on BBFit quality variables;
- Number of T2 floors (Fig. B.3, right): the ratio between data and Monte Carlo is very close to one, so the agreement is considered satisfactory;
- Inertia tensor (Fig. B.4, left): the agreement is very good, inside statistical fluctuations and with a ratio close to one;
- Hit time dispersion (Fig. B.4, center): the ratio is always quite close to one, showing a good compatibility between data and Monte Carlo;
- Mean dead time (Fig. B.4, right): even if the slope of Monte Carlo and data is quite the compatible, the disagreement in the low value region is most likely due to the simulation's limited description of detector effects.

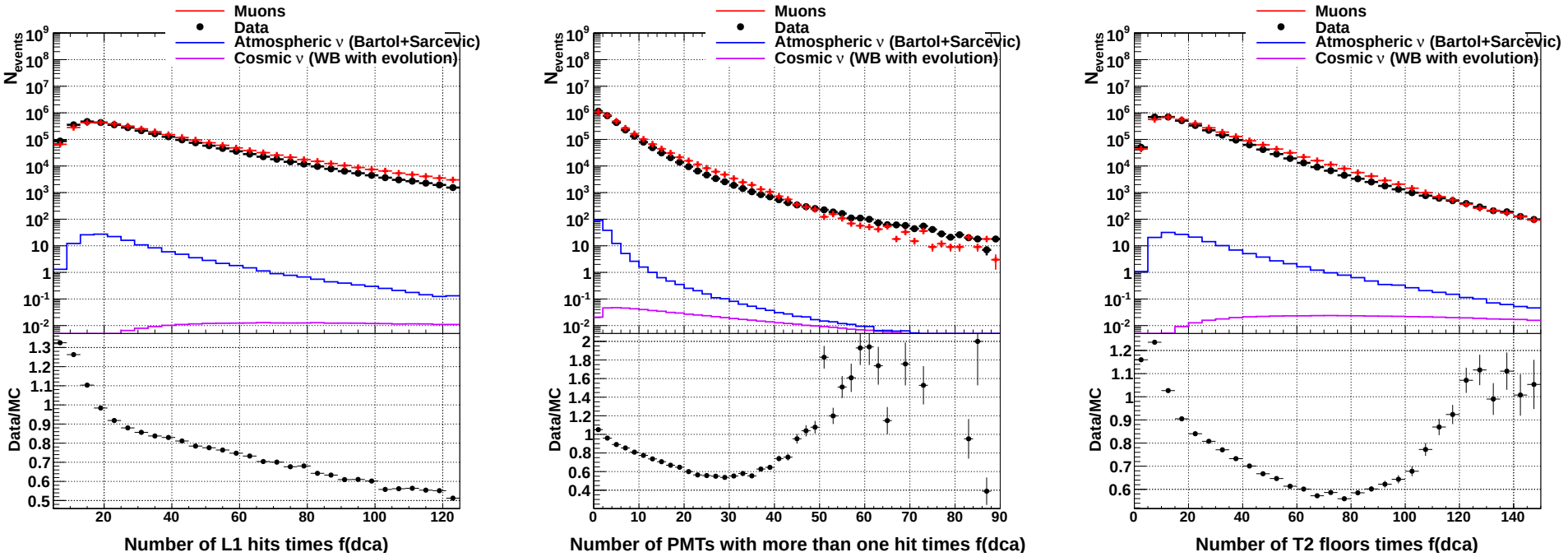

Figure B.3: **Left:** Number of hits: there is a consistency between data and Monte Carlo, which show the same slope and have a ratio quite close to one. **Center**: Number of PMTs with more than one hit: the slopes are inside statistical fluctuations and the agreement is good, especially in the lower range. The data fluctuation in the queue are most probably due to some bright-point-like events, later rejected by the cut on BBFit quality variables. **Right**: Number of T2 floors: the ratio between data and Monte Carlo is very close to one, so the agreement is considered satisfactory.

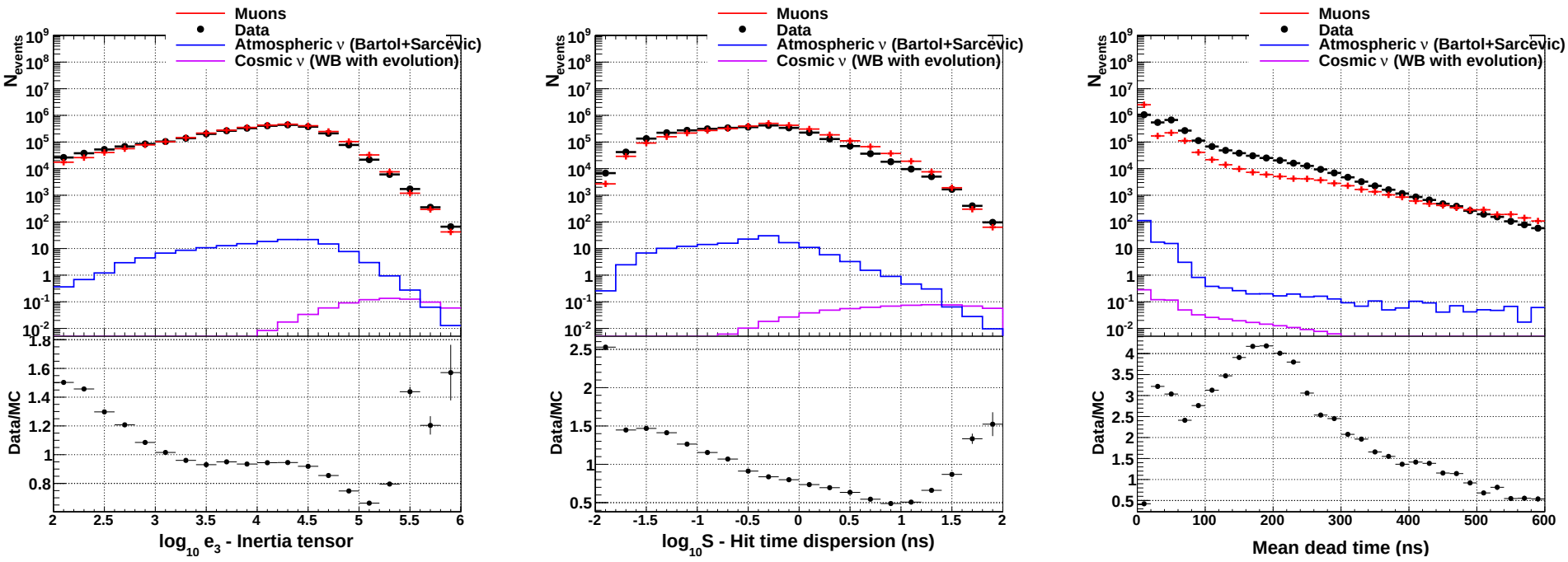

Figure B.4: **Left:** Inertia tensor: considering statistical fluctuations, data and Monte Carlo have a similar slope, resulting in an acceptable agreement. **Center**: Hit time dispersion: the ratio is always quite close to one, showing a good compatibility between data and Monte Carlo. **Right**: mean dead time: even if the slope of Monte Carlo and data is quite the compatible, the disagreement in the low value region is most likely due to the simulation's limited description of detector effects.

B.3 Comparison after the angular selection

As can be seen in Tab. 6.1, at this final stage the statistic is very reduced, as for the cosmogenic analysis. In order to have a better estimation of the agreement between data and simulations, the sum of the background components is reported.

- Number of hits (Fig. B.5, left): even if the statistical fluctuations due to low statistic make the plot scattering, there is a global consistency between the data and the sum of background components;
- Number of PMTs with more than one hit (Fig. B.5, center): a certain consistency can be seen between data and the sum of background components, which are in a very good agreement especially in the low region;
- Number of T2 floors (Fig. B.5, right): as for the number of hits, even if the plot is scattering, the slope of data is quite well reproduced by Monte Carlo simulations;
- Inertia tensor (Fig. B.6, left): considering statistical fluctuations, data and Monte Carlo have a similar slope, resulting in an acceptable agreement;
- Hit time dispersion (Fig. B.6, center): the slope of data and sum of background component is well reproduced, giving a globally good agreement between data and Monte Carlo;
- Mean dead time (Fig. B.6, right): data and Monte Carlo have quite the same slopes, showing an acceptable compatibility between the two histograms.

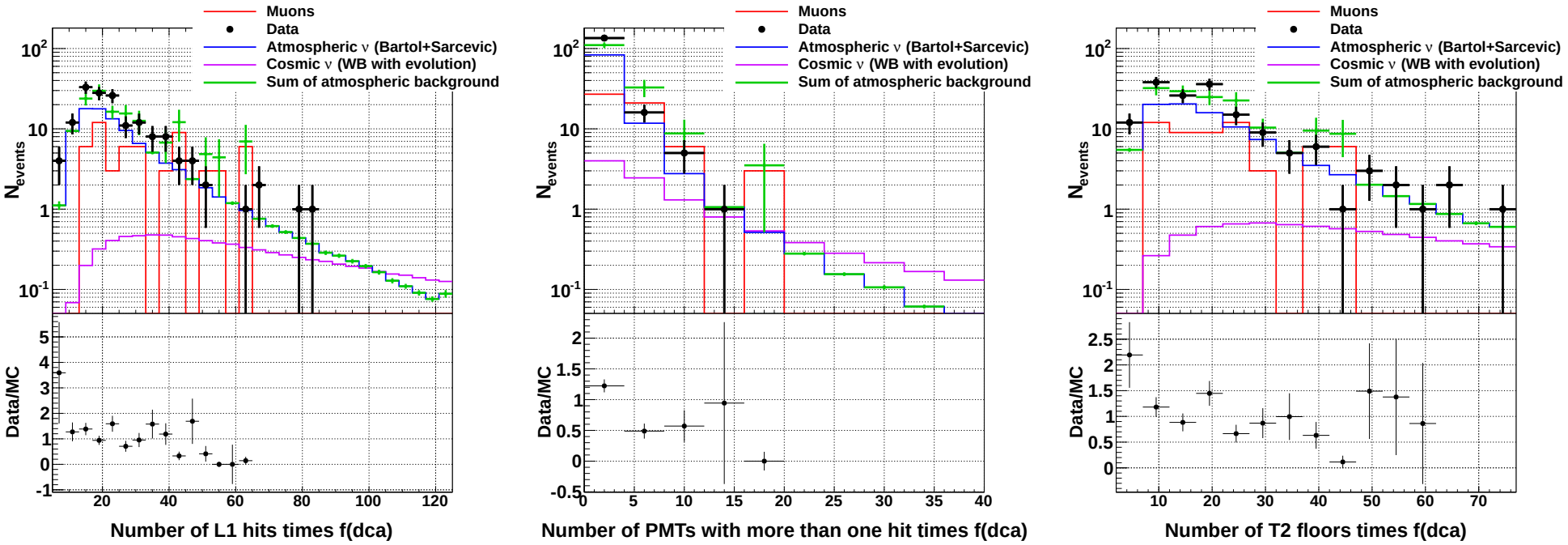

Figure B.5: **Left:** Number of hits: even if the statistical fluctuations due to low statistic make the plot scattering, there is a global consistency between the data and the sum of background components. **Center**: Number of PMTs with more than one hit: a certain consistency can be seen between data and the sum of background components, which are in a very good agreement especially in the low region. **Right**: Number of T2 floors: as for the number of hits, even if the plot is scattering, the slope of data is quite well reproduced by Monte Carlo simulations.

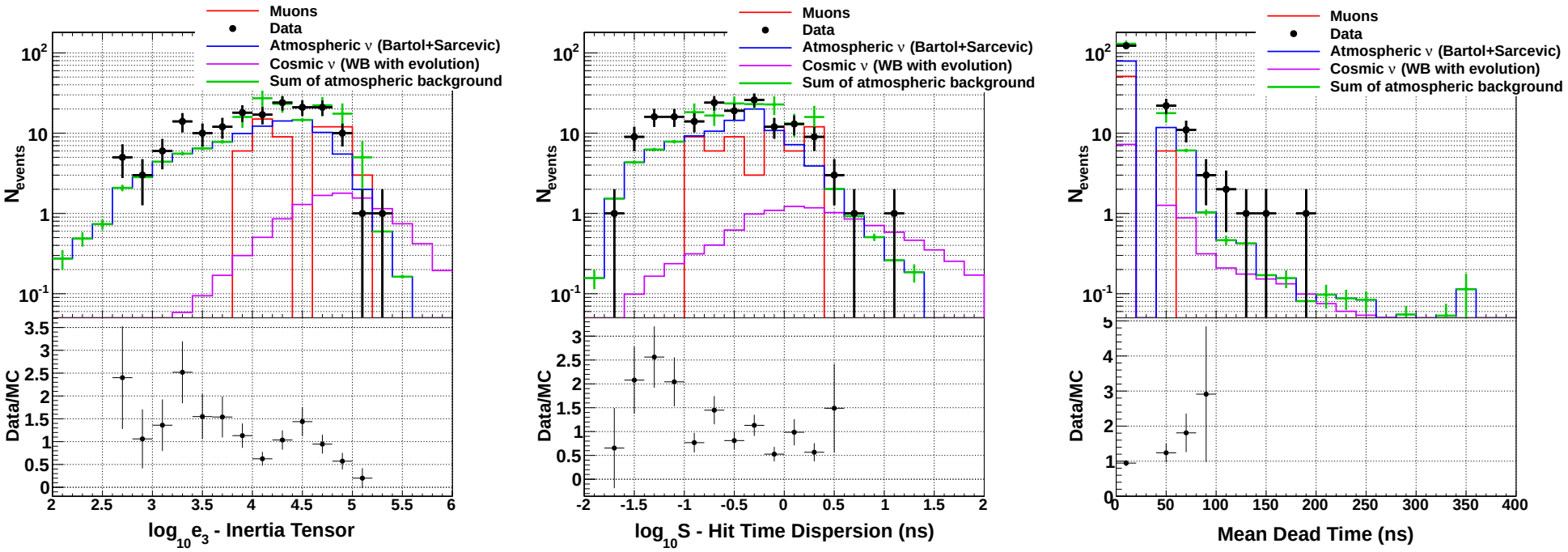

Figure B.6: **Left:** Inertia tensor: considering statistical fluctuations, data and Monte Carlo have a similar slope, resulting in an acceptable agreement. **Center**: Hit time dispersion: the slope of data and sum of background component is well reproduced, giving a globally good agreement between data and Monte Carlo. **Right**: mean dead time: data and Monte Carlo have quite the same slopes, showing an acceptable compatibility between the two histograms.

Bibliography

[1] V. F. Hess. *Phys. Zeit.*, **13**:1084 (1912).

[2] Particle Data Group, C. Amsler et al., *Physics Letters B* **667** (2010) 1.

[3] E. Fermi, **On the origin of cosmic rays**, *Phys. Rev.*, **75**:1169 (1949).

[4] E. Fermi, **Galatic magnetic fields and the origin of cosmic radiation**, *Astroph. J.*, **119**:1 (1954).

[5] V. L. Ginzburg, Y.M. Khazan, V.S. Ptuskin, **Origin of Cosmic Rays: Galactic Model with Halo**, *Astrophysics and Space Science*, **68**, 295-314 (1980).

[6] J. Abraham et al. **Correlation of the highest-energy cosmic rays with nearby extragalactic objects**, *Science*, **318**:938-943 (2007).

[7] J. R. Horandel, **Models of the knee in the energy spectrum of cosmic rays**, *Astrop. Phys.*, **21**:241-265 (2004).

[8] T. Antoni et al., **Electron, muon and hadron lateral distributions measured in air-showers by the KASCADE experiment**, *Astrop. Phys.*, **14**:245-206 (2001).

[9] A. M. Hills, *Ann. Rev. Astron. Astrophys.*, **22**:425 (1984).

[10] G. T. Zaptsepin and V. A. Kuz'min, *JETP Lett.*, **4**:78 (1966).

[11] The HIRES Collaboration, *Phys. Rev. Lett.*, **100**:101101 (2008).

[12] J. Abraham for the Auger Coll., *Phys. Rev. Lett.*, **101**:06110 (2008).

[13] M. Takeda et al., *Phys. Rev. Lett.*, **81**:1163 (1998).

[14] T. Chiarusi and M. Spurio, **High-Energy Astrophysics with Neutrino Telescopes**, *Eur. Phys. J. C*, **65**:649-701 (2010).

[15] F. Aharonian et al., **High energy astrophysics with ground-based gamma ray detectors**, *Rep. Prog. Phys.*, **31**:096901 (2008).

[16] F. Halzen and D. Hooper, **High-energy neutrino astronomy: the cosmic ray connectio**, *Rer. Prog. Phys.*, **65**:1025-1078 (2002).

[17] C. E. Fichtel and J. I. Trombka, **Gamma-ray astrophysics: new insight into the Universe**, RP 1386, NASA (1997).

[18] J. Vandenbroucke, for the Fermi LAT collaboration, **Physics and astrophysics with gamma-ray telescopes**, *Nucl. Phys. B*, **00**:1-7 (2010).

[19] T. C. Weekes et al., **Observation of TeV gamma rays from the Crab Nebula using the atmospheric Cherenkov imaging technique**, *Astroph. J.*, **342**:379-395 (1989).

[20] R. Mirzoyan et al., **The first telescope of the HEGRA air Cherenkov imaging telescope array**, *Nucl. Instr. and Meth.*, **351**:513:526 (1994).

[21] R. Enomoto et al., **Design study of CANGAROO-III, stereoscopic imaging atmospheric Cherenkov telescope for sub-TeV gamma-ray**, *Astrop. Phys.*, **16**:235-244 (2002).

[22] F. Piron (CAT coll.), **Observation of the gamma-ray emission above 250 GeV from the Blazars Markarian 501 and Markarian 421 by the CAT Cherenkov Atmospheric Image Telescope**, *Proceedings of the XIth recontres de Blois* (1999).

[23] J. A. Hinton, **The status of the HESS project**, *New Astron. Rev.*, **48**:331-337 (2004).

[24] T. C. Weekes et al., **VERITAS: the Very Energetic Radiation Imaging Telescope Array System**, *Astrop. Phys.*, **17**:221-243 (2002).

[25] J. Albert et al., **Physics and Astrophysics with a ground-based gamma-ray telescope of low energy threshold**, *Astrop. Phys.*, **23**:493-509 (2005).

[26] J. Abraham et al., **Correlation of the highest-energy cosmic rays with nearby extragalactic objects**, *Science*, **318**:938-942 (2008).

[27] E. Waxman and J. Bahcall, **High energy neutrinos from cosmological gamma-ray burst fireball**, *Phys. Rev. Lett.*, **78**:2292 (1997).

[28] D. Guetta and E. Amato, **Neutrino from individual gamma-ray bursts in the BATSE catalog**, *Astrop. Phys.*, **20**:429 (2004).

[29] P. Sreekumar et al. (EGRET Coll.), **EGRET Observation of the Extragalactic Gamma-Ray Emission**, *Astroph. J.*, **494**:523-534 (2000).

[30] R. M. Crocker and F. Aharonian, **The Fermi bubbles: Giant, multi- billion-year-old reservoirs of galactic center cosmic rays**, *arXiv:1008.2658v3* (2010).

[31] S. Adrian-Martinez et al., **Detection Potential of the KM3NeT Detector for High-Energy Neutrinos from the Fermi Bubbles** , *Astrop.Phys.*, **42**:7-14 (2013).

[32] E. Waxman and J. Bahcall, **High energy neutrinos from astrophysical sources: An upper bound**, *Phys. Rev. D*, **59**:023002 (1998).

[33] E. Waxman and J. Bahcall, **High energy neutrinos from astrophysical sources: The upper bound is robust**, *Phys. Rev. D*, **64**:023002 (2001).

[34] R. J. Protheroe, K. Mannheim and J. P. Rachen, *Phys. Rev. D*, **63**:023003 (2001).

[35] D. Allard et al., **Cosmogenic neutrinos from the propagation of ultra high energy nuclei**, JCAP09 005 (2006).

[36] S. Adrian-Martinez et al., **Search for relativistic magnetic monopoles with the ANTARES neutrino telescope**, *Astrop. Phys.*, **35**:634-640 (2012).

[37] J.A. Aguilar et al., **Search for a diffuse flux of high-energy ν_μ with the ANTARES neutrino telescope**, *Phys. Lett. B*, **696**:19-22 (2011).

[38] J. Pumplin et al., **New generation of parton distributions with uncertainties from global QCD analysis**, *JHEP* **7**(12) (2001).

[39] S. L. Glashow, **Resonant scattering of antineutrinos**, *Phys. Rev.*, **118** 316 (1969).

[40] L. Landau and I. Pomeranchuk, **The Collected Papers of L. D. Landaus**, *Pergamon, New York* (1965).

[41] **The CERN Program library**, *http://www.info.cern.ch/asd/cernlib/*.

[42] H. Plothow-Besch, *Comp. Phys. Comm.*, **82**:74-90 (1994).

[43] R. Gandhi et al., **Ultra High Energy Neutrino Interactions**, *Astrop. Phys.*, **5**:81 (1996).

[44] A. Connolly et al., **Calculation of High Energy Neutrino-Nucleon Cross Sections and Uncertainties Using the MSTW Parton Distribution Functions and Implications for Future Experiments**, *Phys. Rev. D* **83**:113009 (2011)

[45] G. Ingelman, A. Edin and J. *Comp. Phys. Comm.*, **101**:108-134 (1997).

[46] T. Sjostrand, *Comp. Phys. Comm.*, **82**:74-90 (1994).

[47] The CTEQ Collaboration, *Eur. Phys. J. C*, **15**:375-392 (2000).

[48] W. R. Leo, **Techniques for Nuclear and Particle Physics Experiments**, *Springer-Verlag* (1988).

[49] A. Heijeboer, **Track Reconstruction and Point Source Search with ANTARES**, PhD Thesis, NIKHEF, Amsterdam (2004).

[50] J. Brunner, **The refraction index at ANTARES site**, ANTARES internal note (2000).

[51] A. M. Markov, in *Proceeding of the Rochester Conference*, New York (1960).

[52] G. A. Askaryan et al., *Nucl. Instr. and Meth.*, **164**:267 (1979).

[53] P. Amram et al., **Background light in potential sites for the ANTARES undersea neutrino telescope**, *Astrop. Phys.*, **13**:127-136 (2000).

[54] M. Ageron et al., **Performance of the first ANTARES detector line**, *Astrop. Phys.*, **31**:227-283 (2009).

[55] A. Roberts, **Birth of high-energy neutrino astronomy: a personal history of the DUMAND project**, *Rev. Mod. Phys.*, **64**:259 (1992).

[56] L. Kuzmichev, **The Baikal neutrino experiment: from NT200 to NT200+**, in *Proceedings of the 29th ICRC* (2005).

[57] P. Amram et al. (ANTARES Coll.), **The ANTARES Optical Module**, *Nucl. Instr. and Meth. A*, **484**:369 (2002).

[58] J. A. Aguilar et al. (ANTARES Coll., **Transmission of light in deep sea water at the ANTARES site**, *Astrop. Phys.*, **19**:253-267 (2003).

[59] B.A.P. van Rens, *The software trigger in ANTARES*, ANTARES-SOFT-2004-001 (2004).

[60] M. Circella, **The construction of ANTARES, the first undersea neutrino telescope**, *Nucl. Instr. and Meth. A*, **602**:1-6 (2009).

[61] J. A. Aguilar et al. (ANTARES Coll.), **The Data Acquisition System for the ANTARES neutrino telescope**, *Nucl. Instr. and Meth. A*, **570**:107 (2007).

[62] L. Core., **Effective high thresholds measure**, ANTARES internal note, ANTARES-CALI-2012-001 (2012).

[63] J. A. Aguilar, **Analysis of the Optical Beacon system and search for point-like sources in the ANTARES neutrino telescope**, PhD Thesis at the Universitat de Valencia (2008).

[64] J. Brunner, **Simulation of ^{40}K signals**, ANTARES internal note, ANTARES-SOFT-1999-003 (1999).

[65] M. De Jong, **Coincidence rate of Potassium-40 seen by MILOM**, ANTARES internal note, ANTARES-PHYS-2006-001 (2006).

[66] D. J. L. Bailey, **GENHEN v5r1: Software Documentation**, ANTARES internal note, ANTARES-SOFT-2002-004 (2002).

[67] A. M. Cooper-Sarkar et al., *Int. J. Mod. Phys. A.*, **13**:3385-3586 (1998).

[68] M. Honda et al., *Phys. Rev. D*, **52**:4985-5005 (1995).

[69] G. D. Barr et al., *Phys. Rev. D*, **70**:023006 (2004).

[70] G. Battistoni, A. Ferrari, T. Montaruli and P. Sala, **The FLUKA atmospheric neutrino flux calculation**, *hep-ph/0207035* (2002).

[71] G. D. Barr, T. K. Gaisser, P. Lipari, S. Robbins and T. Stanev, *http://www-phoh.physics.ox.ac.uk/∼barr/fluxfiles.*

[72] C. G. S. Costa, **The prompt lepton cookbook**, *Astrop. Phys.*, **16**:193-204 (2001).

[73] D. Heck et al., FZKA 6019, Forshungszentrum Karlsruhe (1998).

[74] G. Carminati et al., **Atmospheric MUons from PArametric formulas: a fast GEnerator for neutrino telescopes**, *Comp. Phys. Comm.*, **179**:915-923 (2008).

[75] Y. Becherini et al., *Astrop. Phys.*, **25**:1 (2006).

[76] C. Kopper. **A software framework for KM3NeT**, *Nuclear Instruments and Methods in Physics Research Section A*, **602**(1):107 â 110, Proceedings of the 3rd International Workshop on a Very Large Volume Neutrino Telescope for the Mediterranean Sea (2009).

[77] Rene Rivera, **Boost C++ Libraries**, http://www.boost.org/ (2007).

[78] The Root team, **The ROOT analysis framework**, http://root.cern.ch/ (2010).

[79] **GEANT program manual**, *CERN program library long writeup*, **W5013** (1993).

[80] S. Navas and L. Thompson, **KM3 User Guide and Reference Manual**, ANTARES internal note, ANTARES-SOFT-1999-011 (1999).

[81] P. Antonioli et al., **A three-dimensional code for muon propagation through the rock: MUSIC**, *Astrop. Phys.*, **7**:357 (1997).

[82] M. De Jong, **The TriggerEfficiency program**, ANTARES internal note, ANTARES-SOFT-2009-001 (2009).

[83] J. Carr, S. Escoffier and D. Zaborov, **Proposition for an alternative trigger based on the T2 cluster trigger**, ANTARES internal note, ANTARES-SOFT-2007-016 (2007).

[84] A. J. Heiboer, **Track reconstruction and Point Source Searches with ANTARES**, PhD Thesis at the Amsterdam University (2004).

[85] J. Brunner, **The BBFit reconstruction algorithm**, ANTARES internal note, ANTARES-SOFT-2009-003 (2009).

[86] J. A. Aguilar et al., **A Fast Algorithm for Muon Track Reconstruction and its Application to the ANTARES Neutrino Telescope**, *Astropart.Phys.* vol. 34, pp. 652â662 (2011).

[87] C. Riviere, **Run-by-run Monte Carlo simulation for ANTARES: v2**, ANTARES internal note, ANTARES-PHYS-2012-001 (2012).

[88] E. Presani, **Neutrino Induced Showers From Gamma-Ray Burst**, PhD Thesis (2011).

[89] A. Hoecker et al., **TMVA 4, toolkit for multivariate analysis in ROOT**, CERN-OPEN-2007-007 (2009).

[90] G.C. Hills and K. Rawkins, **Unbiased cuts for optimal upper limits in neutrino detectors: the model of rejection technique**, *astro-ph/0209350* (2002).

[91] G.J. Feldman and R.D. Cousins, **Unified approach to the classical statistical analysis of small signals**, *Phys. Rew. D.* **57**(7):3873:3889 (1998).

[92] W. Rolke and A. Lopez, **Confidence intervals and upper bounds for small signals in the presence of background noise**, *Nucl. Instrum. Meth. A* **458**:745-758 (2001).